Improved Techniques in Ultrasonic Molecular Imaging for Evaluating Response to Cancer Therapy

Jason E. Streeter

A dissertation submitted to the faculty of the University of North Carolina at Chapel Hill in partial fulfillment of the requirements for the degree of Doctor of Philosophy in the Department of Biomedical Engineering.

Chapel Hill
2013

Approved by:

Paul A. Dayton, Ph.D.

Caterina M. Gallippi, Ph.D.

Richard L. Goldberg, Ph.D.

David S. Lalush, Ph.D.

Jen Jen Yeh, M.D.

Abstract

JASON E. STREETER: Improved Techniques in Ultrasonic Molecular Imaging for Evaluating Response to Cancer Therapy.
(Under the direction of Paul A. Dayton, Ph.D.)

Molecular imaging is a broad term for describing a technique designed to evaluate molecular activity in biological systems. Recently, ultrasound has gained interest in molecular imaging due to the practical advantages over traditional imaging modalities: it is inexpensive, safe and portable.

The principle behind ultrasonic molecular imaging (USMI) is the selective targeting of acoustically active intravascular microbubbles to biomarkers expressed on the endothelium. Once accumulated at the target site, the microbubbles enhance the acoustic backscatter from pathologic tissue that might otherwise be difficult to distinguish from normal tissues. Since USMI has the potential to provide information prior to the appearance of phenotypic changes, it is proposed that this method can facilitate early assessment of disease progression. Pre-clinical imaging studies have demonstrated the efficacy of USMI for applications including, but not limited to, assessment of tumor angiogenesis, evaluation of cardiovascular disease, and imaging dysfunctional endothelium, thrombus and inflammation.

Although significant advances in USMI have been made, there remain challenges that need to be addressed as this technique advances toward clinical relevance. The ultimate goal of USMI is to determine the degree to which biomarkers are expressed by the target tissue. Therefore, it is essential that targeted microbubbles adhere in quantities that produce backscattered intensities in greater magnitude than the signal

from non-specific targeting. Given this requirement, research has primarily focused on improving the sensitivity to bound microbubbles, improving the ability to quantify biomarker expression, increasing the quantity of targeted microbubbles retained at the site of pathology, and improving microbubble architecture to minimize the non-specific retention of microbubbles and immunogenic response.

This dissertation supports the following hypotheses for *in vivo* USMI experiments:

1. Producing size-selected microbubbles increases detection sensitivity.

2. Implementing a 3-D ultrasound platform improves our ability to quantify biomarker expression.

3. Using acoustic radiation force enhances microbubble targeting.

4. Creating buried-ligand microbubbles reduces immunogenic response and non-specific targeting.

These improvements will ultimately provide a basis of methods, which we will draw from to assess a tumor's response to therapy and compare it to more traditional methods.

This is dedicated to my family,

for their patience,

for their encouragement,

for their support,

and for their love.

Acknowledgments

First, I would like to thank Paul Dayton. Your dedication to my education and research throughout my graduate career is greatly appreciated. I also would like to acknowledge Dr. Mark Borden for teaching me how to fabricate and size-select microbubble contrast agents. This knowledge has been a fundamental part of my research here at UNC/NCSU and I will be forever grateful. In addition, I would like to recognize Steve Emanuel for his counsel and guidance in the workshop. Your assistance has made a tremendous difference in my success over the last five years. I would like to thank my committee members for their commitment to my research and education during my time at UNC/NCSU. I would like to recognize my colleagues in the Dayton Lab. Over the years, you have helped in my accomplishments, and I will always remember your kindness, your helpfulness, and your generous contributions toward my research. Additionally, I would like to acknowledge the Animal Studies Core Facility for their excellent technical assistance over the years. Lastly, I would like to thank all of the friends that I have made throughout my time at UNC/NCSU. You will be missed.

Table of Contents

List of Figures

List of Tables

List of Abbreviations

2-D	Two-Dimensional
3-D	Three-Dimensional
ARF	Acoustic Radiation Force
B-mode	Brightness Mode
BLA	Buried-Ligand Architecture
CARPA	Complement Activation-Related Pseudo-Allergy
CEF	Cumulative Error Function
CPS	Cadence Pulse Sequence
cRAD	Cyclo-Arg-Ala-Asp-D-Tyr-Cys
cRGD	Cyclo-Arg-Ala-Gly-Asp-D-Tyr-Cys
CT	Computed Tomography
DCE-PI	Dynamic Contrast-Enhanced Perfusion Imaging
DICOM	Digital Imaging and Communications in Medicine
DSPC	1,2 Distearoyl - sn - Glycero - 3 - Phosphocholine
ELA	Exposed-Ligand Architecture

FDA	Food and Drug Administration
FSA	Fibrosarcoma
GUI	Graphical User Interface
HUVEC	Human Umbilical Vein Endothelial Cell
IHC	Immunohistochemical
JPEG	Joint Photographic Experts Group
MAL-P2K	1,2 Distearoyl - sn - Glycero - 3 - Phosphoethanolamine - N - Maleimide (Polyethylene Glycol) - 2000
MCA	Microbubble Contrast Agent
MI	Mechanical Index
MRI	Magnetic Resonance Imaging
MVD	Micro Vessel Density
P2K	1,2 Distearoyl - sn - Glycero - 3 - Phosphoethanolmine - N - Methoxy - Polyethylene Glycol - 2000
PBS	Phosphate Buffered Saline
PDX	Patient-Derived Xenograft
PDX-NR	Patient-Derived Xenograft - Non-Responder
PDX-R	Patient-Derived Xenograft - Responder
PEG	Polyethylene Glycol
PET	Positron Emission Tomography

PRF	Pulse Repetition Frequency
PW	Pulsed Wave
RECIST	Response Evaluation Criteria in Solid Tumors
RLV	Relative Local Variability
ROI	Region of Interest
SPECT	Single-Photon Emission Computed Tomography
TIFF	Tagged Image File Format
TT20	Time to 20 Percent
US	Ultrasound
USMI	Ultrasonic Molecular Imaging
VEGF	Vascular Endothelial Growth Factor

CHAPTER 1

Hypotheses and Scope

1.1 Hypotheses

This dissertation supports the following hypotheses for *in vivo* ultrasonic molecular imaging experiments:

1. Producing size-selected microbubbles increases detection sensitivity.
2. Implementing a three-dimensional ultrasound platform improves our ability to quantify biomarker expression.
3. Using acoustic radiation force enhances microbubble targeting.
4. Creating buried-ligand microbubbles reduces immunogenic response and non-specific targeting.

These improved techniques will ultimately provide a basis of methods, which we will draw from to assess a tumor's response to therapy and compare it to more traditional methods.

1.2 Scope

This dissertation is organized in four main sections:

1. Overview and Introduction

2. Experimental Methods

3. Data Supporting the Hypotheses

4. Discussion and Conclusions

We begin in Chapter 2 where we discuss the motivation for this dissertation. This is followed by a high-level overview of both molecular imaging and ultrasonic molecular imaging in Chapter 3. In these chapters we emphasize current research and improvements that are to be addressed in this dissertation.

The experimental methods section begins in Chapter 4 where we discuss microbubble contrast agents, their role in ultrasound molecular imaging and their basic properties utilized in diagnostic ultrasound. In addition, a detailed overview of the experimental fabrication methods is presented. In Chapter 5 we discuss how microbubbles are detected using ultrasound technology. We provide a detailed description of the clinical imaging system and the 3-D platform in which experiments are performed throughout this dissertation. This chapter concludes by describing the procedures that were used in preparing animals for *in vivo* imaging. Chapter 6 provides an overview of the diagnostic techniques that we will utilize for our supporting data.

Data supporting this dissertation's hypotheses is provided in Chapter 7 through Chapter 12. First, Chapter 7 explores the effect of repeated administration of targeted microbubbles in molecular imaging experiments, which is a basis for the more advanced studies supporting this dissertation. Next, in Chapter 8, we evaluate the improvement in targeted microbubble sensitivity by using size-selected microbubbles. Chapter 9 focuses on improving our ability to comprehensively quantify biomarker expression through three-dimensional molecular imaging methods. Our focus shifts in Chapter 10 as we provide data that supports an improvement in microbubble targeting by utilizing acoustic energy to forcibly move microbubbles. Chapter 11 logically follows as

buried-ligand microbubbles are activated through acoustic radiation force and evaluated *in vivo* for the reduction of both immunogenic response, and non-specific targeting. Finally, in Chapter 12, we draw from our newly developed techniques to compare and contrast three different methods for evaluating a tumor's response to therapy: molecular imaging, perfusion imaging and volume measurements.

This dissertation is concluded in Chapter 13 as we discuss the data supporting our hypotheses in greater context. We will explore advantages of each technique, the shortcomings, future directions and possibilities for clinical translation.

CHAPTER 2

Overview of Cancer

2.1 Cancer Overview

Cancer is a disease that is characterized by the abnormal growth of cells, which is caused by changes in gene expression [1; 2; 3; 4]. Ultimately, this leads to a shift in the balance between cell proliferation and cell death, which may gradually evolve into a population of cells that invade and metastasize [1; 2; 3; 4]. If the spread of these cells is not controlled, then it can result in death [1; 2; 3; 4].

Cancer may be caused by environmental factors such as tobacco, chemicals, or radiation. However, cancer may also be caused by internal factors such as mutations, hormones, or immune conditions [1; 2; 3; 4]. Often, ten or more years may pass between exposure to external factors and the detection of cancer [4]. Cancer is typically treated with surgery, radiation, chemotherapy or some combination [4].

2.2 Cancer Statistics

Over the past 75 years, cancer death rates have steadily risen [1]. According to the American Cancer Society, one in every four deaths in the United States may be attributed to cancer, which is second only to heart disease [4]. In addition, it is estimated that in 2013, approximately 580,000 Americans will die as a result of cancer, which is almost 1,600 people per day [4]. Moreover, it is expected that in 2013 there will be more than 1.7 million new cancer cases (Table 2.1). Due to the high mortality rates

linked to cancer, there is an obvious need to understand the disease progression for better therapeutic options.

While the mortality rates are staggering, remarkable progress in drug discovery and innovation for cancer therapy has been made in the last decade [5]. For instance, the 5-year survival rate for all cancers that have been diagnosed between 2002 and 2008 is 68% [4]. This number has clearly improved since the 1970's when the same statistic was 49% [4]. However, there are certain types of cancer, like pancreatic adenocarcinoma, for which therapeutic options are limited and mostly ineffective. With just a 6% survival rate, most cancer patients that develop pancreatic cancer will die within the first year of their diagnosis [4]. The lack of progress in primary prevention, early diagnosis, and treatment for this type of cancer underscores the need for additional efforts in cancer research and is the primary motivation behind this dissertation.

Table 2.1: 2013 Cancer Facts and Figures from the American Cancer Society [4]

	Male		Female		Five Year
	New Cases	Deaths	New Cases	Deaths	Survival Rate (%)
Breast	2,240	410	232,340	39,620	89
Colon and Rectum	73,680	26,300	69,140	24,530	64
Esophagus	14,440	12,220	3,550	2,990	17
Kidney	40,430	8,780	24,720	4,900	71
Liver	22,720	14,890	7,920	6,780	15
Lung and Bronchus	118,080	87,260	110,110	72,220	16
Melanoma of the Skin	45,060	6,280	31,630	3,200	91
Non-Hodgkin Lymphoma	37,600	10,590	32,140	8,430	71
Oral Cavity and Pharynx	29,620	5,500	11,760	2,390	62
Ovary	NA	NA	22,240	14,030	44
Pancreas	22740	19,480	22,480	18,980	6
Prostate	238,590	29,720	NA	NA	99
Thyroid	14,910	810	45,310	1,040	98
Urinary	54,610	10,820	17,960	4,390	78
Uterine Corpus	NA	NA	49,560	8,190	82
All Cancer Types	**854,790**	**306,920**	**805,500**	**273,430**	**68**

2.3 Early Detection of Cancer

Discovering cancer at its earliest and most treatable stage provides patients with the greatest chance of survival [4; 1]. For instance, the 5-year survival rate for localized breast cancer is greater than 95%; however, this number drops to 78% for regional spread, and 23% for metastatic disease [1]. Screening is known to reduce the mortality for many types of cancer including breast, colon, rectum, and cervix [4; 1]. Furthermore, understanding any underlying changes in the breast or skin may result in the detection of these tumors at earlier stages [4]. Anatomical imaging, which includes computed tomography (CT), magnetic resonance imaging (MRI) and ultrasound (US), have greatly improved the accuracy of detecting and delineating tumors and play a key in early diagnosis of many types of cancer [6].

2.4 Personalized Cancer Therapy

Early diagnosis and individualized therapy are essential for the improvement of cancer therapy. Individualized therapy or personalized medicine is the tailoring of treatments based on the responsiveness of each individual tumor to a particular form of therapy. Standard cancer therapies typically suffer from low response rates and substantial side effects that may cause systemic toxicity [7]. Thus, with personalized medicine, patients are matched to the best drug for their disease, and doctors can avoid prescribing drugs that might cause serious harm in the wrong patients [8]. If a patient is a non-responder early in the course of therapy, this information can lead to better treatment efficacy. For instance, early assessment of tumor response to therapy could allow physicians to discontinue ineffective treatment and offer the patient more promising alternatives [9].

2.5 Response to Cancer Therapy

Understanding tumor biology is critical to understanding and identifying targets involved in tumor proliferation, invasion, and metastases, which are the motivating factors behind newly developed therapies. Therefore, it is critical to have tools that help identify patients who might benefit from a particular form of treatment [9]. Typically, the response of tumors to cancer therapy is evaluated with CT or MRI through anatomical imaging using the Response Evaluation Criteria in Solid Tumors (RECIST) criteria [10; 11; 7; 12]. The RECIST criteria focuses on how the tumor volume changes over time rather than evaluating the underlying molecular, cellular, and physiologic processes that govern therapeutic receptiveness [10].

There are several fundamental and practical limitations with using anatomic volume measurements as a means to gauge a tumor's response to therapy [7]. First, some cancers such as melanoma and renal cell carcinoma show no correlation between survival rate and tumor volume [13]. Second, the volume measurement criteria for response to therapy was designed primarily for cytotoxic agents, the efficacy of which is correlated with tumor regression. Thus, volume measurements for new therapies that are not cytocidal (cell killing) are typically not helpful when assessing early response to therapy [12]. Gefitinib, erlotinib, and bevacizumab are examples of drugs in which there are modest regressions or prolonged disease stability [12]. Furthermore, a phase III study evaluating the response of non-small cell lung cancer to erlotinib showed a median overall survival increase of 43% despite a volume response rate of less than 10% [14]. Finally, the application of using volume measurements clinically can be subjective. Due to the difficulty in delineating between post-treatment scar tissue and residual tumor mass, tumor volume can vary up to 100% for small tumors [15].

The limitations of using volume measurements has recently been overcome through the use of imaging modalities like positron emission tomography (PET) that allow for

functional and metabolic changes to be detected early in response to drug therapy [10]. Nuclear medicine, which includes including single-photon emission computed tomography (SPECT) and PET, offers a unique means to study cancer biology, thus improving our approach to cancer treatment [9]. In addition, tissue spectroscopy has improved the detection of gastrointestinal malignancies by evaluating relative changes in how light interacts with tissue [16]. It is clear that for a personalized approach to cancer therapy to be effective, underlying molecular, cellular, and physiologic processes that govern therapeutic receptiveness must be identified. Currently, there is a shift in radiation oncology towards a more biological and molecular approach to response evaluation [16; 6; 17]. Molecular imaging, for instance, promises improvements in focused and personalized therapy, and earlier treatment follow-up [18].

CHAPTER 3

Molecular Imaging Overview

3.1 Molecular Imaging

As discussed in Chapter 2, there is a demand for new strategies that focus on early disease detection through improved screening protocols as well as patient-specific treatment selection and therapy monitoring [7]. As a consequence, much research has focused on the development of new therapeutic strategies directed towards molecular biomarkers, an indicator for a particular disease state. With the development of these novel therapeutics, molecular imaging has emerged as a method to monitor the effect of these therapeutics through imaging techniques [5; 7].

Molecular imaging is a broad term for describing a technique designed to evaluate cellular and molecular activity in biological systems [19]. As a new paradigm for disease detection and response to therapy, the potential of molecular imaging is considerable. First, the imaging of molecular probes tend to be closely associated with the expressed phenotype of diseases, thus enabling direct associations between therapy and effect [11]. In addition, molecular imaging offers versatility for providing functional assessments of response to therapy by offering snapshots of the bioactivity of drug compounds over time [5]. Finally, molecular imaging provides assessments for response to therapy in humans and non-humans alike, which is essential for translational research [5].

Traditionally, the modalities associated with molecular imaging have been PET, SPECT and optical imaging [7]. A brief description of these techniques in the context

of molecular imaging of cancer are provided in the following subsections.

3.1.1 Metabolic Imaging with PET

PET is an imaging method which measures biochemical function of radio-labeled tracers rather than anatomical structure [7]. Metabolic imaging with PET using the glucose analog ^{18}F-fluorodeoxyglucose is currently the only widely-used application in clinical oncology [7]. This technique has the ability to quantify cellular metabolism and is primarily used for tumor staging [7]. However, PET imaging with ^{18}F-fluorodeoxyglucose has also been used for differentiating between malignant and benign tumors and identifying tumor recurrence and potential metastatic lesions [7]. Typically, metabolic imaging is regarded as a superior technique relative to anatomic-based imaging for response to therapy characterization. However, this type of imaging is non-specific, especially in inflamed areas, which limits its diagnostic efficacy [7]. While the application of PET using FDG in measuring therapeutic response has shown promise, specific clinical scenarios have not yet been standardized [7; 20; 21].

3.1.2 Imaging angiogenesis with PET

Tumor angiogenesis is the formation of capillaries and new blood vessels from surrounding host tissue to provide sufficient oxygen supply and nutrients to the tumor [1; 2]. VEGF and $\alpha_v\beta_3$ are integrins that are found in abundance on the surface of these proliferating endothelial cells; thus, they are specific markers for ongoing angiogenesis [1; 2]. $\alpha_v\beta_3$ has been the most thoroughly studied integrin due to the specificity of RGD to this particular integrin [22; 7]. Haubner *et al.* developed the first radio-labeled RGD peptide marker, which showed a strong affinity to angiogenic tumors [7; 23]. Initial studies using RGD tracers have been promising and histological studies have confirmed that there is good correlation between RGD uptake and $\alpha_v\beta_3$ expression making it a

good target for molecular imaging applications involving angiogenesis [7; 24; 25]. Currently, RGD as a PET tracer is not used for measuring therapeutic response, but the technique shows promise in monitoring anti-angiogenic activity and may have clinical relevance in the future [7].

3.1.3 Imaging angiogenesis with SPECT

SPECT is an imaging technique that detects low energy gamma rays that arise from radioisotope decay [26; 27; 28]. One advantage that SPECT has over PET imaging is the ability to detect multiple probes simultaneously [26; 27; 28]. Conversely, SPECT has lower sensitivities and typically requires higher doses, which mean more ionizing exposure for the patient [26; 27; 28]. In the context of clinical molecular imaging of cancer, SPECT has shown promise in the diagnosis of both colorectal and lung cancers [18]. Pre-clinically, SPECT has been used to investigate the VEGF-induced pathways associated with angiogenesis by using Technetium-99m that was tagged with VEGF-C [26; 29]. Furthermore, this particular technique has been successful in the pre-clinical monitoring of VEGF expression in response to anti-angiogenic therapy in rat glioma [26; 29]. While SPECT is used clinically for diagnosis, monitoring therapeutic response is not currently available with this imaging modality [26; 18].

3.1.4 Optical Imaging

Optical imaging is an approach to molecular imaging that uses either luminescence or fluorescence detection as a means for evaluating molecular events [26]. Clinical applications of optical imaging techniques are typically limited to the skin surface due to the limited depth penetration through human tissue [18]. Raman spectrophotometry is an emerging molecular imaging technique used clinically for monitoring atherosclerosis-associated inflammation and imaging of porphyrin (blue fluorescence) accumulation

in highly-proliferating cancer cells [18; 30; 31]. However, due to the depth penetration restriction, optical imaging applications have primarily been pre-clinically oriented through the evaluation of new molecular targets and pre-clinical drug evaluations [18]. Optical imaging is now a well-established methodology in pharmacology for evaluating therapeutic effects on cancer cell lines treated with various compounds [26; 32; 33]. Since optical imaging typically requires less equipment and expertise, it is often more cost-effective than technologies like PET and SPECT [26]. While this approach has clinical limitations, it remains a valuable tool for preclinical evaluation of cancer therapeutics due to its high specificity [26].

Clinical molecular imaging is typically performed with PET or SPECT [18]. Ultimately, it is hoped that one or all of these techniques will help doctors to visualize the expression and activity of particular molecules, cells and biological processes that influence the behavior of tumors [16]. The development of molecular imaging both clinically and pre-clinically is in its infancy and could ultimately yield tremendous patient benefit.

3.2 Ultrasonic Molecular Imaging Introduction

Medical US has long been used in clinical applications both as a primary modality and as a supplement to other diagnostic procedures. The basis for US imaging is the transmission of high frequency (megaHertz) sound waves that propagate through tissue. These sound waves backscatter from the interfaces between tissue components with different acoustic properties and are detected by the imaging system, allowing the creation of images based on tissue characteristics and spatial location. Thus, traditional US has focused primarily on the imaging of anatomical structures and analysis of blood flow in large vessels. Until recently, there has been no mechanism by which US has been able to detect changes at the cellular and molecular level.

Over the past decade, US has gained interest in the area of molecular imaging due to the practical advantages over traditional molecular imaging modalities: it is inexpensive, safe (no ionizing radiation), portable (bedside support), and readily available with fast acquisition times [19]. With ever growing health care costs, contrast-enhanced US imaging is gaining momentum in the field of molecular cancer research as an alternative to more expensive imaging modalities.

The ability to detect acoustically active microbubble contrast agents (MCA) designed to selectively adhere to biomarkers expressed on the endothelium is the basis for ultrasonic molecular imaging (USMI) [1; 7]. MCAs are intravascular, thus the specific targets for molecular imaging must be present in the vascular space and are typically expressed on the luminal vessel surface [34]. In USMI, targeted microbubbles accumulate at the target location and enhance the areas of diseased tissue that are not detectable with traditional US imaging. As an example of its utility, USMI can help assess whether and to what extent a specific target (example: angiogenesis) is expressed in tumor neovasculature [35]. This includes both the assessment of the presence of the targets as well as their spatial distribution [35]. Since USMI has the potential to provide information prior to the appearance of gross phenotypic changes, it is proposed that this method can facilitate early assessment of disease progression or response to therapy [19].

Although significant advances in molecular imaging have been made over the last decade, there are many challenges that must be addressed to advance the utility of USMI. The ultimate goal of molecular imaging is to determine the degree to which biomarkers are expressed by the target tissue. Therefore, it is essential that targeted microbubbles adhere in quantities that produce backscattered intensities in greater

magnitude than the signal intensities from non-specific targeting. Given this requirement, research has primarily focused on improving the sensitivity to bound microbubbles, improving the ability to quantify biomarker expression, increasing the quantity of targeted microbubbles retained at the site of pathology, and improving microbubble architecture to minimize the non-specific retention of microbubbles and immunogenic response.

3.2.1 Sensitivity Improvement

Targeted microbubbles in molecular imaging experiments typically have sub-optimal retention. Rather than increase the number of microbubbles at the target location through increased dose, many groups are evaluating the effect of increasing the backscattered signal for each microbubble, thus improving the sensitivity of the system to targeted agents.

Rayleigh-Scattering theory of sub-wavelength particles predicts an increase in US backscatter intensity as a function of the scattering cross-section, a metric directly related to the size of the microbubble scatterer [36; 37]. Due to the significance of microbubble size in the acoustic response, recent interest has involved new production and sorting methods for microbubbles including centrifugation techniques, microfluidics, and electrohydrodynamic atomization [38; 39; 40; 41; 42]. Each size-selection method has resulted in a substantial improvement in acoustic response, which may improve sensitivity to targeted microbubbles.

For over a decade, targeted imaging applications have primarily used mechanically agitated MCAs with a relatively small mean diameter ($\sim$1 μm). The resultant small populations of adherent MCAs provide weak backscatter intensity and limit imaging sensitivity in molecular imaging [19]. We hypothesize that the improvement of contrast sensitivity in molecular imaging applications can be achieved by increasing the

mean diameter in MCA populations through centrifugation methods. To our knowledge, there have been no molecular imaging studies that have incorporated size-selected microbubbles to improve sensitivity to targeted agents.

3.2.2 Quantification Improvement

Perhaps the greatest challenge in USMI is the ability to quantify biomarker expression. Even though the precise relationship between the number and distribution of retained microbubbles and the resulting acoustic response is still unknown, there have been significant advances in other areas of quantification. One of the limitations of preclinical USMI is that it lacks a comprehensive field-of-view compared to other imaging modalities.

Until recently, traditional brightness mode (b-mode), or non-targeted contrast imaging, has been mainly two-dimensional (2-D). This has not been a limiting factor for applications in which the user is imaging anatomical structures, because adjusting the transducer manually can vary the image plane. Since molecular imaging with US typically uses a more precise subtraction method for quantifying molecular marker expression, image acquisitions are obtained by placing the transducer in a fixed clamp on an anesthetized animal [43; 44]. Therefore, it is nearly impossible to obtain volumetric molecular imaging information by manually translating the transducer as with traditional b-mode applications.

Traditional 2-D USMI has provided valuable insight into the detection of biomolecular markers. Unfortunately, it is difficult to achieve accurate quantitative information of molecular changes in heterogeneous tissue with only a single 2-D image plane. Until recently, three-dimensional (3-D) USMI has been unavailable due to the absence of contrast agent detection strategies implemented in conjunction with 2-D arrays or with elevational scanning of linear arrays. However, our unique setup allows us to obtain

volumetric acquisitions with a clinical US system in a contrast detection mode by mechanically scanning the transducer elevationally across the tumor, which is convenient given the requirement of a fixed clamp setup. We hypothesize that using this novel 3-D approach may provide a more robust assessment of molecular marker expression throughout the tumors than traditional 2-D US.

3.2.3 Improvement in Quantity of Targeted MCAs

The magnitude of the detected signal correlates well with the quantity of adherent microbubbles. Prior studies assessing the adhesion of targeted microbubbles have observed sub-optimal retention (∼several bubbles per mm^3) [45; 44]. Thus, increasing the quantity of targeted microbubbles may result in an increase in the detected signal and may improve the ability to detect the pathology.

Over the past decade, *in vivo* USMI research has relied on passive targeting as the basis for this technique. Passive targeting is microbubble adherence that does not require any additional forces for binding. Unfortunately, passive targeting has resulted in poor binding efficiency, which necessitates signal amplification in targeted imaging applications. A transducer directing non-destructive energy perpendicular to the blood flow can displace moving MCAs to the wall of the vessel opposite the sound source, thus increasing the probability of microbubble-endothelium interactions [46]. Forcibly displacing MCAs to the wall of the vessel would make it possible to increase the concentration of MCAs during USMI experiments, which has been hypothesized but not demonstrated *in vivo* with a clinical US system [46; 47; 48]. Improved targeting via acoustic radiation force (ARF) techniques have been observed *in vivo* acoustically and with intravital microscopy [48; 49]. Due to the potential significant increases in MCA adhesion, the application of ARF-enhanced USMI of angiogenesis *in vivo* with a clinical US system is of great value.

3.2.4 Immunogenic Response Minimization

In typical USMI experiments, the microbubble architecture utilizes a targeted ligand that is exposed to the surrounding environment. This presents the threat of increased interactions with plasma components that may lead to non-specific adhesion. In addition, there may be an increased risk in undesired immunogenic reactions. Ultimately, the traditional exposed-ligand architecture (ELA) is easy to manufacture and use in a molecular imaging experiment; however, the trade-off is a reduction in our ability to specifically identify our target.

Minimizing the non-specific retention of microbubbles has recently been realized using a buried-ligand architecture (BLA) scheme [50; 51; 52]. Microbubbles typically consist of a lipid shell with a polyethylene glycol (PEG) brush to prevent surface adsorption and improve solubility. ELA microbubbles for molecular imaging use this architecture as a basis with a targeting ligand tethered to the PEG brush for surface exposure. BLA microbubbles, however, use a more complex flexible PEG surface mechanism for the purpose of hiding the ligand from the surrounding environment. Buried-ligand microbubbles are introduced to the vascular system and subsequently activated with an ARF pulse, which reveals the buried ligand to the target site. This method has shown a significant improvement over conventional targeted microbubbles in avoiding immunogenic responses and improving non-specific targeting [51; 52].

Previous *in vitro* studies with buried-ligand microbubbles have shown that it is feasible to target cells with the application of ARF [52]. However, prior studies have not demonstrated *in vivo* USMI with buried-ligand microbubbles. We hypothesize that buried-ligand architectures, in conjunction with ARF, can be used for *in vivo* molecular imaging of tumor neovasculature.

3.3 Summary

Early studies indicate that USMI has significant diagnostic potential in the assessment of disease progression and response to therapy. At the pre-clinical level, molecular imaging has already led to a greater understanding of the pathophysiologic mechanisms of various types of diseased tissue. In addition, USMI has shown much progress in the area of pre-clinical drug efficacy evaluations, which could be expanded to more efficient methods of cancer therapeutic development. For example, Pysz and colleagues recently used microbubbles targeted to a kinase insert domain receptor to monitor anti-angiogenic therapy (against Vascular Endothelial Growth Factor - VEGFR-2) in human colon tumor-bearing mice [53]. In another study, USMI was successfully used to monitor the effects of an anti-angiogenic treatment on the expression of both VEGFR-2 and $\alpha_{\mathrm{v}}\beta_3$ integrin in squamous cell carcinoma xenografts [54]. Molecular imaging with US research is only in its infancy, but this type of imaging modality could yield tremendous patient benefits in the form of earlier tumor detection, treatment response monitoring, and an individualized approach to various forms of therapy.

CHAPTER 4

Microbubble Contrast Agents Overview

4.1 Microbubble Contrast Agents

In general, blood is a weak US scatterer, thus vascular diagnostic applications (example: echocardiography) can be challenging especially with larger patients where US attenuation may dominate. Contrast agents help to improve on this shortcoming by enhancing the visualization of blood flow, thus improving the quality of diagnostics.

The use of contrast agents for US was first reported in 1968 when Gramiak and Shah discovered that there was an increased backscatter of US caused by injected microbubbles [37]. Comprehensively, this mechanism may be described with the Rayleigh-Plesset model as well as Rayleigh scattering theory of a sub-wavelength spherical body [37]. Using these models, the microbubble oscillatory dynamics in an ultrasound field may be described by mechanisms such as compressibility, density of the mediums, elasticity of the shell, and viscosity of the shell [37; 36]. The behavior of the microbubble in an ultrasound field is quite complicated and beyond the scope of this thesis. However, it is important to illustrate that there are significant differences in density and compressibility between a microbubble and the blood that surrounds it. Ultimately, this results in ultrasound scattering that is several orders of magnitude different for a microbubble relative to an equivalent volume of tissue or blood [37; 36].

Over the last several decades, there has been much effort in the research of contrast media for ultrasound with emphasis on producing a stable and effective contrast agent

[37; 36]. Contrast agents typically used in US studies include perfluorocarbon emulsion nanoparticles [55], echogenic liposomes [56; 57; 58], and MCAs [59; 60; 61], with the most commonly used agent being the microbubble (Figure 4.1).

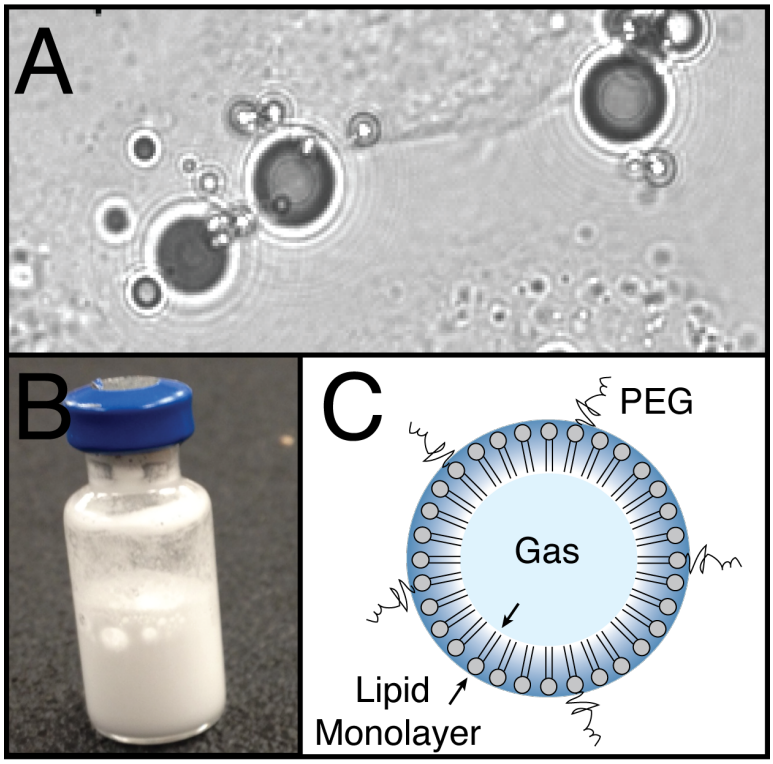

Figure 4.1: Microbubble Examples A: A polydisperse distribution of various sized microbubbles as viewed in a bright-field microscope. B: A recently agitated 3 mL vial of microbubbles suspended in a mixed solution of PBS, propylene glycol, and glycerol. C: A high-level illustration presenting the typical components of a lipid monolayer microbubble.

4.1.1 Microbubbles for Perfusion Imaging

In order to take advantage of the contrast mechanism, microbubbles are composed of a gas core that is typically encapsulated by phospholipid-based, albumin or polymer shell [62; 63; 64; 36; 65]. A microbubble's gas core is usually comprised of a high molecular

weight gas (Example: decafluorobutane) in order to prevent the gas from diffusing out of the microbubble [65; 66]. The minimization of dissolution allows the microbubble to persist in the bloodstream for many minutes at a time, which is a requirement for most diagnostic applications [36]. Finally, most lipid-based microbubbles are fitted with a PEG brush to prevent microbubbles from coalescing into larger microbubbles and for purposes of solubility [65; 66].

Microbubbles are inherently blood-pool agents, and thus are confined to the vascular compartment. In the United States, the primary function of perfusion-based microbubbles is in echocardiography where they help to delineate endocardial borders for more accurate diagnosis of heart disease [67]. Microbubbles have been used in applications such as the assessment of systolic function and left ventricular volume, and for identifying myocardial infarction and coronary artery stenoses [68; 69; 70; 71]. More recently, perfusion-based contrast agents have been used to quantify blood flow metrics in cancer research [72; 73; 74].

4.1.2 Microbubbles for Molecular Imaging

Targeted microbubbles are similar to microbubbles used for contrast-enhanced echocardiography in that they are composed of a gas core and are usually stabilized by a lipid, protein or polymer shell. However, unlike these perfusion agents, targeted microbubbles contain high-affinity adhesion ligands (such as an antibody, peptide etc.), which are specific for a particular disease epitope [65; 66]. In typical microbubble architectures, these ligands are attached to the PEG brush and interact with the target biomarkers away from the bubble surface [75].

Developments in USMI, which utilize targeted microbubbles, provide a range of new applications for contrast-enhanced ultrasonography, including, but not limited to, the diagnosis of myocarditis, evaluation of myocardial infarction, assessment of transplant

rejection, ischemic memory imaging, and early-stage detection and treatment of solid tumors [76; 77; 78].

4.2 Microbubble Safety

Microbubble contrast agents are typically smaller than red blood cells ($< 8\ \mu$m) in order to pass through the pulmonary capillary bed after intravenous injection [36]. After the intravenous bolus injection, microbubbles are distributed uniformly throughout the peripheral circulatory system [36]. After this preliminary phase, microbubbles typically show uptake in the liver and spleen due to phagocytic cells of the reticuloendothelial system [36]. The stabilizing components of microbubbles are filtered by the kidney and eliminated by the liver with the phospholipids of the shell entering normal metabolism [36]. Finally, the gas component of the microbubble contrast agents is expelled by the lungs after the microbubbles have persisted for a period of time, typically a few minutes [36].

Microbubble contrast agents are safe with a low incidence of side-effects [79; 80; 36]. Extensive studies investigating the use of perfusion-based microbubbles for echocardiography have concluded that adverse reactions in patients are rare [79; 80; 36]. However, it should be noted that individual cases of dyspnea, chest pain, and nausea have been reported [79; 80]. In addition, there have been reports of tingling, numbness and dizziness after administration [79; 80]. Microbubbles are not inherently nephrotoxic or cardiotoxic, but there have been cases of severe allergic reactions [79; 80]. In a 2008 study, over 200,000 patients were evaluated with the contrast agent Definity® (Lantheus Medical Imaging, Billerica, MA). Of the 200,000 patients, 16 allergic reactions were reported ($\sim$0.3%), which is an incidence that is much lower than current CT-based or MR-based contrast agents [79; 80; 36]. While there have been rare instances of side-effects using microbubbles, it is clear that the potential clinical benefits outweigh the

potential for adverse reactions.

4.3 Experimental Methods for MCA Fabrication

This section details the process in which lipid solutions were prepared for the experiments described in this dissertation. Recipes for perfusion agents, non-targeted agents (control) and targeted agents are presented and the manufacturing processes for obtaining various populations are discussed.

4.3.1 Perfusion Agent Recipe

MCAs for perfusion-based experiments were created using a 9:1 molar ratio of 1,2 Distearoyl - sn - Glycero - 3 - Phosphocholine (DSPC) (Avanti Polar Lipids, Alabaster, AL) and 1,2 Distearoyl - sn - Glycero - 3 - Phosphoethanolmine - N - Methoxy - PEG - 2000 (P2K) (Avanti Polar Lipids - Alabaster, AL) in a 90 mL buffer solution (Figure 4.2A). The buffer solution was comprised of 80% phosphate buffered saline (PBS), 15% propylene glycol and 5% glycerol and the final lipid concentration was 1.0 $\frac{\text{mg}}{\text{mL}}$.

4.3.2 Non-targeted Agent Recipe

Non-targeted (control) lipid solutions for molecular imaging experiments were created using DSPC, P2K, and 1,2 Distearoyl - sn - Glycero - 3 -Phosphoethanolamine - N - Maleimide (PEG)-2000 (MAL-P2K) cross-linked to a cRAD peptide (Cyclo-Arg-Ala-Asp-D-Tyr-Cys) in a 18:1:1 molar ratio respectively with a total lipid concentration of 1.0 $\frac{\text{mg}}{\text{mL}}$. Finally, the lipids were suspended in 90 mL of sterile PBS (Figure 4.2C).

4.3.3 Targeted Agent Recipe

Microbubbles designed to target $\alpha_{\text{v}}\beta_3$ integrins for molecular imaging experiments were created with a 18:1:1 molar ratio of DSPC, P2K, and MAL-P2K cross-linked to a cRGD peptide (Cyclo-Arg-Ala-Gly-Asp-D-Tyr-Cys) (Peptides International - Louisville, KY)

(Figure 4.2B). Similar to the perfusion and non-targeted agents, lipids were fabricated with a total lipid concentration of 1.0 $\frac{\text{mg}}{\text{mL}}$ in a 90 mL buffer solution of sterile PBS. The chosen cRGD peptide has previously been shown to target $\alpha_v\beta_3$-expressing vasculature, which is characteristic of angiogenic tumors [22; 38; 81].

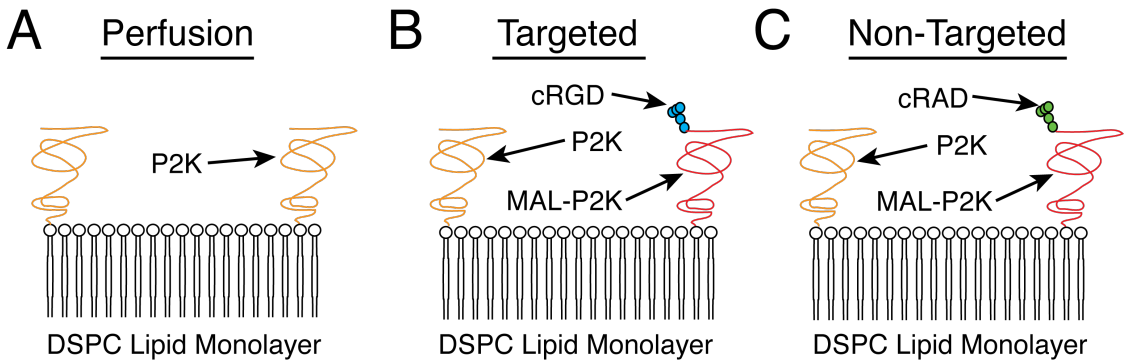

Figure 4.2: Illustrations of the various microbubble architectures used in this dissertation. A: Perfusion-based microbubble architecture consisting of a DSPC lipid monolayer and a P2K brush layer. B: Targeted microbubble architecture consisting of a DSPC lipid monolayer, a P2K brush layer, and a cRGD peptide linked to a MAL-P2K. C: Non-Targeted microbubble architecture consisting of a DSPC lipid monolayer, a P2K brush layer, and a cRAD peptide linked to a MAL-P2K.

4.3.4 Lipid Preparation Procedure

Briefly, powdered lipids were measured to precise weights using a high precision balance (AB204-S, Mettler Toledo, Greifensee, Switzerland) with the previously described recipes. The lipids were placed into a 100 mL glass vial with 2 mL of chloroform, an organic compound in which lipids easily dissolve. Next, the lipids were thoroughly agitated with a vortex mixer until all lipids were visibly dissolved in the chloroform. Then, the chloroform was evaporated in the presence of slow-flowing nitrogen and simultaneous agitation with the vortex mixer. After the chloroform was removed from the container, the dried lipids were added to an oven, under vacuum, at 55°C for 30 minutes to remove any remaining chloroform from the container. Finally, the buffer

solution was added to the lipid container and introduced to a sonication (Branson 2510, Branson Ultrasonics, Danbury, CT) bath for 30 minutes at 55°C for re-hydration.

4.3.5 Unsorted Microbubble Populations

Unsorted microbubbles were produced using mechanical agitation, which is the fabrication method that is utilized for the FDA - approved contrast agent Definity®. First, 1.5 mL of the appropriate lipid solution was transferred to a 3 mL serum vial. The vial was stoppered and capped and decafluorobutane was exchanged with the air in the vial headspace using a custom vacuum apparatus. The vial was shaken vigorously for 45 seconds at 4500 rotations per minute using a mixer (Vialmix, Bristol-Myers Squibb Medical Imaging, North Billerica, MA) to produce the characteristic polydisperse distribution for perfusion-based *in vivo* experiments.

4.3.6 Sorted Microbubble Populations

The specific procedure for sorting microbubbles is presented in this section as an itemized list of steps and as a flow chart in Figure 4.4. The method used to create various size distributions is based on differences in buoyancy forces for different microbubble sizes and was recently described in detail by Feshitan and colleagues [41]. Using this technique, sorted distributions with mean diameters of $\sim$1.0 μm, $\sim$1.6 μm, and $\sim$3.5 μm may be obtained (Figure 4.3). It is important to note that the mode of the distribution is often larger than the mean diameter of the microbubble population. This is due to imperfections of the technique, which limit the amount of small microbubbles that are filtered during the isolation technique. Thus, the residual small populations that remain after centrifugation typically reduces the mean of the size distribution to a value that is less than the mode of the same distribution.

Microbubble Production

A large quantity of lipid solution is required (typically 90 mL or more at a minimum concentration of 1.0 $\frac{\text{mg}}{\text{mL}}$) to yield the appropriate number of sorted microbubbles. This lipid solution is prepared via the methods described in section 4.3.4. After the lipid solution is prepared, different diameter distributions are preferentially selected using a multi-step centrifugation procedure as follows:

1. Lipids are completely dissolved in the buffer solution by raising the solution temperature to 55°C.

2. The beaker of lipids is transferred to the sonic dismembrator apparatus. The sonicator tip is placed such that it is ∼1 mm below the surface of the lipid solution.

3. The sonic dismembrator is set to a power of 70% and a time of 15 seconds.

4. A large collection of microbubbles is generated via acoustic emulsification by turning the sonicator on while flowing decafluorobutane over the surface of the solution.

5. The resulting microbubbles (in solution) are collected using 30 mL syringes.

6. The 30 mL syringes are placed in a centrifuge for 10 minutes at 300 G.

7. After 10 minutes, a microbubble "cake" forms toward the plunger of the syringe. The buffer solution is slowly pushed out of the syringe (everything but the microbubble "cake") into a beaker for recycling.

8. Approximately 1 mL of buffer solution is added to the syringe containing the microbubble "cake" for every 1 mL of microbubbles produced.

9. Using the recycled lipid solution, steps 1 through 8 are repeated until at least 30 mL of microbubbles have been collected.

3.5 Micron Diameter Isolation

1. The well-mixed 30 mL syringe of microbubbles is placed into a centrifuge for 1 min at 30 G.

2. The resulting microbubble solution is slowly pushed out into another 30 mL syringe and the microbubble "cake" is discarded.

3. Filtered PBS is added to the syringe containing the solution until there is a final volume of 30 mL.

4. The 30 mL syringe of microbubbles is placed into a centrifuge for 1 min at 70 G.

5. The resulting microbubble solution is slowly pushed out into another 30 mL syringe and the microbubble "cake" is discarded.

6. Filtered PBS is added to the syringe containing the solution until there is a final volume of 30 mL.

7. The 30 mL syringe of microbubbles is placed into a centrifuge for 1 min at 160 G.

8. The resulting microbubble solution is slowly pushed out into another 30 mL syringe for $\sim$1.0 μm and $\sim$1.6 μm selection.

9. The "cake" is transferred to a 5 mL syringe for the selection of $\sim$3.5 μm diameter microbubbles.

10. Filtered PBS is added to the syringe until there is a final volume of 5 mL.

11. The 5 mL syringe is placed in centrifuge for 1 min at 120 G.

12. The resultant microbubble solution is slowly pushed out of the syringe while the microbubble "cake" is retained.

13. Steps 10 through 12 are repeated until the resultant solution is completely clear.

14. The final microbubble population is stored in a 3 mL syringe with no headspace. The size distribution is described in Figure 4.3C.

1.6 Micron Diameter Isolation

1. Using the resultant microbubble solution from step 8 above, the 30 mL syringe is placed in the centrifuge for 1 min at 270 G.

2. The resulting microbubble solution is slowly pushed out into another 30 mL syringe for $\sim$1.0 μm size-selection.

3. Filtered PBS is added to the syringe containing the microbubble "cake" until there is a final volume of 30 mL.

4. The 30 mL syringe is placed in the centrifuge for 1 min at 270 G.

5. The resultant microbubble solution is slowly pushed out of the syringe and discarded while the microbubble "cake" is retained.

6. Steps 3 through 5 are repeated until the resultant solution is completely clear.

7. The final microbubble population is stored in a 3 mL syringe with no headspace. The size distribution is described in Figure 4.3B.

1.0 Micron Diameter Isolation

1. Using the resultant microbubble solution from step 2 above, the 30 mL syringe is placed in the centrifuge for 10 min at 300 G.

2. The resulting microbubble solution is slowly pushed out and discarded.

3. The microbubble "cake" is retained and stored in a 3 mL syringe with no headspace. The size distribution is described in Figure 4.3A.

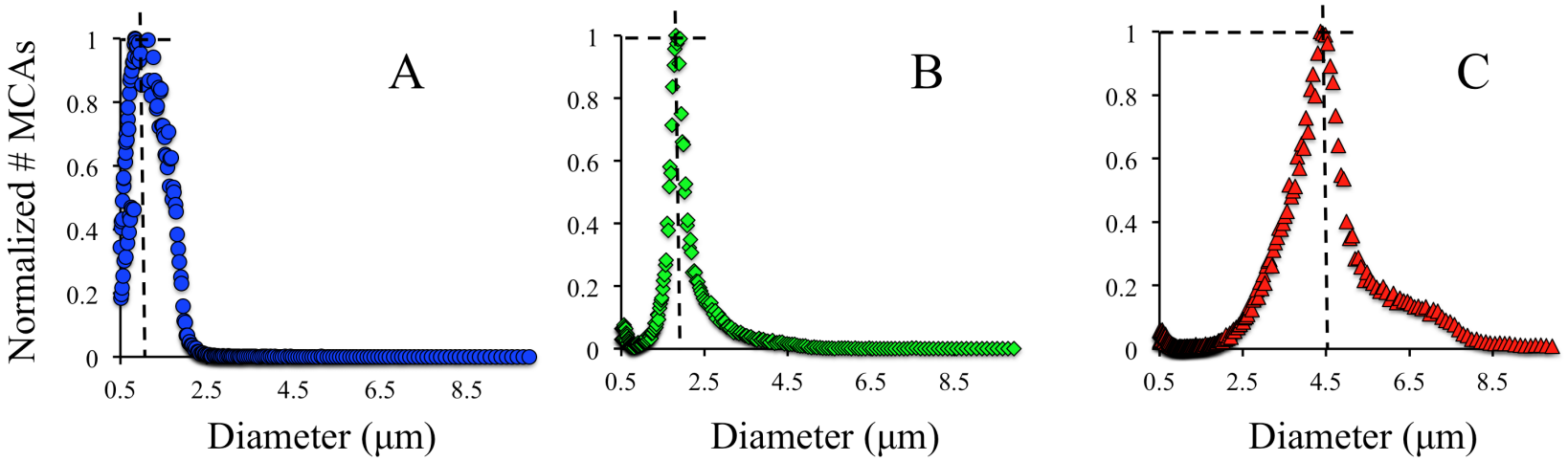

Figure 4.3: A: Resultant 1.0 μm Diameter Size Distribution. B: Resultant 1.6 μm Diameter Size Distribution. C: Resultant 3.5 μm Diameter Size Distribution. Note: The dotted lines indicate the mode of the distribution, not the mean diameter.

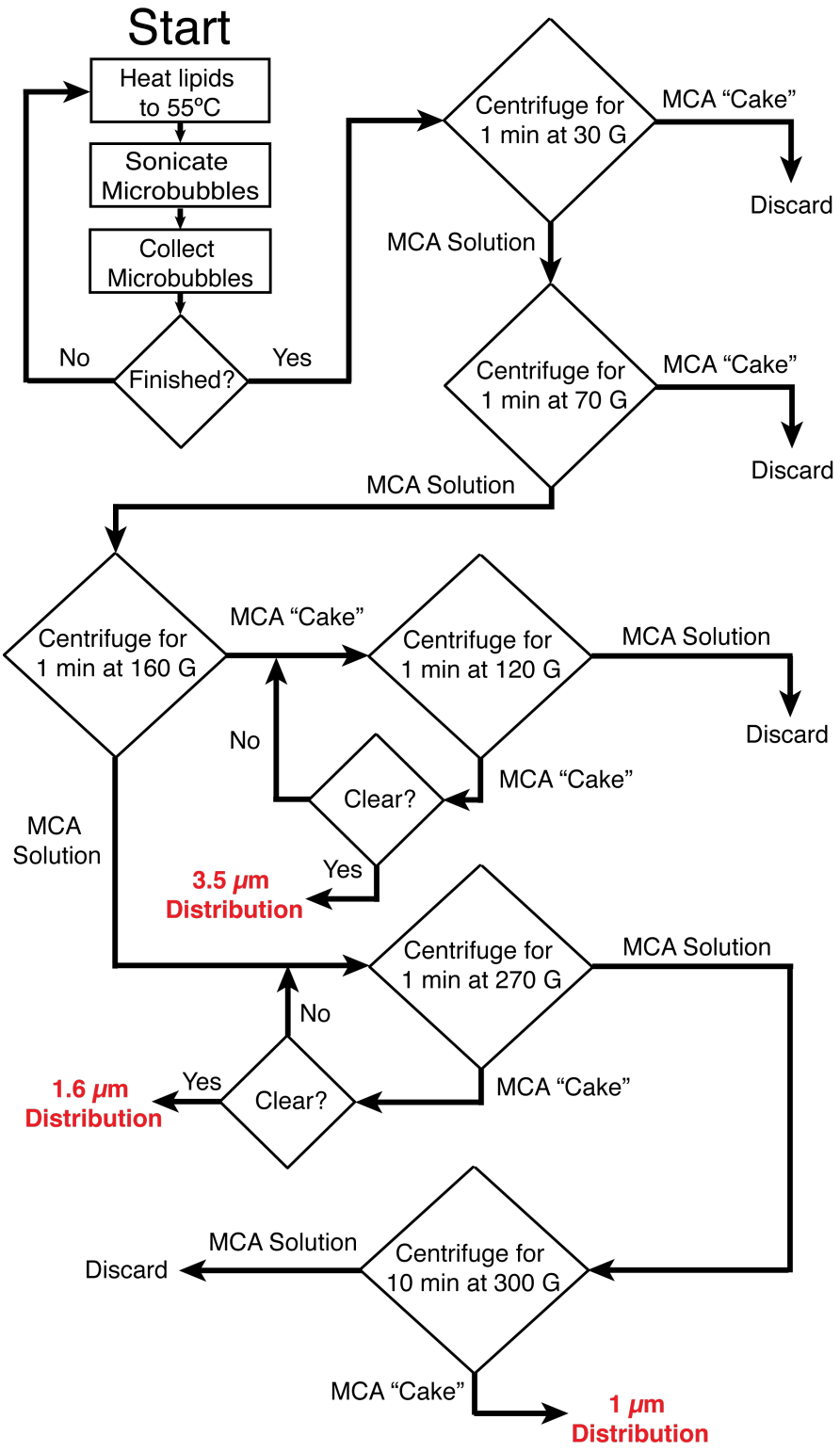

Figure 4.4: MCA size-selection flow chart based on the procedures in 4.3.6.

CHAPTER 5

Imaging and Animal Preparation

5.1 Imaging Contrast Agents

Lipid-encapsulated microbubbles oscillate in the presence of an acoustic wave [36; 82]. When a microbubble is insonified, it expands and contracts in rhythm with the negative and positive pressure half cycles respectively. In general, the microbubble is analogous to a spring-mass system where the balance of forces are governed by the restoring force of the encapsulated gas and the inertia of the surrounding fluid pushing on the shell surface [36].

Microbubbles respond non-linearly to acoustic pulses even at low energies, unlike tissue [36]. The non-linear behavior of microbubbles allows for the use of various pulsing and signal processing strategies to detect the signal backscattered from contrast agents and segment it from tissue [36; 82]. Furthermore, these unique non-linear properties enable imaging sensitivity on the order of a single microbubble [83]. This ultimately provides a high contrast-to-noise ratio for use in a variety of advanced diagnostic procedures. This chapter describes common imaging techniques that are employed in US systems to separate microbubble signals from tissue along with experimental details on the imaging system and 3-D platform utilized herein.

5.1.1 Amplitude Modulation Imaging Overview

Amplitude modulation is a contrast agent imaging technique that utilizes the dependence of the microbubble response on the amplitude of the transmitted pulse [36; 84]. A brief and generalized description of this technique is provided in this section (Figure 5.1). First, two different interrogation pulses are transmitted with different amplitudes, but with the same frequency [36; 84]. Typically, the second pulse has an amplitude that is twice the amplitude of the first pulse [36; 84]. The imaging system then stores the backscattered intensity from the interrogated region for each of the two pulses. Post-processing is then performed on the two signals. The first stored echo is multiplied by a factor of two before it is subtracted from the second stored echo sequence [36; 84]. This technique has two different outcomes for linear scatterers and non-linear scatterers. For linear scatterers, or stationary tissue (at low pressure amplitudes), the second echo will be equivalent to two times the first echo; therefore, the final subtracted signal will equate to a zero value. In other words, the two-pulse technique will ultimately produce zero signal for linear or tissue-like scatterers. For non-linear scatterers, however, echoes produced by the two pulses will not subtract to zero. The residual signal created after post-processing represents the non-linear signal produced by the interrogated MCAs. The one disadvantage of this technique over conventional b-mode imaging is that the frame rate is sacrificed due to the requirement of multiple transmit pulses, which may sacrifice our ability to detect fast moving objects with this technique.

5.1.2 Pulse Inversion Imaging Overview

Pulse inversion is another common technique implemented in currently available US systems (Figure 5.2). This technique is similar to amplitude modulation in that it involves two transmit pulses and some additional processing. As with amplitude modulation, a two-cycle pulse is transmitted and the return echo is stored [36; 85; 82].

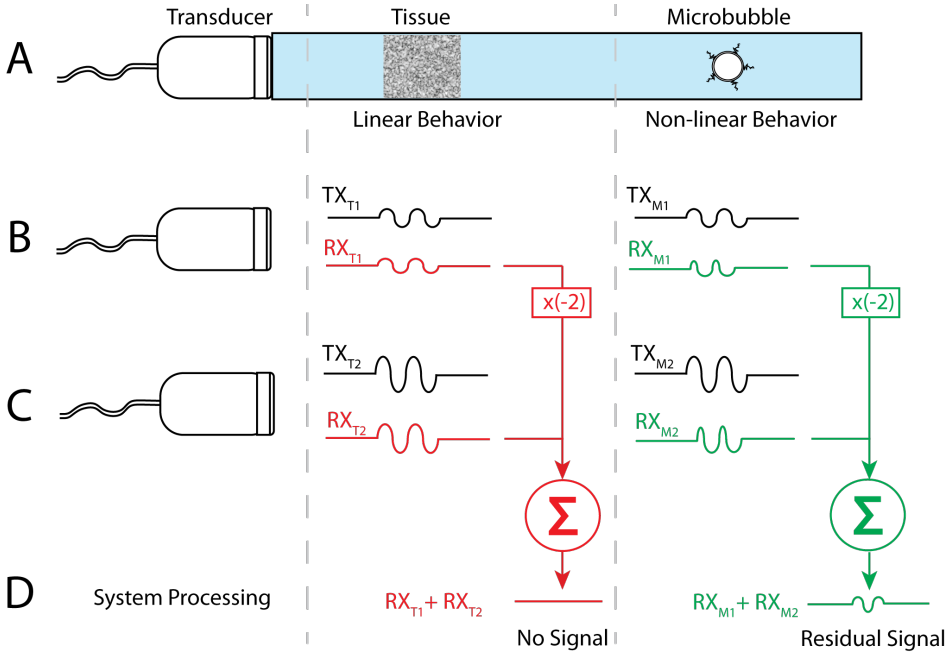

Figure 5.1: High-level description of the amplitude modulation imaging technique. A: Pictorial description of the setup to describe amplitude modulation. In this panel a transducer interrogates both a tissue region and a microbubble region. At low pressure amplitudes, the tissue will behave as a linear target and the microbubble will behave non-linearly. B: A two-cycle pulse is transmitted at amplitude A and the return echo is stored for both tissue and microbubbles. C: Again, a two-cycle pulse is transmitted only this time the amplitude of the signal is 2A. The return echo is stored for both tissue and microbubbles. D: The receive signal from the first pulse sequence is multiplied by minus two and then added to the second receive signal. The final result for the tissue region will be zero whereas the result for the microbubble region will equate to a non-zero value.

Then, another two-cycle pulse is transmitted only this time it is inverted relative to the initial transmitted pulse [36; 85; 82]. The echo from the inverted signal is stored and is added to the received signal from the initial pulse [36; 85; 82]. Due to the non-linearity of microbubbles, the echo from the inverted pulse will differ from echo from the initial pulse, which will sum to a non-zero value. The linear scatterers, however, will behave the same for both the first and inverted pulses and thus sum to zero.

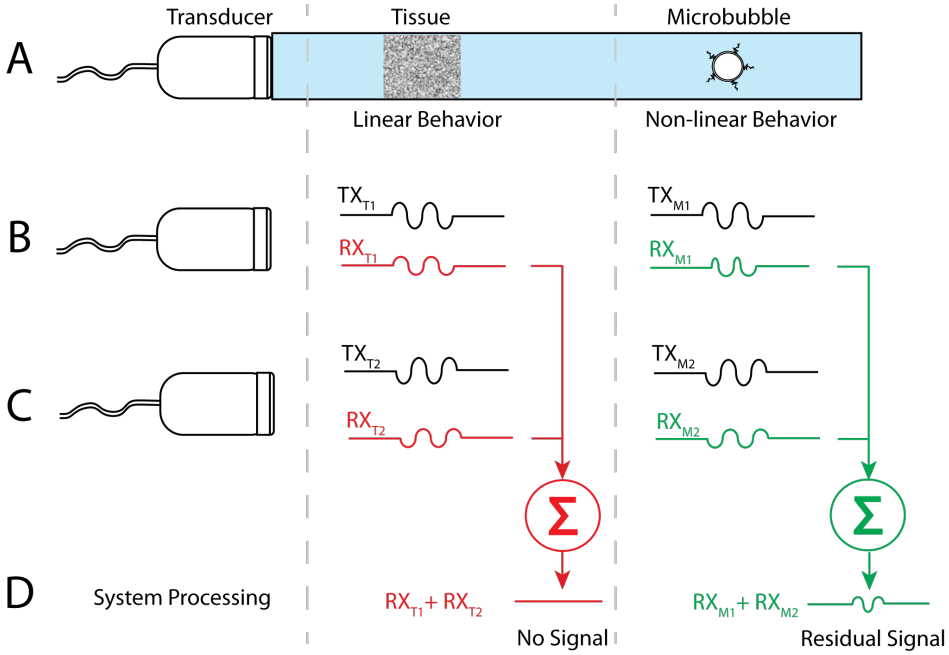

Figure 5.2: High-level description of the pulse inversion imaging technique. A: Pictorial description of the setup to describe pulse inversion. In this panel, a transducer interrogates both a tissue region and a microbubble region. At low pressure amplitudes, the tissue will behave as a linear target and the microbubble will behave non-linearly. B: A two-cycle pulse is transmitted and the return echo is stored for both tissue and microbubbles. C: Again, a two-cycle pulse is transmitted only this time the signal is inverted from B. The return echo is stored for both tissue and microbubbles. D: The two receive signals for tissue are summed and equate to zero. The two microbubbles, being non-linear, sum to a non-zero value.

5.1.3 CPS Imaging Overview

Cadence Pulse Sequence (CPS) imaging is a complex contrast-specific imaging technique that was developed by Siemens in the 1990's [36; 86]. In general, this technique uses both amplitude modulation and pulse inversion, the two previously described techniques, to achieve separation of tissue and non-linear microbubbles. Employing this technique provides high sensitivity for microbubble detection, but at the expense of frame-rate due to the multi-pulse strategy (Figure 5.3). Finally, it is important to note that this is a brief high-level description of CPS and that this imaging mode is

much more complex in its implementation [36; 86].

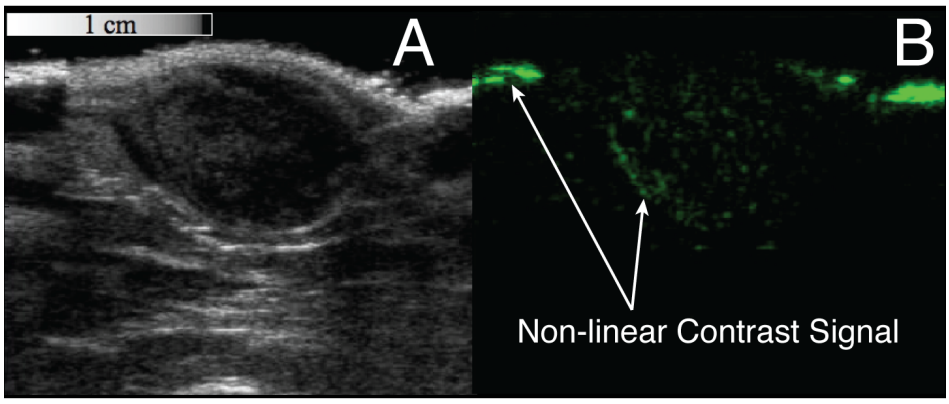

Figure 5.3: Examples of both b-mode and CPS images output from the Siemens Sequoia system. A: The grayscale b-mode image is a typical anatomical interrogation of a subcutaneous fibrosarcoma tumor. B: An interrogation of the same tumor in the same location, but using CPS mode, a non-destructive non-linear imaging technique, which suppresses the signal from the tissue. The green signal is the receive signal from non-linear targeted microbubbles within the tumor tissue.

5.1.4 Harmonic and Sub-Harmonic Imaging Overview

As previously mentioned, microbubbles behave similar to a spring-mass system [36]. Moreover, the oscillatory motion of the microbubble in an acoustic field may contain harmonic and sub-harmonic energies relative to the fundamental transmit frequency, f_0 [82]. By utilizing these properties, it is possible to detect microbubbles through harmonic and sub-harmonic imaging techniques [82; 87; 88].

Harmonic imaging is a method where the ultrasound system separates the second harmonic frequency signal from the fundamental transmit frequency. Briefly, an ultrasound system generates a transmit pulse at a frequency f_0 that is within the bandwidth of the system. The microbubble oscillates and produces harmonic energies, which are subsequently detected by the system at the second harmonic frequency, $2f_0$ [36; 82]. By using filtering techniques, the harmonic signals are separated from the fundamental

frequency, which contains most of the energy detected from tissue. Unfortunately, at high enough pressures, tissue may also generate harmonic signals [36; 82]. Therefore, most of the systems that incorporate this technique are obscured by residual tissue signal components, which cannot be completely separated from the microbubble signal [36; 82]. Since this is not a multi-pulse imaging strategy, frame-rates are typically not compromised when using this technique.

Under certain conditions, microbubble contrast agents also generate sub-harmonic energy [87; 88; 89]. Sub-harmonic imaging is a technique that utilizes this behavior as a means to separate the microbubble signal from the tissue signal. Sub-harmonic imaging is similar to harmonic imaging; however in this detection scheme, the ultrasound system receives the scattered microbubble signal at $\frac{1}{2}f_0$, rather than twice the fundamental frequency [87; 88; 89]. Since the received signal is lower in frequency than the fundamental, this technique does not suffer significantly from frequency-dependent attenuation. Unfortunately, the resolution of the system worsens because of the lower detected sub-harmonic frequencies. Similar to harmonic imaging, frame-rates are typically not affected when using this technique due to its single-pulse strategy.

While harmonic imaging and sub-harmonic imaging have been utilized successfully in various applications, these imaging techniques were not inherent to our clinical ultrasound system, and thus not available as a comparison to CPS. Therefore, all *in vivo* imaging throughout this dissertation was performed using CPS imaging.

5.2 Experimental Methods - Imaging System

5.2.1 System overview and capabilities

A Siemens US imaging system (Acuson Sequoia 512 Mountainview, CA) with a linear array transducer (Model #:15L8) was used to acquire all US images described herein (Figure 5.4). For molecular imaging experiments, b-mode images are required to obtain

regions of interest for quantifying biomarker expression within a tumor. Thus, for all experiments performed, b-mode US images of tumors were taken at 14 MHz in spatial compounding mode. Another necessary component for quantifying biomarker expression in molecular imaging experiments is the destruction of microbubbles. This was achieved using the D Color function (Color Doppler) at 7 MHz with a maximum mechanical index (MI) of 1.9. Prior studies utilizing a MI of 1.9 to destroy microbubbles suggest no indication of bioeffects when higher frequencies ($\geq$7 MHz) are utilized [90].

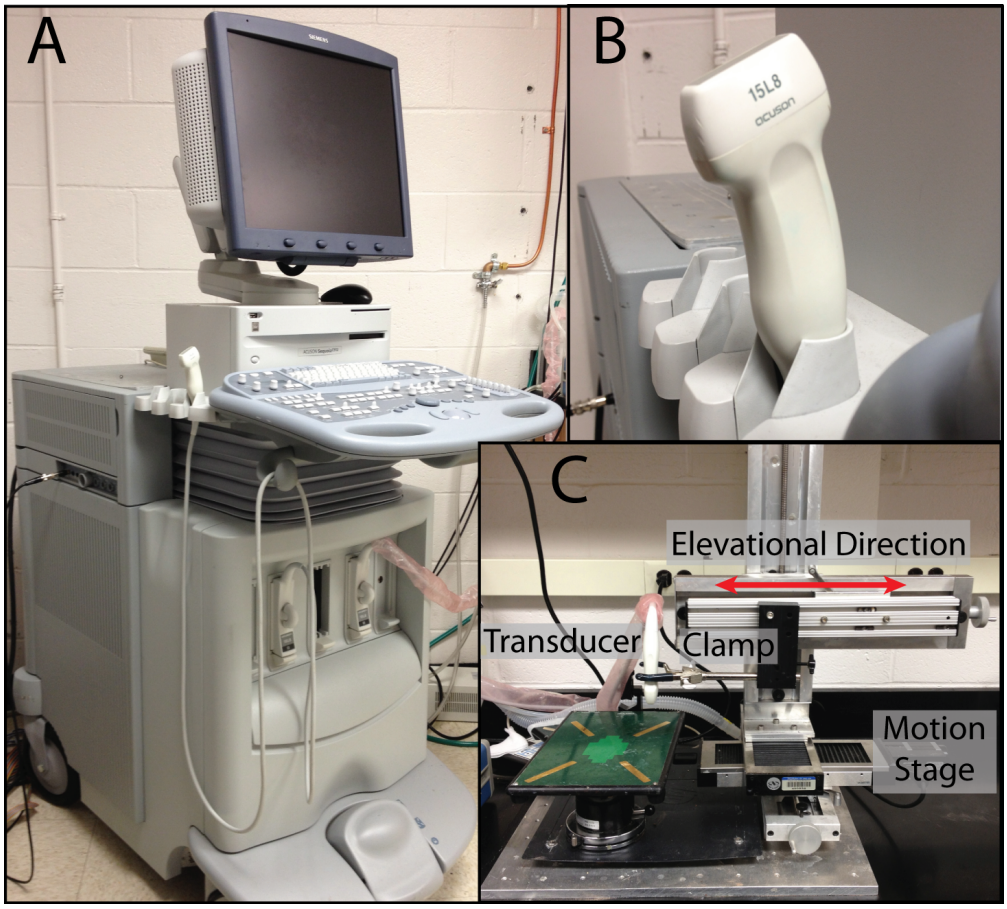

Figure 5.4: Images of the US scanner used for all of the studies described herein. A: Siemens Acuson Sequoia with a 15L8 linear array transducer. B: Close-up of the 15L8 linear array transducer that was used in all US experiments. C: 3-D stage used for all volumetric acquisitions. The transducer was positioned in a fixed clamp and digitally stepped in the elevational direction using the linear motion stage shown in the image.

5.2.2 Experimental Methods - CPS Imaging

MCAs were imaged in CPS mode, which is a non-destructive contrast-specific imaging technique previously described in 5.1.3. CPS was implemented to provide a high contrast to tissue ratio while being minimally destructive to microbubbles [56; 60; 86]. For all contrast imaging, the transducer was operating at a frequency of 7 MHz and a MI of 0.18 with a dynamic range of 80 dB. In a preliminary experiment, the video intensity of targeted agents *in vivo* was observed over 30 seconds using CPS at a MI of 0.18. In this experiment (data not shown), no loss in signal intensity was observed over the evaluated time frame, indicating that our imaging parameters were non-destructive. This conclusion was corroborated by Kaufmann and colleagues in a study performed in 2010 evaluating the effect of power on microbubble adherence in molecular imaging experiments *in vivo* [91].

5.2.3 Experimental Methods - 3-D Imaging Apparatus

To create 3-D data sets, the transducer was positioned in a fixed clamp and digitally stepped in the elevational direction using a linear motion stage (Model UTS150PP, Newport Irvine, CA) (Figure 5.4C). A custom LabView (National Instruments Austin, TX) program was interfaced to both the motion stage and the US system. Using output signals from the US system, the step-size of the motion stage was precisely positioned while simultaneously triggering the capture of video data at every discrete step [81; 92]. The elevational beam width of the 15L8 transducer was calculated to be $\sim$800 μm.

5.2.4 Experimental Methods - ARF for MCA Translation

ARF was utilized in Chapters 10 and 11. ARF pulses were implemented using the pulsed wave (PW) Doppler mode at a frequency of 7 MHz. Adjusting gate size, location of the gate within the field, and blood velocity scale enabled us to achieve a 25%

duty cycle with a pulse repetition frequency (PRF) of 25 kHz. The axial focus was positioned deep into tissue (∼6 cm) to create an unfocused application of ARF. Finally, the amplitude of the ARF pulses was modulated by using the power output dial of the US system.

5.3 Animal Preparation and MCA Administration

In this section, we describe how animals were prepared and contrast agents were administered for the studies in Chapters 7 through 11. All animal studies were conducted in accordance with the protocols approved by the University of North Carolina School of Medicine's Institutional Animal Care and Use Committee.

In Chapters 7 through 11, rats of similar sizes (∼125 g) were used for all *in vivo* studies. The tumor model used in all *in vivo* experiments was a rat fibrosarcoma (FSA) [93]. In previous studies, this particular type of tumor has been shown to provide a good model for $\alpha_v\beta_3$ targeted molecular imaging [38; 81]. It should be noted, however, that an R3230 mammary carcinoma tumor model was also evaluated in Chapter 8.

5.3.1 Tissue Implantation

During the tumor tissue implantation procedure, the rats were anesthetized using 2% inhaled isoflurane mixed with oxygen. The animal's body temperature was maintained at 37° through the use of a temperature-controlled heating pad. Next, the rat's left flank was shaved and disinfected and a 2 mm incision was made above the quadriceps muscle. Finally, a small 1 mm^3 piece of tumor tissue was positioned subcutaneously and allowed to grow for approximately 2 weeks. Once the tumor had grown to approximately 1 cm in diameter in the longest measurable axis, imaging was performed.

5.3.2 Animal Preparation for Imaging

Rodents were anesthetized with 2% inhaled isoflurane mixed with oxygen. Once the rat was sedated, the area to be imaged was shaved with small animal hair clippers and further depilated using a chemical hair remover. A 24-gauge catheter was inserted into the tail vein of the animal for the purpose of administering MCAs. The US transducer used in the *in vivo* analysis was positioned in a fixed clamp and coupled to the animal with US gel. Throughout the imaging procedure, the rodent's body temperature was maintained through the use of a temperature-controlled heating pad .

5.3.3 Contrast Administration

The sizes and concentrations of stock solutions for all microbubble types used in all studies were measured prior to each imaging study using an Accusizer 780A laser light obscuration and scattering device (Particle Sizing Systems, Santa Barbara, CA, USA). For each injection, the appropriate volume of stock solution was added to the catheter via a micropipette tip and flushed with sterile saline. Animals received less than 1.5 mL limit of total fluid volume through the tail vein within any 24-hour period.

Table 5.1 summarizes the animal study parameters for each experimental study described in this dissertation.

Table 5.1: Summary of Animal Study Parameters

Chapter	Animal Type	# Animals	Imaging Subject	Tumor Type	Imaging Type
7	Rat	13	Tumor	FSA	MI
8	Rat	9	Kidney	NA	Perfusion
8	Rat	3	Tumor	FSA, R3230	MI
9	Rat	8	Tumor	FSA	MI
10	Rat	8	Tumor	FSA	MI
11	Rat	8	Tumor	FSA	MI
11	Rat	8	Tumor	FSA	Perfusion
12	Mouse	14	Tumor	Panc.	DCE-PI
12	Mouse	14	Tumor	Panc.	MI

CHAPTER 6

Experimental Diagnostic Methods

This chapter describes the experimental diagnostic procedures utilized in this dissertation. Each section generally describes the method, how the data was obtained from each method and its implementation herein.

6.1 Perfusion-Based Imaging and Methods

Tracking the transit of microbubbles after a bolus injection enables measurements of the physiology of organs or tumors, which can provide diagnostic information regarding disease [94]. The ability to accurately quantify tissue perfusion is essential for the assessment of the physiological functionality and viability of a specific type of tissue [94]. For instance, when evaluating blood perfusion in the normal kidney, the arterial venous transit is less than 4 seconds; however, in acute renal allograft rejection, it is much longer [94; 95]. By using contrast-enhanced ultrasound, we can measure tissue perfusion by monitoring the backscattered intensity from the microbubbles flowing through the tissue of interest and make diagnostic decisions based on this data. Different parameters related to tissue perfusion may be extracted from this sort of contrast-enhanced analysis such as blood velocity, the volume of blood passing in a section of tissue per unit of time, and the proportion of tissue volume occupied by blood [94].

6.1.1 Time-Intensity

In this dissertation, microbubble clearance from the circulatory system was measured *in vivo* by observing the length of time that each type of microbubble persisted in the tumor vasculature (or kidney in Chapter 8) after a bolus injection of MCAs. Briefly, the linear array transducer was placed in a fixed clamp to maintain the same imaging plane and the imaging system was set to a center frequency of 7 MHz in CPS mode. After each bolus injection, the MCA wash-in was recorded at a 1 Hz sample rate using the clip store function on the US system. Once there were no microbubbles visibly moving in the vasculature, the video was stopped and analyzed offline. Figure 6.1 describes the procedure of measuring the intensity of a region of interest over time for the purposes of evaluating microbubble clearance.

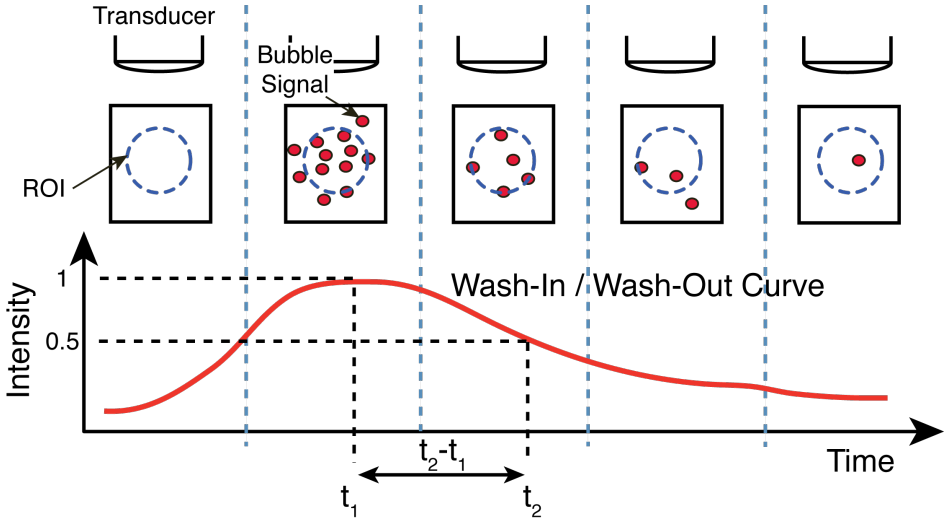

Figure 6.1: Diagram that describes the mechanism for obtaining a time-intensity curve for contrast-enhanced imaging. Persistence is measured as the time from the peak intensity to the time that the video intensity of the ROI reached half of the peak intensity.

Of note, only animal studies with contrast administration not requiring radiation force were used to collect persistence data, because the volumetric administration of

ARF interferes with our ability to observe the contrast agent wash-in. This is directly related to data that was collected in Chapter 11.

Perfusion imaging videos in Digital Imaging and Communications in Medicine (DICOM) format were imported and analyzed using custom graphical user interface (GUI) Matlab software (Mathworks, Natick, MA) (Figure 6.2). Pixel intensity was averaged within the region of interest (ROI) for each video frame and normalized with respect to the movie frame with the highest mean. Within each data set, the system receive gain and transmit power were kept constant. The persistence time of the MCAs was calculated by taking the time from the peak intensity to the time that the video intensity of the ROI reached half of the peak intensity, which is an established metric for this method of evaluation [51].

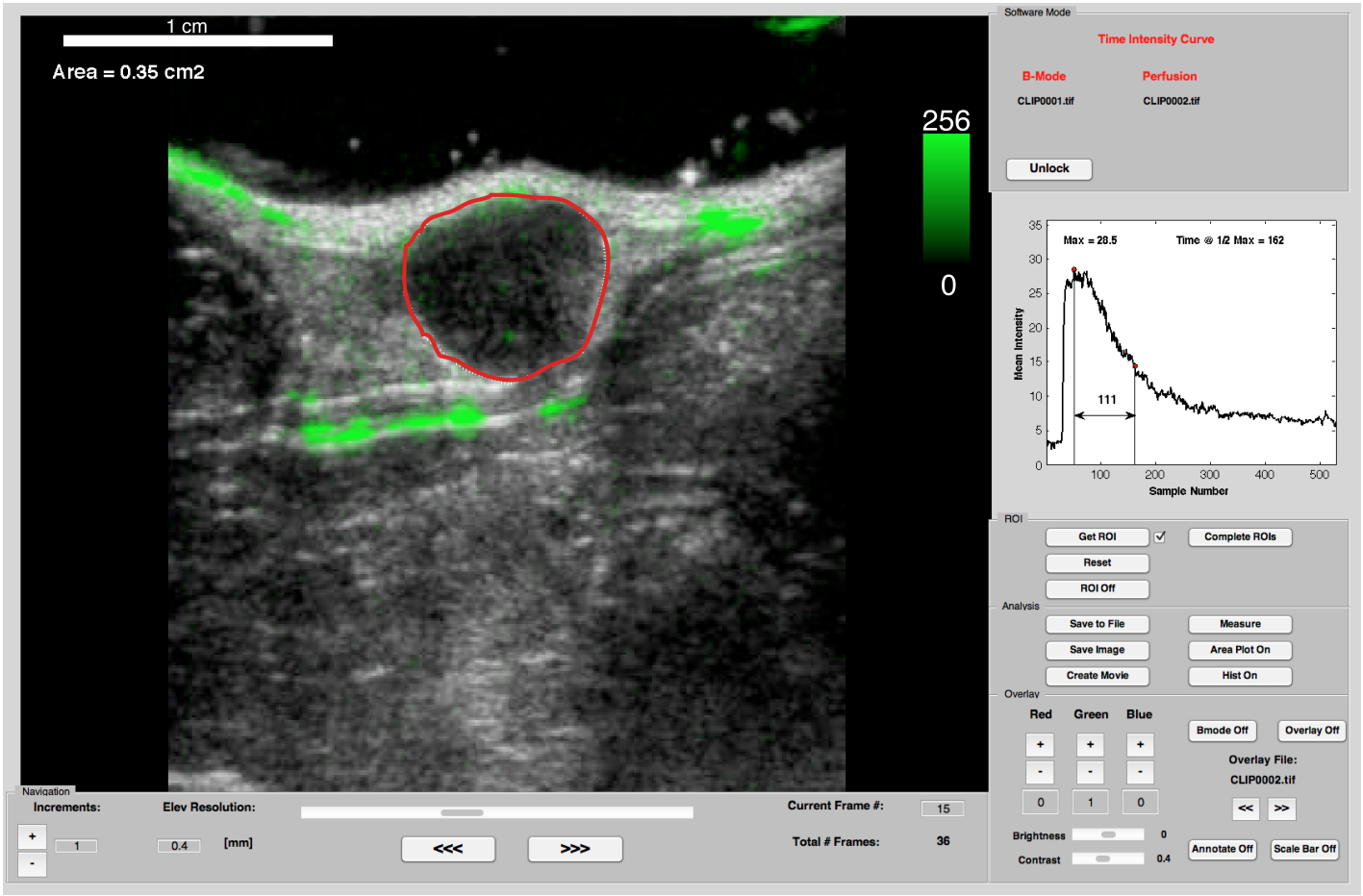

Figure 6.2: Customized GUI that calculates the time-intensity curve for a drawn ROI. The red line corresponds to the user-drawn ROI. The image on the far right is the time-intensity curve associated with microbubble clearance within a fibrosarcoma tumor.

6.1.2 Destruction-Reperfusion

Dynamic contrast-enhanced perfusion imaging (DCE-PI) is an US technique that is used to non-invasively monitor the blood flow in both large vessels and in the capillary microcirculation using non-targeted perfusion-based MCAs. This technique uses a short, high-intensity pulse of US that causes rapid destruction of MCAs in the interrogated region. This clearance pulse is immediately followed by a low-intensity contrast-specific signal that does not fracture the microbubbles, but instead allows for the pixel-by-pixel observation of blood flow rates as the MCAs enter back into the tissue [71; 96]. Accordingly, changes in contrast enhancement over time can provide information about tissue perfusion. Figure 6.3 illustrates the concept of DCE-PI.

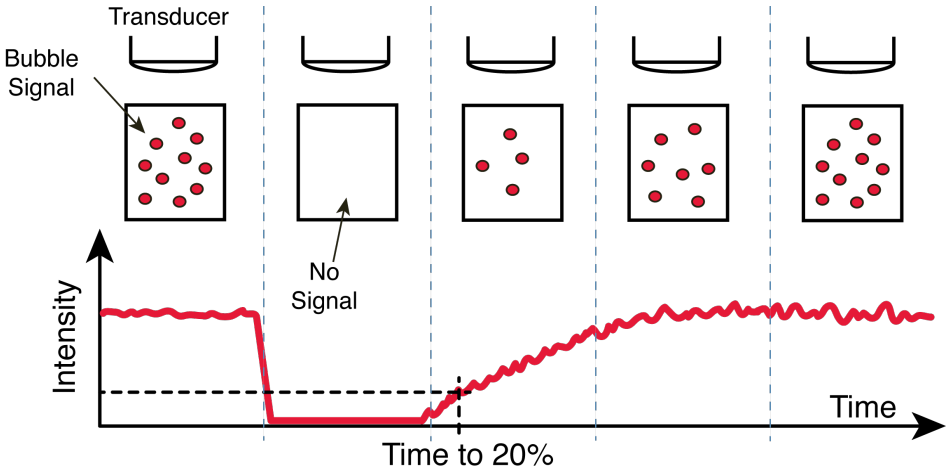

Figure 6.3: Diagram describing the destruction-reperfusion approach to DCE-PI. MCAs are destroyed and subsequently interrogated until the intensity reaches 20% of the maximum.

In this dissertation, DCE-PI was performed by using the destruction-reperfusion imaging technique previously described by Wei *et al.* and real-time motion correction was performed as described by Pollard *et al* [71; 97]. The CPS capture software tool was used to implement this technique. Briefly, non-targeted contrast agents were continuously infused at a rate of 15 $\frac{\mu L}{min}$. After a wait period of one minute for complete

tumor perfusion, a contrast-specific frame was collected and recorded by the system. This was followed by a short, high-intensity pulse of US that causes rapid destruction of MCAs in the 2-D imaging plane was introduced. This clearance pulse was immediately followed by a low-intensity, contrast-specific interrogation to monitor the MCAs as they entered back into the tissue. When the monitored contrast signal reached 20% (Time to 20% - TT20) of the system maximum, the time was recorded and displayed as a color. Perfusion mapping occurred at the pixel level and the maximum perfusion time window was set to be 20 seconds for all readpoints. Within each data set, the system receive gain and transmit power were kept constant.

Video data from perfusion imaging experiments were acquired and saved in DICOM format for offline analysis. Using the b-mode image data collected during the MCA destruction sequence, ROIs were established around the perimeter of the tumor in each image plane. With custom Matlab scripts, the mean pixel intensity, which is linearly related to the time that it takes to reach 20% of the maximum system value, was averaged for all voxels throughout the perfused volume of the treated tumor (Figure 6.4).

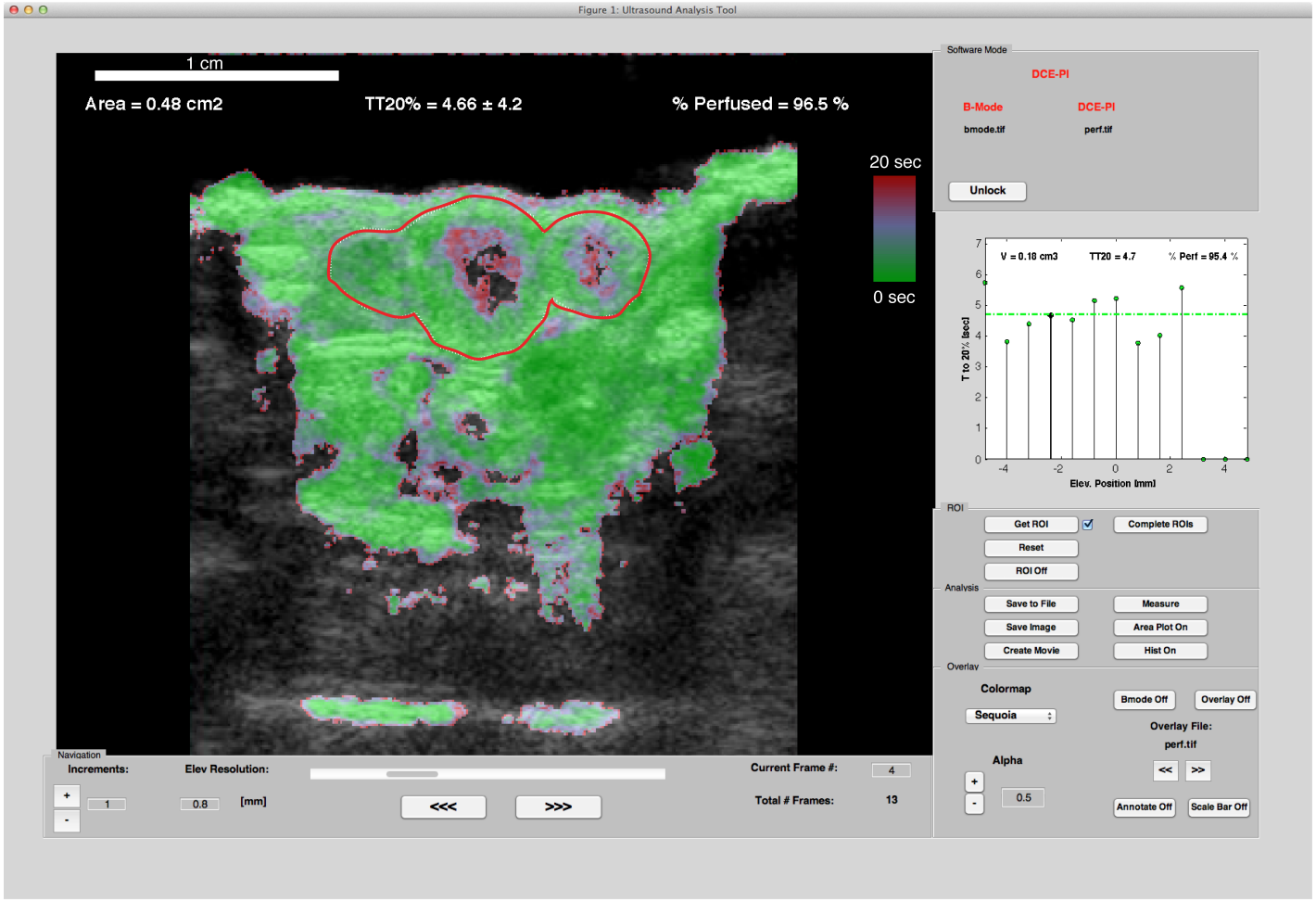

Figure 6.4: Custom GUI that calculates the mean destruction-reperfusion values for a drawn ROI. The red line corresponds to an example user-drawn ROI. The output plot on the right illustrates the slice-by-slice TT20 values associated with this tumor.

6.2 Molecular Imaging and Methods

As previously discussed, USMI has the ability to non-invasively characterize biologic processes at the cellular and molecular level [76; 98; 59]. The principle behind USMI is the selective targeting of acoustically active intravascular MCAs to biomarkers expressed on the endothelium [99] (Figure 6.5). Once accumulated at the target site, the MCAs enhance the acoustic backscatter from pathologic tissue that might otherwise be difficult to distinguish from normal tissues. While USMI is still a developing field, a wide variety of techniques are emerging such as assessment of tumor angiogenesis, the diagnosis of myocarditis, the evaluation of transplant rejection, the evaluation of cardiovascular disease, and the imaging of dysfunctional endothelium, and thrombus [98; 100; 77; 101].

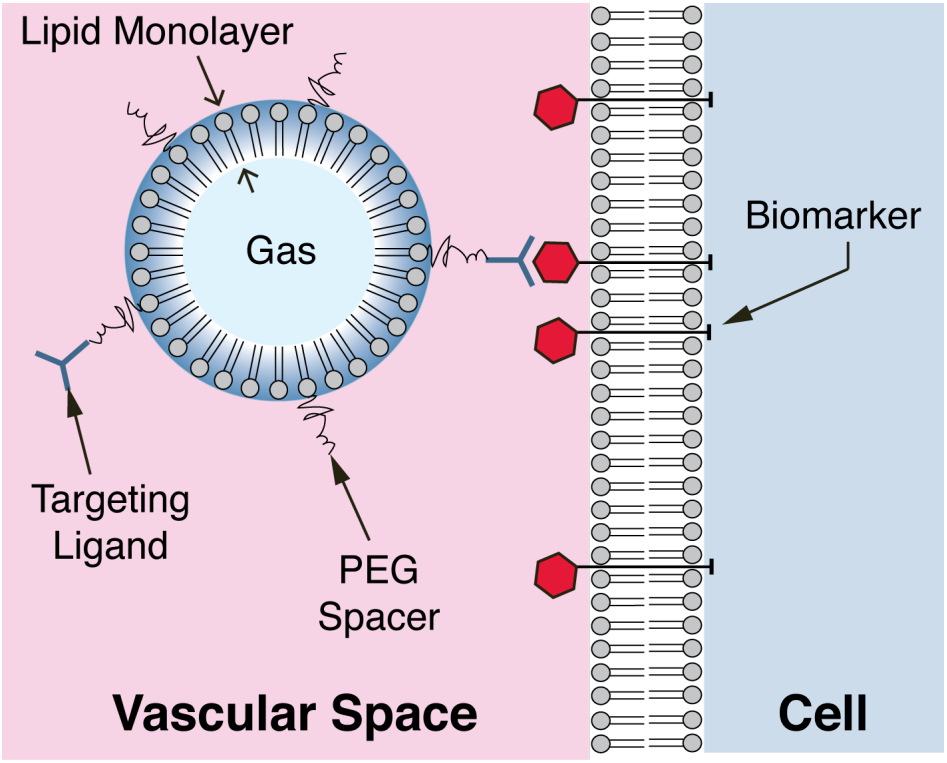

Figure 6.5: Diagram illustrating a targeted MCA. Targeted MCAs adhere to vascular biomarkers, which can be detected with US.

In this dissertation, *in vivo* molecular imaging was performed as follows. CPS mode was used in all molecular imaging studies to image targeted microbubbles. Prior to imaging tumors with targeted contrast agents, background data was taken in both b-mode and CPS mode to optimize elevational scan length and to ensure the absence of bubbles within the coupling gel. After the initial scans were performed, the system was paused and a bolus injection of MCAs was administered through the catheter followed by a sterile saline flush. After waiting for freely-circulating bubbles to clear from the animal's system, a 3-D imaging scan was acquired across the tumor in the US system's CPS mode. The bound microbubbles were then destroyed using a high mechanical index b-mode (MI: 1.9) volumetric scan, and then the tumor was re-imaged in CPS mode at the same elevational slice locations for a baseline measurement with no targeted agents (Figure 6.6). It is important to note that prior studies utilizing a MI of 1.9 to destroy microbubbles suggest no indication of bioeffects when higher frequencies ($\geq$7 MHz) are utilized [90]. Within each imaging data set, the system receive gain and transmit power were kept constant. The specifics involving the USMI procedure vary for each study. Table 6.1 summarizes the imaging parameters for each experimental study described in this dissertation.

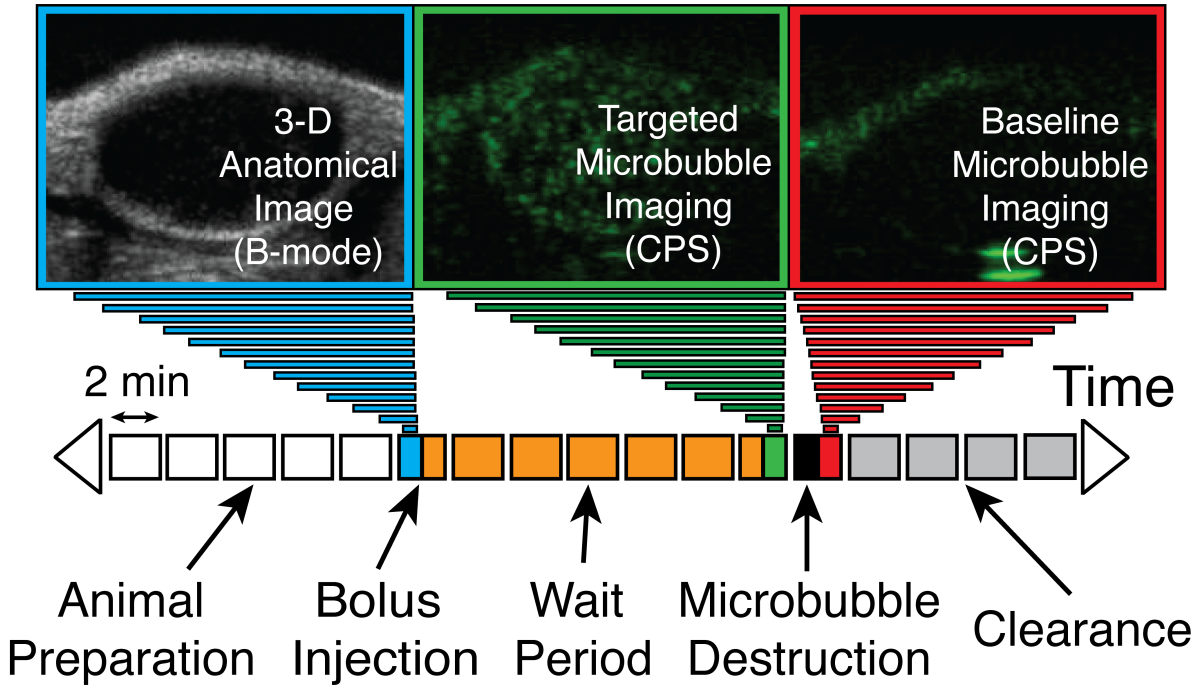

Figure 6.6: Diagram illustrating the general timeline associated with the molecular imaging protocol. Each box along the timeline represents a 2-minute block of time. Typical times associated with animal preparation were on the order of 10 minutes. This was followed by a 3-D anatomical image acquisition in b-mode. Next, there was a wait period, which was typically between 10 and 15 minutes for larger microbubbles. Finally, the targeted data was collected along with the baseline acquisition.

Table 6.1: Summary of Imaging Parameters

Chapter	Imaging Type	CPS MI	Freq. [MHz]	CPS Gain [dB]	Elev. Steps [μm]	ARF Pres. [kPa]
7	MI	0.18	7	-10	400	NA
8	Perfusion	0.18	7	-5	NA	NA
8	MI	0.18	7	-3	1000	NA
9	MI	0.18	7	-3	800	NA
10	MI	0.18	7	-10	400	4, 13 and 21
11	Perfusion	0.18	7	-12	NA	NA
11	MI	0.18	7	-12	400	13
12	DCE-PI	0.18	7	-15	800	NA
12	MI	0.18	7	-15	400	NA

Video data from targeting experiments were acquired and saved in DICOM format for offline analysis. Using b-mode image data collected prior to contrast administration, ROIs were established around the perimeter of the tumor in each image plane. With custom Matlab scripts, the difference in mean pixel intensity between the pre-destruction pulse image (the image with adherent MCAs) and the background image was determined for each image plane as a measure of $\alpha_v\beta_3$ targeting, similar to previous molecular imaging studies with US [38; 81] (Figure 6.7).

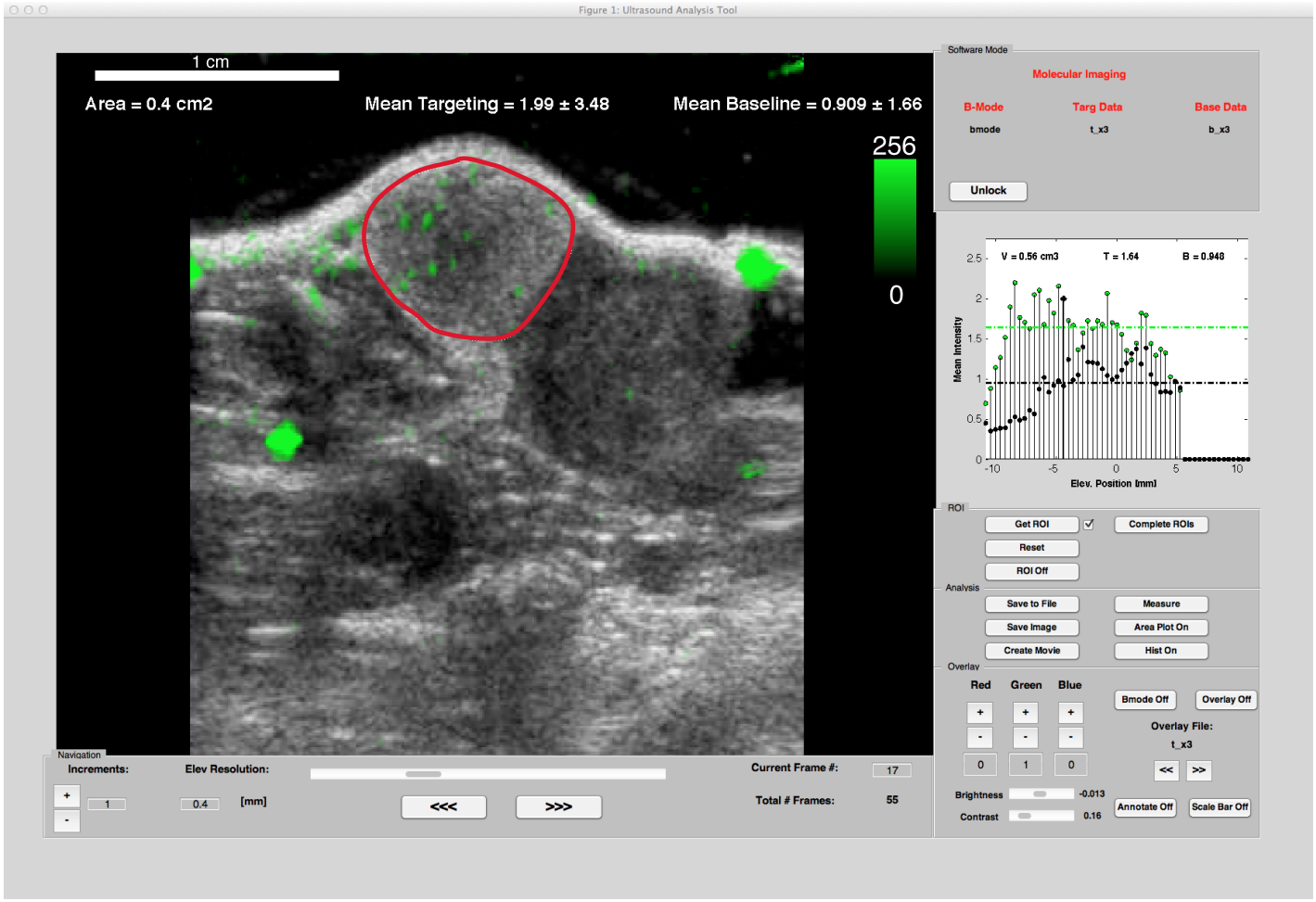

Figure 6.7: Custom GUI that calculates the mean targeted intensity values for a drawn ROI. The red line corresponds to the user-drawn ROI. The figure on the right illustrates the slice-by-slice values of the mean intensity from the targeted microbubble acquisition and the corresponding baseline acquisition.

CHAPTER 7

Repeated Administration of Targeted Contrast Agents

7.1 Introduction

Often, an USMI study requires multiple targeted microbubble injections within a single imaging study to evaluate short-term biological changes, system parameters, or novel microbubble formulations [102; 103; 104]. Targeted microbubbles are fitted with a ligand that allows binding to endothelial biomarkers. However, as endothelial receptors are occupied by ligands from targeted bubbles, it is possible that these receptors would no longer be available for future targeting. This might happen if 1) MCAs stay retained at the target site, or 2) fragments of the MCAs are retained at the target site after bubble destruction. Thus, if targeted microbubbles are injected multiple times in a single animal study, it is possible that the quantity of available binding sites is diminished over time. In the case where receptor ligands were sufficiently competitively inhibited, it would bias the results of successive molecular imaging data where multiple targeted microbubble injections are required.

We hypothesized that the amount of biomarker expression, relative to the amount of receptors occupied by ligands from targeted bubbles, would be great enough to

allow for multiple targeted microbubble injections for a single animal study without discernible competitive inhibition effects. To test this hypothesis, we analyzed the *in vivo* molecular imaging results from two groups of animals. The first group of animals, a control group, received molecular imaging studies with microbubbles targeted to $\alpha_v\beta_3$ at time 0 and 60 minutes. The second group of animals was imaged at the same two time points, but with three additional targeted microbubble injections at time 15, 30, and 45 minutes (Figure 7.1). These time points were chosen to provide sufficient time for microbubbles to clear circulation prior to successive injections. Molecular imaging results were compared between groups at baseline and 60 minutes as an indication of whether or not multiple serial injections have an effect on the outcome of an USMI experiment.

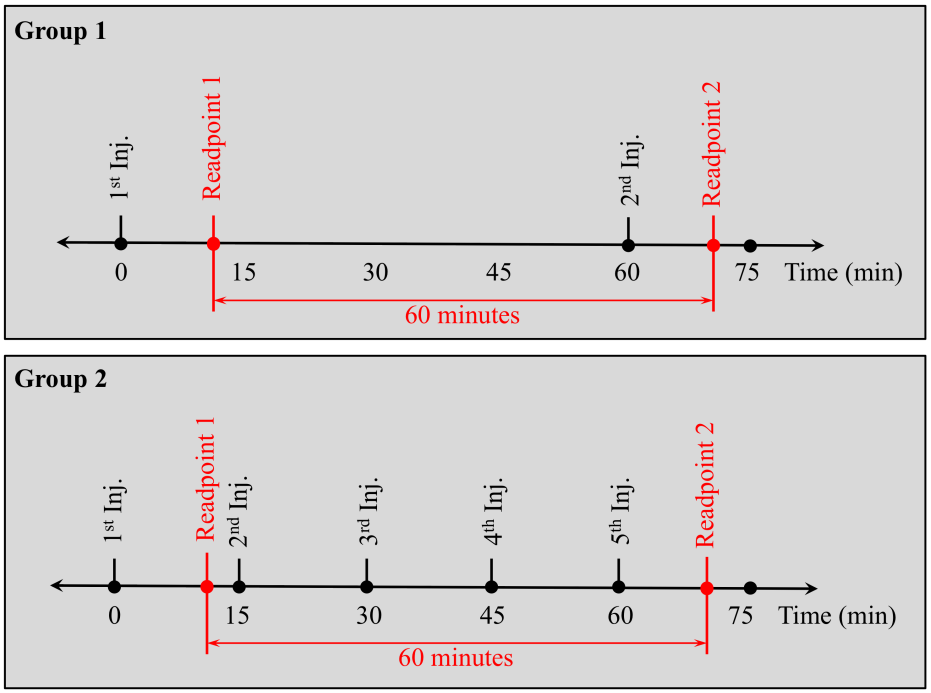

Figure 7.1: The timelines for when bolus injections were given and the imaging readpoints for groups 1 and 2. Each bolus injection, for group 1 and group 2, consisted of a contrast agent dose of 5 x 10^6 microbubbles.

7.2 Materials and Methods

7.2.1 Microbubble Contrast Agents

Lipid solutions for MCAs designed to target $\alpha_v\beta_3$ integrins were created as described in 4.3.3 and 4.3.4. MCAs with a large, preferentially-selected mean diameter (3.3 $\pm$ 1.9 μm) have been shown to produce greater backscatter intensities [38; 105; 42] in USMI studies as compared to vial-shaken, unsorted, polydisperse distributions. Therefore, all MCAs in this study were sorted as described in 4.3.6.

7.2.2 Animals and Tumor Models

A total of 13 Fischer 344 rats (Charles River Laboratories, Durham, NC, USA) of similar sizes were used for all *in vivo* studies (Group 1 - N = 7, Group 2 - N = 6). Tumors were implanted and animals were prepared for imaging as described in 5.3. For each contrast agent injection, the appropriate volume of stock solution was added to the catheter via a micropipette tip and flushed with 100 μL of sterile saline such that a dose of 5 x 10^6 microbubbles was administered consistently with each injection.

7.2.3 Clinical Imaging System

The 3-D US imaging system along with the parameters used to acquire all images in this chapter are as described in 5.2.1, 5.2.2 and 5.2.3. Within all imaging data sets, the CPS gain (-10 dB) and transmit power (MI: 0.18) were kept constant, and the transducer was stepped elevationally every 400 μm.

7.2.4 Molecular Imaging Protocol

Molecular imaging data was obtained after freely circulating microbubbles had visibly cleared the animal's system (typically 10 minutes). Once the microbubbles had cleared, the molecular imaging procedure and analysis was followed as described in 6.2. We used

Matlab's two-sided Student's t-test to assess the statistical significance of each group. Significance between two different distributions were considered at a value of $p < 0.05$.

7.3 Results

Two different groups of animals were imaged with USMI to determine if multiple serial injections affect the amount of adherent microbubbles detected in an individual experiment. Intensity values for each animal's readpoint were normalized to the value at the baseline measurement or time 0. Injections and molecular imaging readpoints were performed on the control group (Group 1) at time 0 and 60 minutes after the first injection while Group 2's injections were at times 0, 15, 30, 45 and 60 minutes with readpoints at 0 and 60 minutes.

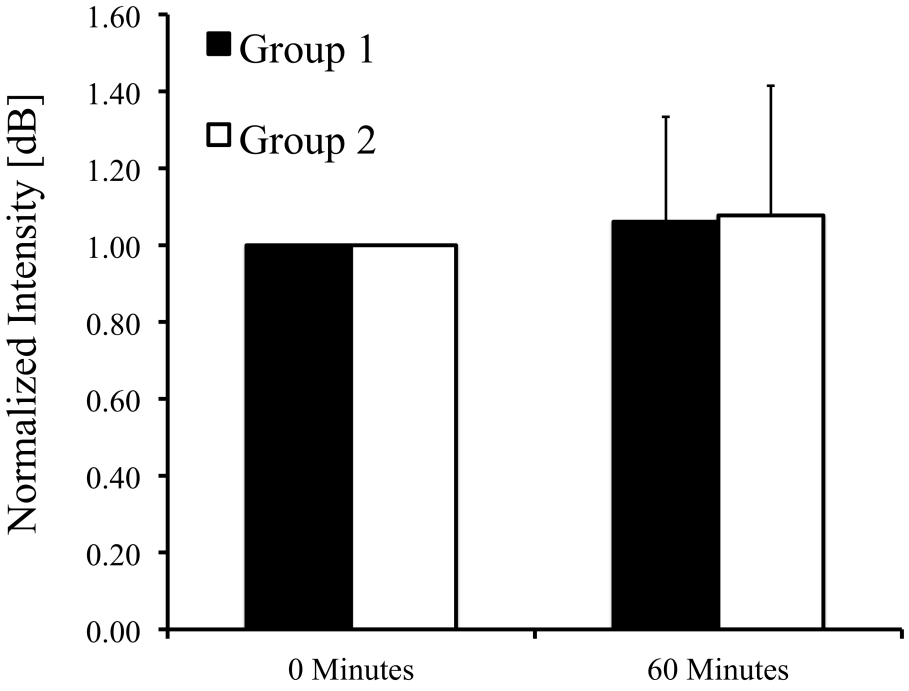

Figure 7.2: The percent change in volumetric targeted microbubble intensity for Groups 1 and 2, 60 minutes after baseline imaging. $p = 0.93$ for Group 1 relative to Group 2.

Group 1 showed a 6% increase (1.06 ± 0.27) in targeting relative to baseline while

Group 2 showed an 8% increase (1.08 ± 0.34) in the amount of targeted microbubbles determined through intensity measurements (Figure 7.2). Group 1 was not significantly different from Group 2 after the 60-minute readpoint (p = 0.93), but rather had similar targeting and similar variance. Figure 7.3 shows a 2 by 2 panel of a representative Group 1 tumor and a representative Group 2 tumor at baseline and 60 minutes after. The green color represents the targeted microbubble signal detected via Cadence Pulse Sequencing mode in the experiment. The green pixels, correlated to the degree of $\alpha_v\beta_3$ expression, are overlaid onto a traditional b-mode image to illustrate the location of the targeting relative to the tumor.

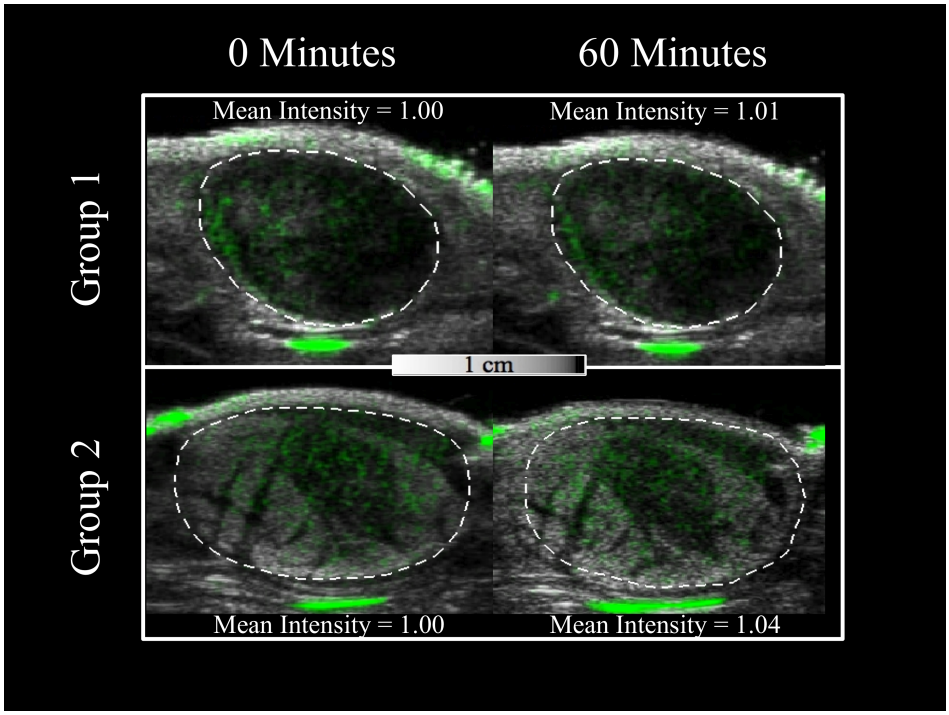

Figure 7.3: 2-D US images of a representative Group 1 and Group 2 tumor at baseline and 60 minutes after initial imaging. The green color is the targeted microbubble signal detected via CPS mode. The intensity of the green color is loosely correlated to the degree of $\alpha_v\beta_3$ expression. The green signal is overlaid onto a traditional b-mode image to illustrate the location of the targeting relative to the tumor. The white dotted line illustrates the ROI selected for the quantification of biomarker expression.

7.4 Discussion and Conclusion

In this study, we evaluated if successive injections of targeted microbubbles would reduce the ability of future injections of targeted bubbles to adhere to endothelial receptor ligands. While the scope of this study was limited to a short time period as well as a specific tumor model and a specific microbubble dose, the results are encouraging. Given the dose of cRGD-targeted microbubbles injected (which was appropriate for achieving sufficient molecular imaging signal) and the inherent variability of the molecular imaging procedure, there was no discernible statistical difference between injecting twice and injecting five times. Ultimately, this suggests that the quantity of over-expressed $\alpha_{\mathrm{v}}\beta_3$ biomarkers present must be sufficiently greater than the available ligands so as not to present competitive inhibition. Thus, preliminary data suggests that serial multiple injections in a single USMI study do not bias or compromise endothelial retention of targeted microbubbles due to competitive inhibition from prior bound bubbles or bubble fragments. What our study does not address is whether or not the adhesion of targeted bubble ligands affects the tumor biology as might be anticipated with large doses. Furthermore, we observed a slight increase in molecular targeting in both imaging models, the mechanism for which is still unknown. Future studies beyond this pilot should include larger animal numbers, different doses of contrast, different ligands, and longer time points.

CHAPTER 8

Improving Sensitivity in Ultrasonic Molecular Imaging

8.1 Introduction

For traditional USMI applications, backscatter intensity is relatively weak owing to the small populations retained during targeting [56; 106; 107; 108; 109; 45]. This poor binding efficiency necessitates signal amplification in USMI applications, thus providing the motivation to maximize the sensitivity to bound MCAs [56; 76; 51].

Owing to the small percentage of bound MCAs at their target sites, research in USMI has focused mainly on improvement of the contrast sensitivity through improved ligands and adhesion schemes, detection methods, and contrast delivery mechanisms [99; 110; 56; 51; 106; 48; 111; 112; 113; 114]. However, over the last several years, more attempts have been made to improve contrast sensitivity by optimizing the echogenicity of the contrast agents themselves.

In order to produce the most effective acoustic backscatter, the scattering cross-section of the microbubble must be as large as possible. In accordance with the Rayleigh scattering model, theory predicts an increase in US backscatter intensity as a function of the microbubble scattering cross-section and therefore size:

$$I = \frac{I_o \sigma}{4\pi z^2} \tag{8.1}$$

where I_o is incident intensity, σ is the microbubble scattering cross-sectional area with a 6^{th} order dependence on radius, and z is the distance between the transducer and the microbubble [36].

Like a mechanical system, the microbubble's competing balance of forces can result in a resonant frequency as it oscillates in an sinusoidal acoustic field. Thus, at the resonant frequency, the microbubble has its largest cross-sectional area and produces the most effective backscatter intensity. Based on the knowledge that microbubble size and resonant frequency are intricately coupled, Talu and colleagues proposed that increasing the monodispersity of a microbubble population to match the fixed frequency output of an imaging system may improve contrast imaging sensitivity [106]. Moreover, in an *in vitro* study of the acoustic response of monodisperse contrast agents, Kaya and colleagues determined that signal amplitude could be increased both by matching the imaging frequency to the bubbles' resonant frequency and by increasing the diameter of the microbubbles [105]. Finally, Sirsi and colleagues recently demonstrated improvements in contrast to tissue ratio in the mouse kidney using high-frequency contrast imaging by increasing the mean diameter of the microbubble population [42]. Because of the significance of microbubble size in the acoustic response, recent interest has involved new production and sorting methods for MCAs, including centrifugation techniques, microfluidics, and electrohydrodynamic atomization [39; 41; 40; 115; 116; 117].

In addition to echogenicity, the bloodstream persistence of a microbubble is directly correlated to the initial radius of a MCA by the dissolution behavior governing lipid-shelled microbubbles. Also, accumulation of targeted MCAs in USMI experiments is generally affected by circulation persistence [118; 119]. It should be noted, however, that bloodstream persistence is a complex physiologic phenomenon that depends on

other environmental factors that are not discussed in this article.

The contrast agent currently approved by the Food and Drug Administration (FDA), Definity®, has a polydisperse distribution with a mean diameter of around 1 μm (diameter 1.0 $\pm$ 0.83 μm, as tested in this study) and a concentration of $\sim$1 x $10^{10} \frac{\#}{\text{mL}}$ [120]. This distribution is characteristic of many types of lipid-shelled microbubbles, which are formed by sonic or mechanical agitation, two common formulation techniques for targeted and non-targeted MCAs. For standard perfusion imaging, MCA size distribution has not been a limitation, because billions of microbubbles are typically administered intravascularly, thus providing plenty of image contrast. However, for USMI applications, relatively small populations of adherent MCAs remain, and thus, provide weak backscatter intensity, which ultimately limits imaging sensitivity [56; 106; 108]. In this chapter, we demonstrate *in vivo* that contrast sensitivity improvement in USMI and perfusion imaging applications can be achieved by increasing the mean diameter in microbubble populations.

8.2 Materials & Methods

8.2.1 Microbubble Contrast Agents

Various MCA size distributions were obtained and characterized for both molecular imaging and perfusion imaging experiments. The method used to create the characteristic size distributions is described in section 4.3. For the set of experiments in this chapter, we chose to examine sorted distributions with mean diameters of 1.1 $\pm$ 0.43 μm and 3.3 $\pm$ 1.95 μm (see Figure 8.1), which were isolated using the described centrifugation process (4.3.6). In addition, an unsorted polydisperse size distribution (diameter: 0.9 $\pm$ 0.45 μm), similar to the FDA-approved contrast agent Definity® (diameter: 1.0 $\pm$ 0.83 μm), was used for molecular imaging and perfusion-based imaging experiments (see Figure 8.1). Concentrations and size distributions of the MCAs were

obtained using a laser light obscuration and scattering device.

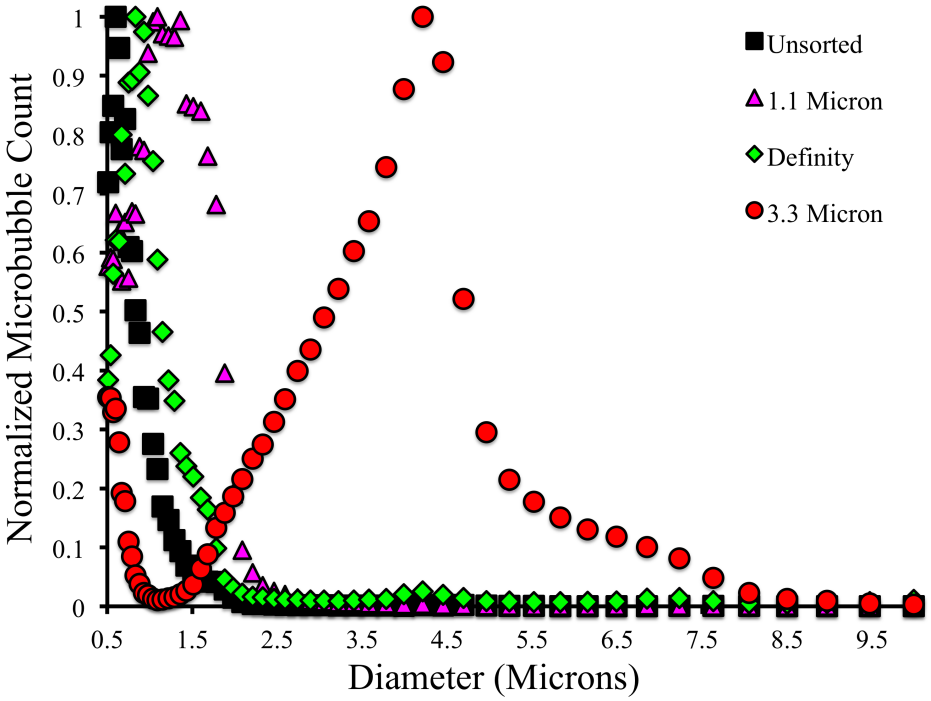

Figure 8.1: Example MCA size distributions obtained during centrifugal size sorting. Values were normalized to the maximum count for comparison.

Perfusion-based and non-targeted lipid solutions for size-selected microbubbles were created as described in 4.3.1, 4.3.4 and 4.3.6. Similarly, unsorted perfusion-based and non-targeted lipid solutions were created as described in 4.3.1, 4.3.4 and 4.3.5. Sorted MCAs targeted to $\alpha_v\beta_3$ integrins were created as described in 4.3.3, 4.3.4 and 4.3.6. Finally, unsorted MCAs targeted to $\alpha_v\beta_3$ integrins were created as described in 4.3.3, 4.3.4 and 4.3.5.

8.2.2 Animal Preparation and Contrast Administration

Sprague-Dawley rats were used for perfusion imaging, whereas molecular imaging was performed on both FSA and R3230 mammary carcinoma tumor models in Fischer 344 rats. Tumors were implanted and animals were prepared for imaging as described in 5.3.

In all experiments, bolus injections of 150 μL were delivered followed by an immediate flush of at least 100 μL sterile saline to clear any remaining MCAs from the catheter.

8.2.3 Imaging System

For each study, the transducer was positioned in a fixed clamp to maintain the same imaging plane in each microbubble size experiment. The 3-D US imaging system along with the parameters used to acquire all imaging data in this chapter are as described in 5.2.1, 5.2.2 and 5.2.3. Within all perfusion imaging data sets, the CPS gain (-5 dB) and transmit power (MI: 0.18) were kept constant. Within all molecular imaging data sets, the CPS gain was set to -3 dB and the transmit power was maintained at a MI of 0.18, a non-destructive acoustic pressure for microbubble imaging.

8.2.4 Perfusion Imaging

Both male and female albino Sprague-Dawley rats (N = 9) were used for non-targeted US perfusion imaging studies in the rat kidney. The aforementioned MCA size distributions were administered in the perfusion experiments (sorted 1 μm, sorted 3 μm, and unsorted polydisperse distributions). Each MCA size distribution was matched in terms of concentration and administered with bolus injections. MCA size distributions and concentrations were measured before and after administration by sampling the MCA storage container to ensure constancy over time for each subsequent animal injection. Injected dose concentrations ranged between 3 x $10^7 \frac{\#}{\text{mL}}$ and 6 x $10^8 \frac{\#}{\text{mL}}$. The entire rat kidney was chosen as the ROI except in the cases where shadowing occurred (attenuation), specifically the sorted 3 μm distributions at high concentrations (150 μL at $\sim$ 6 x $10^8 \frac{\#}{\text{mL}}$). In these cases, only regions above the shaded area were included in the analysis; however, the same ROIs were compared for each individual distribution at the given concentration. Time-intensity curves from perfusion experiments were acquired using the Siemens Sequoia imaging system and analyzed as described in 6.1.1. We used

Matlab's two-sided Student's t-test to assess the statistical significance between each group. Significance between two different distributions were considered at a value of $p < 0.05$.

8.2.5 Molecular Imaging

The relationship between MCA size and targeted agent sensitivity was assessed in three different rats and 22 different independent imaging planes. The transducer was mechanically adjusted across the tumor with a stage micrometer in 1 mm steps to acquire independent image planes with the use of fewer animals (independent planes were ensured as the -6 dB elevational beam width of the 15L8 in CPS mode is approximately 0.8 mm). Using control and $\alpha_v\beta_3$-targeted MCA populations at a dose concentration of 9 x $10^8 \frac{\#}{\text{mL}}$ (150 μL bolus), the contrast sensitivity of unsorted and sorted 3 μm distributions was evaluated in each imaging plane.

The procedure for performing molecular imaging experiments and the subsequent analysis is described in 6.2. In this study, the time required for the MCAs to clear was qualitatively determined to be on the order of 8 minutes for small size distributions and $\sim$30 minutes for large distributions. We used Matlab's two-sided Student's t-test to assess the statistical significance of each group. Significance between two different distributions were considered at a value of $p < 0.05$.

8.3 Results

8.3.1 Perfusion Imaging (Intensity & Persistence)

Non-targeted perfusion imaging showed a strong correlation between backscatter intensity and the size and concentration of the MCAs administered. Example images at the peak intensities for three different diameter distributions at two different concentrations are presented (Figure 8.2). At low concentrations (150 μL at $\sim$3 x $10^7 \frac{\#}{\text{mL}}$), contrast

circulation in the kidney from the sorted 1 μm and unsorted populations was barely visible at the tested gain setting (-5 dB), in contrast to the sorted 3 μm distribution. The normalized video intensity of sorted 3 μm MCAs was approximately 15 and 8 times larger than mean video intensities of the sorted 1 μm (0.77 ± 0.02 vs. 0.05 ± 0.01; $p<0.05$) and unsorted (0.77 ± 0.02 vs. 0.09 ± 0.01; $p < 0.05$) populations, respectively.

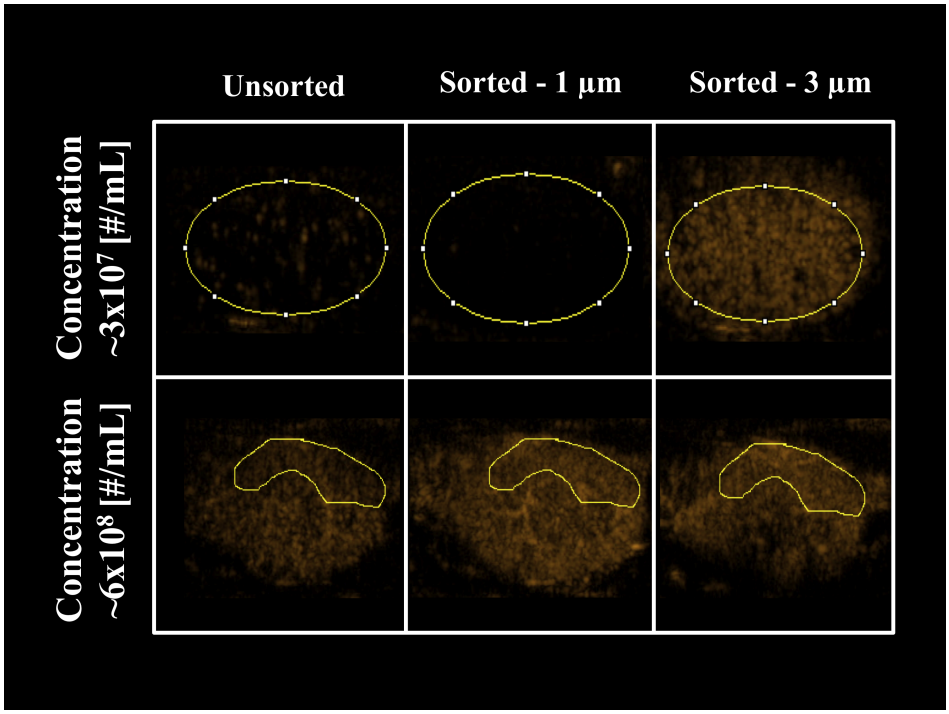

Figure 8.2: Example cadence pulse sequencing images of non-targeted kidney perfusion data for sorted and unsorted microbubble distributions. Regions of interest are indicated and constant for each concentration set. All images were taken at the peak mean intensity.

At MCA concentrations greater than 2 x $10^8 \frac{\#}{\text{mL}}$ (dose: 150 μL), mean video intensity produced by the various size distribution was not significantly different (sorted 3 μm: 0.94 ± 0.0005; sorted 1 μm: 0.80 ± 0.18; unsorted: 0.73 ± 0.30). In each case, the contrast agent circulation in the kidney could be readily visualized. This similarity in video intensity for different distributions at the higher concentration can likely be attributed to the video intensity saturation effect at the higher concentration. Hence,

there was no apparent difference in contrast enhancement as a function of MCA distribution with a high enough concentration and sufficient system receive gain. The ability of the sorted 3 μm MCA size distributions to clearly enhance the kidney microvasculature with approximately 20 times less dose than the sorted 1 μm and unsorted size distributions can be seen in Figure 8.3.

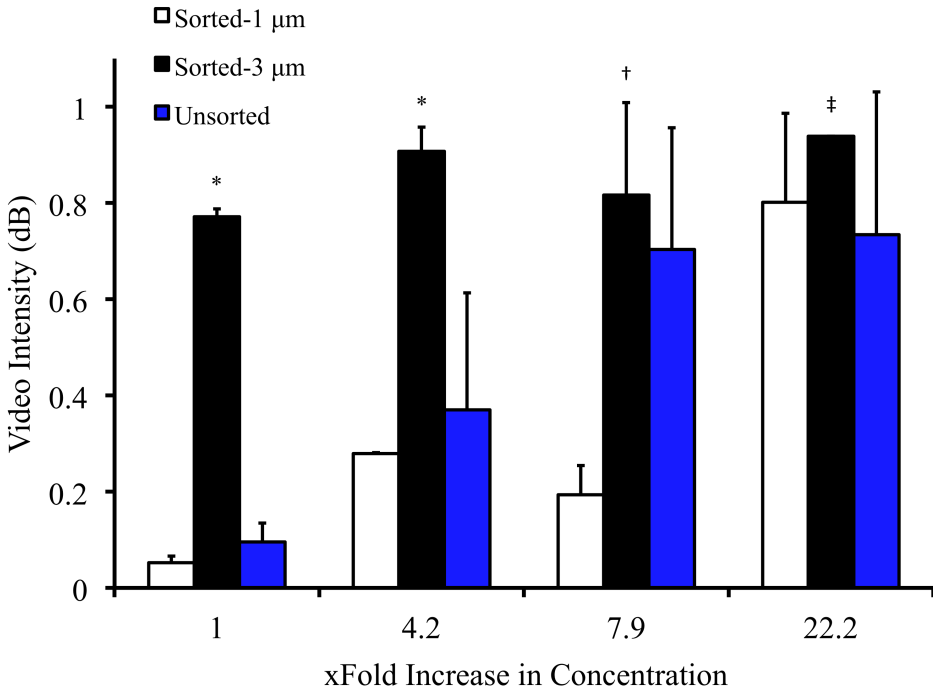

Figure 8.3: Mean normalized peak video intensity as a function of concentration for non-targeted size-sorted perfusion studies. Mean peak values of intensity per region of intensity were normalized across concentration data sets to the maximum average peak intensity. Concentration values are a factor of baseline concentration (150 μL at 3 x $10^7 \frac{\#}{\text{mL}}$). *p < 0.05 compared to sorted 1 μm and unsorted MCAs. †p < 0.05 compared to sorted 1 μm and p < 0.07 compared to unsorted MCAs. ‡p < 0.25 compared to sorted 1 μm and unsorted MCAs.

Persistence curves for the three different distributions (sorted 1 μm, sorted 3 μm, and unsorted) at two different concentrations (150 μL at 3 x $10^7 \frac{\#}{\text{mL}}$ and 6 x $10^8 \frac{\#}{\text{mL}}$) are presented in Figure 8.4. These data show a direct relationship between MCA size and *in vivo* persistence. Microbubble circulation times increase significantly with size

(Figure 8.5), which is expected given the relationship of bubble dissolution to MCA diameter [42; 118; 119]. The sorted 3 μm size distribution provides persistence times that are approximately 3 times (178 $\pm$ 9.9 seconds vs. 52 $\pm$ 0.7 seconds: $p < 0.05$, concentration: 3 x $10^7 \frac{\#}{mL}$, dose: 150 μL) and approximately 9 times (455 $\pm$ 114 seconds vs. 52 $\pm$ 7.8 seconds: $p < 0.05$, concentration: 6 x $10^8 \frac{\#}{mL}$, dose: 150 μL) greater than the persistence times of sorted 1 μm MCAs at the same concentrations. When comparing the sorted 3 μm distributions to unsorted polydisperse distributions, the persistence is approximately 3 times (178 $\pm$ 9.9 seconds vs. 55 $\pm$ 16 seconds: $p < 0.05$, concentration: 3 x $10^7 \frac{\#}{mL}$, dose: 150 μL) and approximately 7 times (455 $\pm$ 114 seconds vs. 65 $\pm$ 23 seconds: $p < 0.05$, concentration: 6 x $10^8 \frac{\#}{mL}$, dose: 150 μL) longer at low and high concentrations, respectively, which suggests a significant increase in circulation time for perfusion applications using larger MCAs.

8.3.2 Molecular Imaging

USMI studies showed a strong relationship between MCA size and targeted contrast sensitivity in both tumor models. Analysis of USMI results includes data from both FSA and R3230 tumor models combined because imaging data collected from each tumor model showed similar video intensity enhancement (Table 8.1) with respect to control populations.

Typical targeted CPS images overlaid onto the b-mode image of the rat tumor illustrate the relatively high acoustic contrast associated with sorted 3 μm MCAs compared to unsorted polydisperse distributions (Figure 8.6). At a CPS gain of -3 dB, video intensity provided from retention of targeted contrast agents in the tumor tissue was 17 times greater from the sorted 3 μm MCA distributions than from control (non-targeted) 3 μm populations (1.0 $\pm$ 0.35 vs. 0.06 $\pm$ 0.06; $p < 0.05$) (Figure 8.7). The unsorted targeted MCAs also produced statistically significant contrast sensitivity

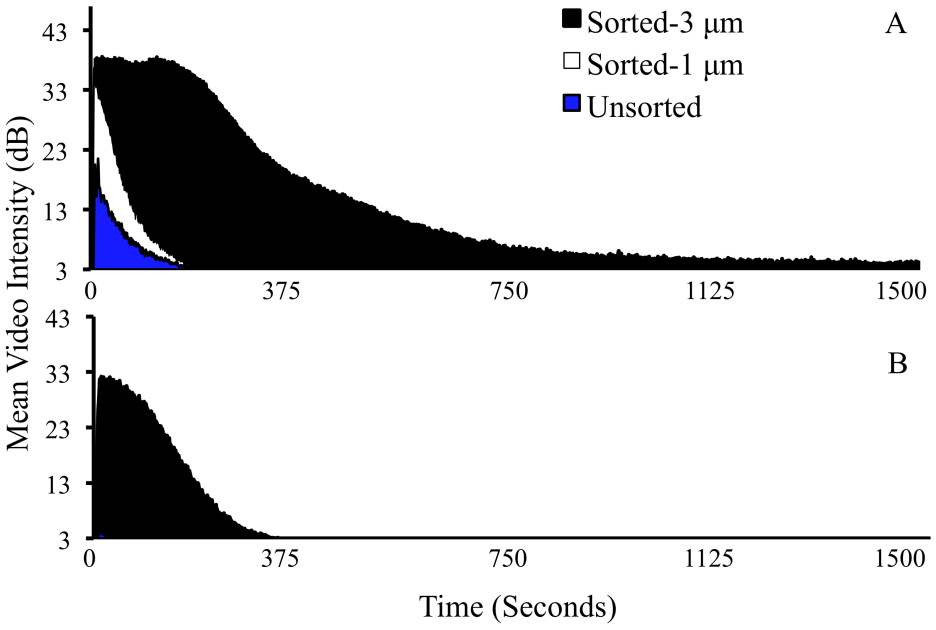

Figure 8.4: Example persistence curves for non-targeted size-sorted and unsorted microbubble distributions. A, Example persistence curves at a concentration of 3 x $10^7 \frac{\#}{\text{mL}}$ (dose: 150 μL). B, Example persistence curves at a concentration of 6 x $10^8 \frac{\#}{\text{mL}}$ (dose: 150 μL).

improvement compared to unsorted control agents (0.05 $\pm$ 0.1 vs. 0.01 $\pm$ 0.02; $p < 0.05$). Although the molecular imaging enhancement produced by both unsorted and sorted 3 μm targeted MCAs was statistically significant compared to that produced by non-targeted control agents, the contrast enhancement provided by the sorted 3 μm MCAs yielded a substantial improvement (20-fold greater) over the enhancement provided by the unsorted population (1.0 $\pm$ 0.35 vs. 0.05 $\pm$ 0.1; $p < 0.05$).

8.4 Discussion and Conclusion

Previous studies have demonstrated that small quantities of MCAs may be retained at the target site [106; 107; 108; 45]. Without optimal sensitivity to all adherent targeted contrast agents, sensitivity in USMI is compromised. Prior *in vitro* studies

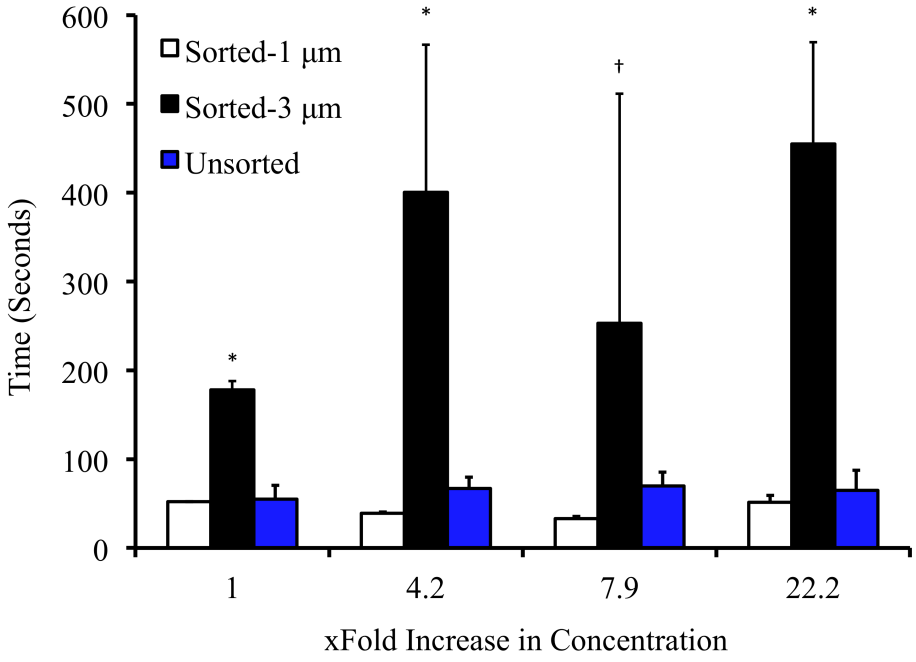

Figure 8.5: Mean persistence times as a function of concentration for non-targeted size-sorted and unsorted perfusion studies. Persistence times were taken to be time from the peak intensity to the time that the intensity reached half of the peak intensity. *p < 0.05 compared to sorted 1 μm and unsorted MCAs. †p $= 0.1$ compared to sorted 1 μm and unsorted MCAs.

have indicated that optimizing size of the microbubbles may result in increased contrast sensitivity [106; 105]. Data presented here confirm that increased contrast sensitivity translates to the *in vivo* environment and that larger MCAs can increase signal in molecular imaging applications.

Our perfusion imaging studies demonstrated that at low concentrations (150 μL at 3 x $10^7 \frac{\#}{\text{mL}}$) and a -5 dB gain on the imaging system, sorted 3 μm MCAs produced well-defined enhancement of the kidney microvasculature. At the same low concentration, sorted 1 μm and unsorted MCAs offered no substantial contrast enhancement.

With the same system gain, and a concentration over a magnitude higher (6 x $10^8 \frac{\#}{\text{mL}}$, dose: 150 μL), the mean peak video intensity for all MCA distributions was

Table 8.1: Normalized Mean Targeted Video Intensity Comparison between FSA and R3230 Tumor Models for Sorted 3 μm and Unsorted Populations (Targeted and Non-targeted).

	Normalized Mean Targeted Video Intensity	
	FSA Tumor Model	R3230 Tumor Model
Sorted 3 μm Targeted	0.95 $\pm$ 0.31	1.11 $\pm$ 0.08
Sorted 3 μm Non-Targeted	0.03 $\pm$ 0.03	0.11 $\pm$ 0.08
Unsorted Targeted	0.07 $\pm$ 0.13	0.01 $\pm$ 0.02
Unsorted Non-Targeted	0.01 $\pm$ 0.02	0.00 $\pm$ 0.01

similar and not statistically different, indicating that there was no advantage to the larger contrast agents at the higher concentration when a moderate (-5 dB) system receive gain is used. This was likely due to saturation of the video intensity for both MCA populations; consequently, we cannot accurately evaluate results at the higher concentrations. It is likely that many researchers currently perform contrast imaging at these higher concentrations; hence, there may be little benefit of size-optimized bubbles if sufficient contrast agent dose and system gain can be used. However, the focus of this study was to demonstrate the advantages of size optimization at low MCA concentrations, such as those present in USMI.

Circulation persistence results indicated that sorted 3 μm MCAs produce at least 3 times greater circulation times than sorted 1 μm and unsorted MCA distributions at all tested concentrations, which is relevant in both clinical and targeted applications. These results are in agreement with data presented by Sirsi and colleagues, who illustrated that persistence time increased with microbubble size in a mouse model, as measured using high-frequency b-mode imaging [121]. In clinical practice, an increase in bloodstream persistence increases the time for diagnosis and maintains a longer time period during which the relative bubble concentration remains constant, which may be important for quantitative techniques. Perhaps the most important conclusion from

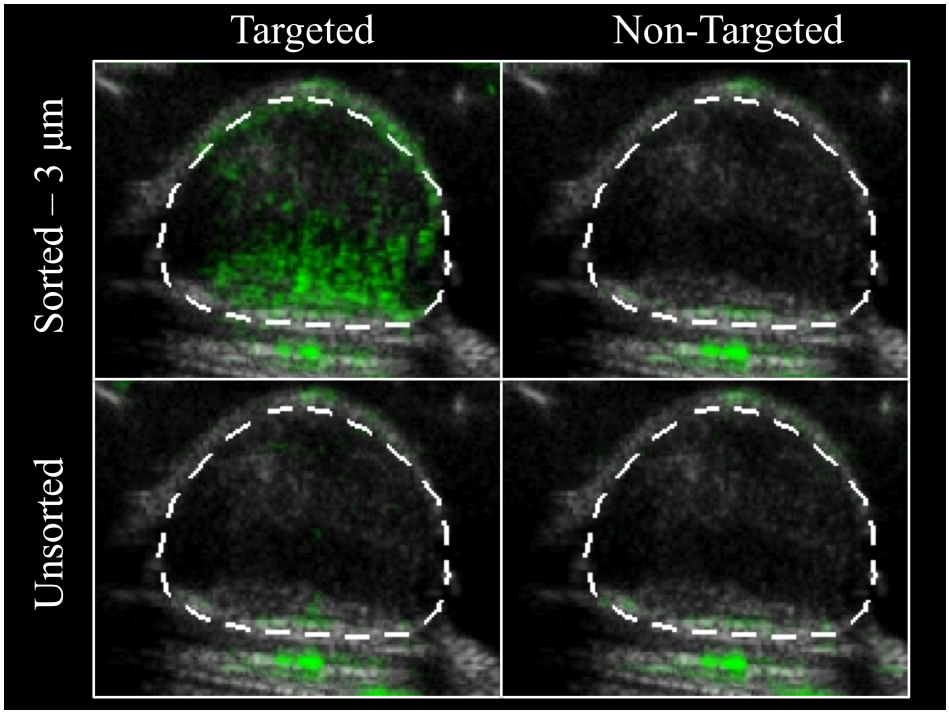

Figure 8.6: Example of image-subtracted targeted and non-targeted data for sorted and unsorted microbubble distributions overlaid with their respective b-mode images.

these results, however, is that the time of image enhancement from larger microbubbles is not necessarily limited by increased filtration from the bloodstream, as one might hypothesize. Further studies will need to be performed to evaluate circulation time of microbubbles as a function of diameter range to establish what size range provides optimal enhancement while maintaining appropriate circulation times.

An increase in bloodstream persistence in USMI provides a unique method to increase binding efficiency. Given that the probability of MCA adhesion is directly proportional to the number of passes through the circulatory system, and sorted 1 μm and unsorted size distributions have relatively short persistence times, sorted 3 μm MCA size distributions are more likely to bind to targeted tissue with their increased circulation times [108; 51; 36; 118; 119]. However, it is unclear from our targeted study what effect, if any, persistence has on the binding population between sorted 3 μm and sorted

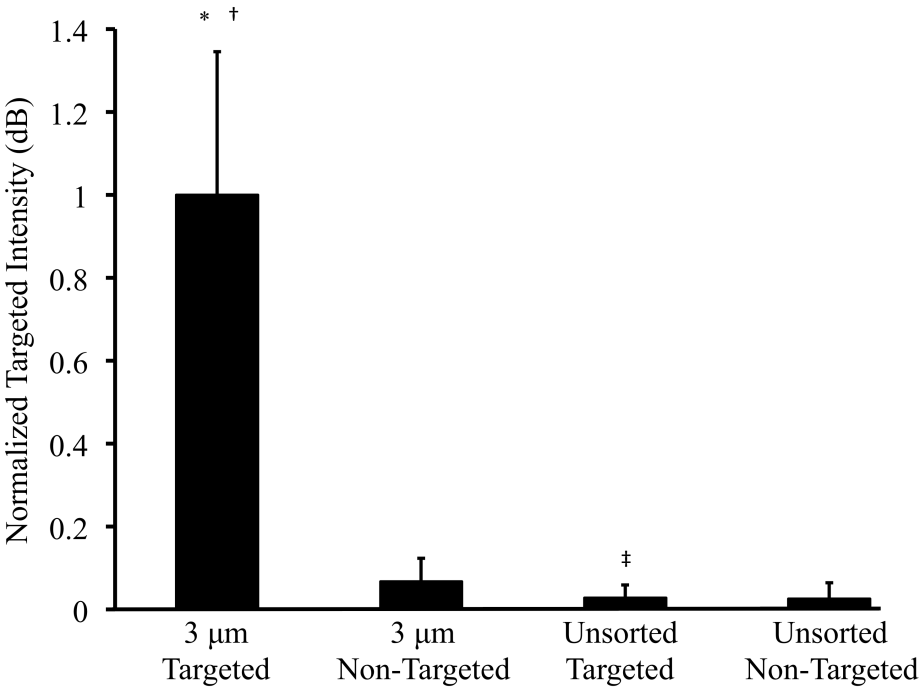

Figure 8.7: Normalized mean video intensity for targeted and non-targeted large and unsorted microbubble distributions. Mean video intensity was taken to be the difference between the mean targeted ROI image section and the mean baseline ROI image section. *$p < 0.05$ compared to unsorted targeted MCAs. †$p < 0.05$ compared to 3 μm control MCAs. ‡$p < 0.05$ compared to unsorted control MCAs

1 μm MCA size distributions. The method for acoustically analyzing targeted agents used in this chapter relies on clearing the freely circulating bubbles from the circulatory system. Given that larger MCA distributions have longer bloodstream persistence times than smaller MCA size distributions, larger targeted MCAs have more time to bind to the targeted tissue. Therefore, the amount of signal intensity related to increased MCA size or increased binding efficiency is unknown. Ironically, this increased circulation time also complicates current USMI techniques because of the need to wait for free agent clearance prior to imaging adherent bubbles. It should also be noted that there is most likely a tradeoff between wait time and binding efficiency. It is possible that the increase in cross-sectional area of the targeted agent is more susceptible to

detachment owing to the increase in shear force by the circulatory system. However, we hypothesize that new techniques will allow near-real-time differentiation of free and adherent agents without waiting for clearance, which will alleviate this concern in the future [111; 112; 122].

In this study, we used sorted 3 μm and unsorted MCA distributions to target angiogenic tumors to determine the relationship between contrast sensitivity enhancement and MCA size. USMI results showed a strong relationship between MCA size and targeted contrast sensitivity with an observed 20-fold increase in video intensity provided by sorted targeted 3 μm MCAs compared to unsorted targeted MCAs. Given the results of the presented perfusion studies and prior *in vitro* work, we assume that the increased backscatter intensity from the targeted sorted 3 μm bubbles was the main component in the sensitivity difference between large and small targeted populations [41]. However, larger microbubbles have a larger surface area, and it is reasonable to assume that they contain more binding ligands than small-diameter bubbles. Therefore, it is possible that the larger MCAs would have a higher probability of binding to a targeted site than smaller MCAs. In contrast, it is also likely that the larger microbubbles may detach faster than the smaller microbubbles owing to shear forces, as mentioned above. We are currently unable to assess these variables *in vivo*, but these aspects should be examined in future *in vitro* studies.

Data also showed that non-targeted sorted 3 μm MCAs had a video intensity compared to baseline greater than that of the unsorted targeted agents. This discrepancy is probably due to a small population of non-specifically bound MCAs in the circulatory system at the time of microbubble destruction. It is reasonable to assume that both sorted 3 μm and unsorted MCA control agents result in some non-specific contrast adhesion; however, sorted 3 μm MCAs produce a larger backscatter intensity inadvertently creating higher values for control populations at a -3 dB gain setting. However,

this small increase in signal from the 3 μm sorted control agents was minor compared to the much larger increase in enhanced signal from the 3 μm targeted agents; therefore, this did not detract notably from the achieved improvements in contrast sensitivity.

In this study, we have demonstrated that a several-fold improvement in contrast sensitivity enhancement can be achieved by tailoring MCA size distributions. This result is especially significant for USMI applications, where the amount of targeted contrast agents retained is typically low, and maximum sensitivity to MCAs is desired. Further work needs to be done to understand persistence effects and binding probabilities related to increased microbubble diameter prior to further optimization of MCA size distributions for use in USMI. Additionally, further *in vivo* studies need to be performed to examine the optimization of the monodispersity of the bubble population and relationship of the mean diameter to the imaging frequency, which are not considered here.

CHAPTER 9

3-D Ultrasonic Molecular Imaging of Angiogenesis

9.1 Introduction

One of the biggest limitations with US imaging, compared to other imaging modalities, is that the field-of-view is less comprehensive [123]. Linear arrays, which are typically used in US imaging are inherently 2-D. Recently, however, 3-D US imaging has become available, largely for cardiac and obstetric applications [124; 125] and more recently for contrast-enhanced perfusion applications [126; 127; 128]. However, molecular imaging with US has traditionally been utilized only with 2-D image acquisition due to the widespread use of one-dimensional linear array transducers and the lack of commercially available US systems with high-resolution contrast-specific imaging modes implemented on 3-D probes.

Our hypothesis is that the application of molecular imaging in 3-D space will provide a more robust evaluation of disease progression than current methods. In this chapter, we demonstrate the application and potential of 3-D USMI of angiogenesis *in vivo* using a clinical US scanner with a custom mechanically scanned transducer system.

Microbubble targeted images were fused with b-mode images in 3-D space to allow for characterization and localization of $\alpha_v\beta_3$ molecular marker expression with respect to tumor volume. Finally, a postmortem immunohistochemical (IHC) analysis performed on multiple tissue slices was compared with the ultrasonic data.

9.2 Materials & Methods

9.2.1 Microbubble Contrast Agents

Lipid solutions for MCAs designed to target $\alpha_v\beta_3$ integrins were created as described in 4.3.3 and 4.3.4. MCAs with a large preferentially-selected mean diameter (3.3 $\pm$ 1.9 μm) have been shown to produce greater backscatter intensities [38; 105; 42] in USMI studies as compared to vial-shaken, unsorted polydisperse distributions. Therefore, all MCAs in this study were sorted as described in 4.3.6. Initial concentrations and size distributions of MCA solutions were determined using an Accusizer 780A. Using these measurements, the MCAs were diluted with PBS to a concentration of 8.0 x $10^8 \frac{\#}{\text{mL}}$ prior to intravenous administration.

9.2.2 Animal Preparation and Contrast Administration

A total of 8 Fischer 344 rats of similar sizes were used for all *in vivo* studies. Tumors were implanted and animals were prepared for imaging as described in 5.3. In all experiments, bolus MCA injections of 100 μL were delivered followed by an immediate flush of at least 200 μL sterile saline to clear any remaining MCAs from the catheter.

9.2.3 3-D Imaging Apparatus

The 3-D US imaging system along with the parameters used to acquire all images in this chapter are as described in 5.2.1, 5.2.2 and 5.2.3. Within all imaging data sets, the CPS gain (-3 dB) and transmit power (MI: 0.18) were kept constant and the

transducer was stepped elevationally every 800 μm.

9.2.4 Image Acquisition

The procedure for performing molecular imaging experiments and its subsequent analysis is described in 6.2. In this study, twenty minutes was determined to be an adequate length of time for this volume of freely circulating contrast agents to be cleared from an animal's system. This was done by examining perfusion wash-out curves for animals with similar weights and given the same dose of MCAs (data not shown). We used Matlab's two-sided Student's t-test to assess the statistical significance of each group. Significance between two different distributions were considered at a value of $p < 0.05$.

9.2.5 Multi-slice IHC Analysis

Tissue Fixation, Processing, Embedding and Sectioning

After USMI was performed, the FSA tumors were extracted for IHC analysis staining for neovessel angiogenesis using a CD31 antibody as previously discussed [43; 104]. Before extraction, the tumor was spot cauterized on the dorsal and left tumor surfaces along the anterior to posterior axis (elevational direction) (Figure 9.1). These cauterized marks were used to preserve the spatial orientation of the tumor after it was removed, such that the tissue face would be perpendicular to the elevational scanning direction (posterior to anterior) of the US transducer. Thus, when processed, the histology slides would approximately correspond to the image displayed with the US system. After extraction, the tumor was segmented into multiple 2 to 3 mm tissue blocks. Finally, each segment was cauterized at a central dorsal position of the tissue face to preserve the orientation of the tumor in later processing steps (Figure 9.1).

Tumor slices were fixed overnight with 4% paraformaldehyde (Electron Microscopy Sciences - Hatfield, PA) in PBS. Fixed tissue was washed for 2 days in PBS prior to being processed into paraffin. Tumor slices were embedded in paraffin blocks while

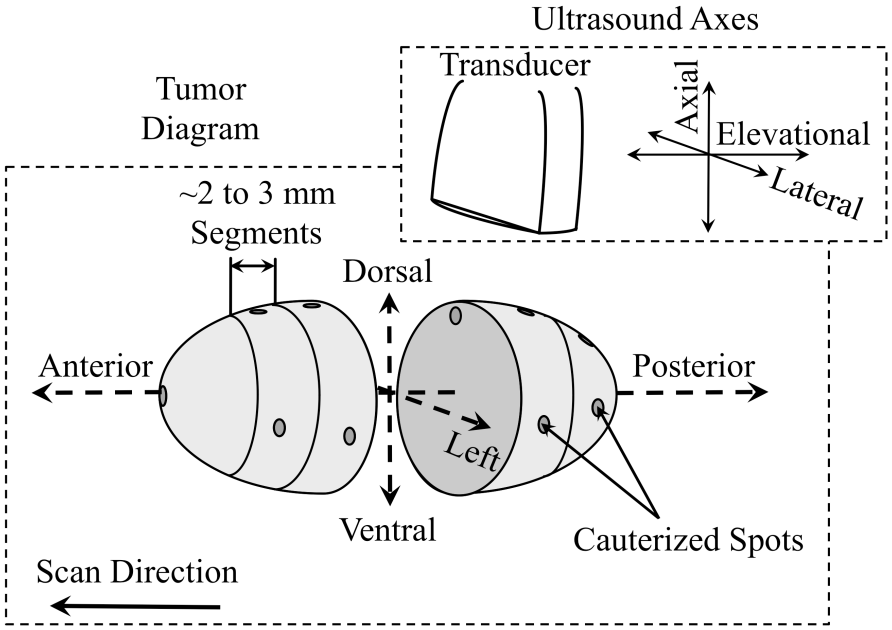

Figure 9.1: 3-D tumor diagram illustrating the anatomical terminology and directional orientation with respect to the transducer for multi-slice histological analyses.

preserving the orientation of the US scan using the cauterized marks. Lastly, tissue sections were mounted on charged slides for histology and IHC processing.

Histology and Immunohistochemistry

Standard methods for histology and IHC were used. Briefly, tissue was deparaffinized with toluene and re-hydrated through a graded series of ethanol and PBS. Nascent vasculature was localized using an antiserum against PECAM-1 (CD31, sc-1506) raised in goat (Santa Cruz Biotechnology - Santa Cruz, CA) diluted 1:200 in normal rabbit serum to a final concentration of 1 $\frac{\mu g}{mL}$. The PECAM-1 IgG was detected using a biotinylated rabbit anti-goat antiserum (BA-5000) (Vector Laboratories - Burlingame, CA) diluted 1:300 in normal rabbit serum to a final concentration of 5 $\frac{\mu g}{mL}$. The anti-goat IgG was localized using streptavidin-peroxidase and 3,3-diaminobenzidine tetrahydrochloride (DAB) (Zymed Laboratories - San Francisco, CA) according to manufacturer's

directions. Antibody incubations were for one hour at room temperature.

Photomicrographs were captured using a BX51 microscope (Olympus - Center Valley, PA) equipped with a motorized 2-D stage driven by a ProScan II controller (Prior Scientific - Rockland, MA). Individual fields were captured at 100x magnification with a DP72 digital camera (Olympus) as 1360 by 1024 pixel Tagged Image File Format (TIFF) files and were assembled into a final image using version 7.7.0.0 of MetaMorph Basic software (Molecular Devices -Downingtown, PA). The original photomicrographs were captured at a resolution of 1.02 μm per pixel. The final photomicrograph montages used for analysis were compressed using the Joint Photographic Experts Group (JPEG) algorithm to reduce their file size and to facilitate their analysis with Matlab software.

Neovascular Quantification

Due to the extremely large file sizes ($\sim$250 MB), the high-resolution images of the stained tissues were re-sized to 20 percent of the original image size. Subsequently, the images were imported into a custom Matlab program for counting neovasculature. First, a user-defined ROI was drawn within the perimeter of the tumor similar to the USMI analysis. At random, ten non-overlapping 1 mm by 1 mm image blocks within the ROI were displayed. Lastly, the stained blood vessels were manually counted in each image. Mean and standard deviations corresponding to the number of new blood vessels per unit area were evaluated and compared within each tumor segment as well as between the multiple sections acquired across the tumor.

9.3 Results

9.3.1 Intra-tumor Analysis

3-D molecular imaging analyses of 8 different animals demonstrated large variations in slice-to-slice mean pixel intensities across different animals' tumors (Animal 6: Mean = 0.07, Spread = 0.04, Animal 5: Mean = 0.78, Spread = 0.68) (Figure 9.2). The spread or the range in the data was calculated as the difference between the image with the highest mean targeting intensity value minus the image with the smallest mean targeting intensity.

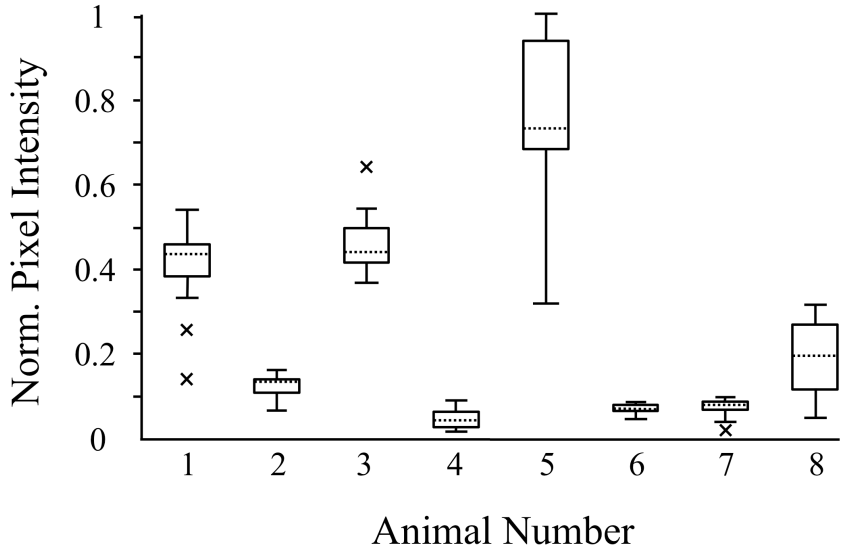

Figure 9.2: Box plots of the mean pixel intensity distributions for each of the eight animals imaged. All values were normalized to the 2-D acquisition with the most MCA targeting. The x symbol represents imaging slices, which were outliers from the distribution.

To further assess intra-tumor variation, mean pixel intensity, normalized to the 2-D acquisition with the most MCA targeting, was plotted as a function of distance relative to the tumor centers for two of the eight most dissimilar animals imaged (Animal #5 = A, Animal #3 = B) (Figure 9.3) to illustrate how microbubble targeting varied

spatially between the two. Mean video intensity (normalized to both tumors' maximum intensity) and standard deviations were 0.77 ± 0.18 and 0.71 ± 0.10 respectively.

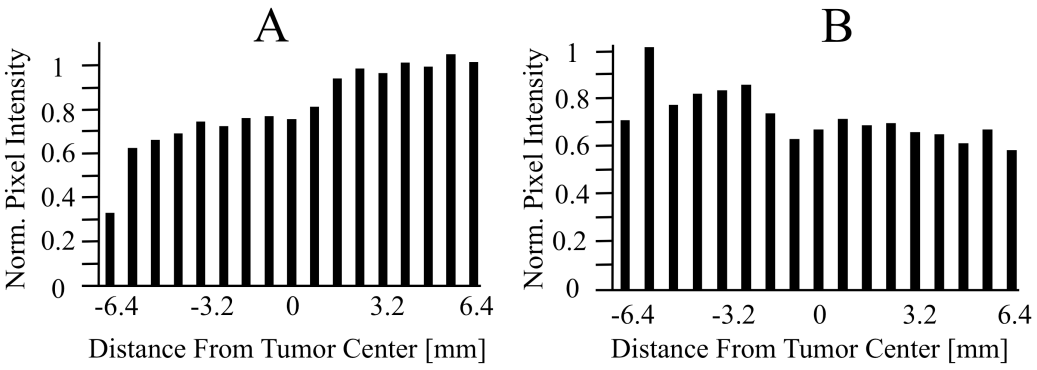

Figure 9.3: Mean pixel intensity per 2-D slice acquisition demonstrating the spatial MCA targeting variability within two different animals. All values were normalized to the 2-D acquisition with the most MCA targeting in each of the two animals. Panel A corresponds to Animal 5 and panel B corresponds to Animal 3.

In addition to slice-to-slice analysis, the degree to which a single imaging plane could misrepresent the entire volume of tissue was determined by calculating the discrepancy between the mean targeted intensity value at the center of the tumor and the mean intensity across all slices in the tumor. This discrepancy was plotted as a percent difference (Figure 9.4) with respect to the mean targeted intensity value at the center of the tumor. Our data indicate that volumetric microbubble targeting could have been underestimated by 28% or overestimated by as much as 16% if only the center slice was acquired.

Lastly, an example 3-D rendering of a heterogeneous tumor (Animal 5) qualitatively illustrates the spatial variation of angiogenic marker expression (Figure 9.5). Panel A shows 3-D isosurfaces of the tumor divided at various locations to illustrate the targeting variation in each user-defined region. Panel B shows each associated targeted

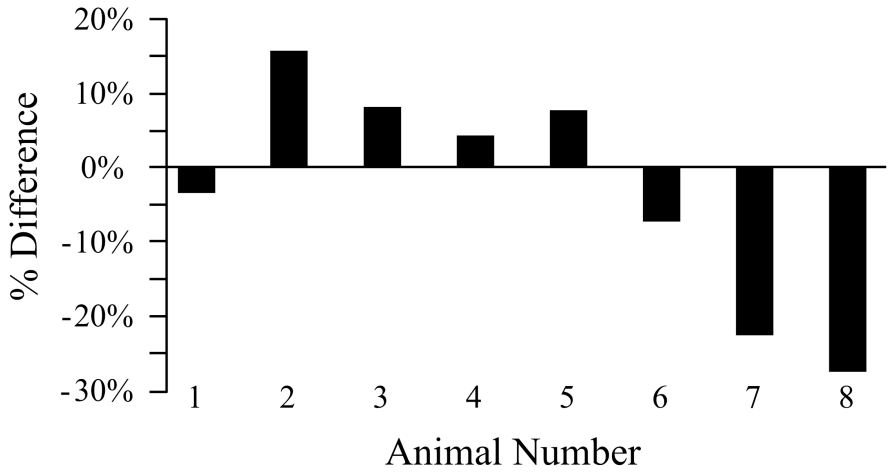

Figure 9.4: Percent difference between mean pixel intensity at center of tumor and mean pixel intensity for all 2-D slices of the same tumor relative to the center value.

acquisition overlaid onto the corresponding b-mode image (traditional 2-D representations).

9.3.2 Inter-tumor Analysis

The distributions of intensity values for all 2-D acquisitions across each animal are compared to each other in the form of box plots normalized to the acquisition with the most microbubble targeting (Figure 9.2). The variance of the mean pixel intensity for the most heterogeneous (Animal 5) and least heterogeneous (Animal 6) tumors was 0.032 and 0.0001 respectively.

Animals 2 and 7 had video intensities that were similar at the center location of each respective tumor (0.10 in Animal 2 versus 0.09 in Animal 7). It is important to note that although the mean targeted intensity values were similar at the center position, the range in targeting between the two different animals were significantly different ($p < 0.05$).

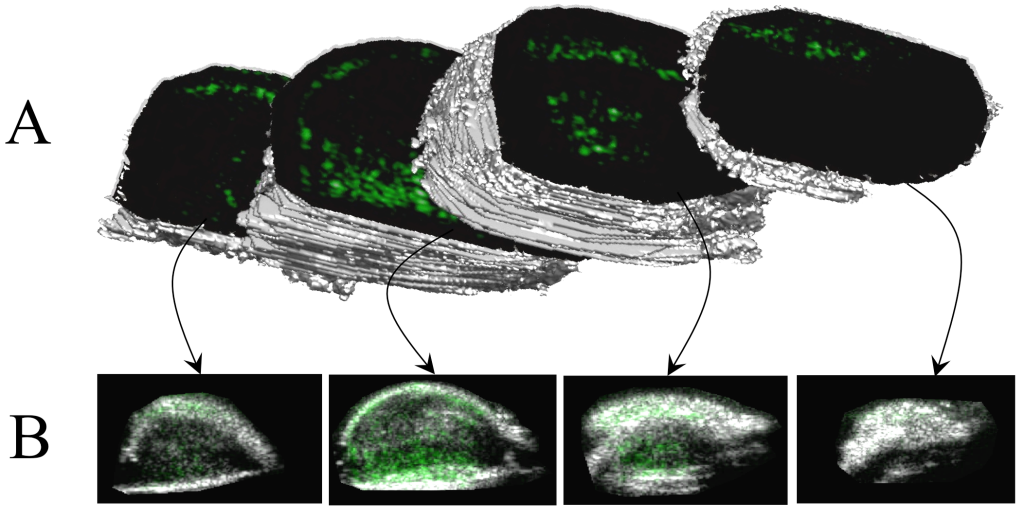

Figure 9.5: A 3-D rendering of an angiogenic tumor with targeted contrast overlaid on b-mode images. This image was created in Matlab by forming an isosurface from the user-defined regions of interest in each 2-D acquisition plane.

9.3.3 Approximating Error in Analogous 2-D Study

In this study, we estimated the magnitude of potential misalignment error in applications where the transducer is moved from a fixed clamp and repositioned. The potential error was obtained by calculating the absolute value of the difference in mean targeting between all adjacent imaging planes relative to the volumetric mean of the tumor, as indicated by the following equation:

$$RLV = \frac{1}{I_m} \sum_{i=1}^{N-1} \left| \frac{I_{i+1} - I_i}{N} \right| \tag{9.1}$$

where I_m is the mean targeted bubble intensity throughout the entire tumor and N is the number of 2-D acquisitions. This quantity, designated as the "Relative Local Variability" (RLV), determines how much variability there is between adjacent slices along the elevational scanning direction. The RLV between adjacent planes for all tumors was 13.4%. The animal with the most relative variability between adjacent image

slices, and thus the highest likelihood of error resulting from a transducer repositioning, was 32.1% (Animal 4) while the animal with the least likelihood of error had an RLV of 6.8% (Animal 5) (Figure 9.6).

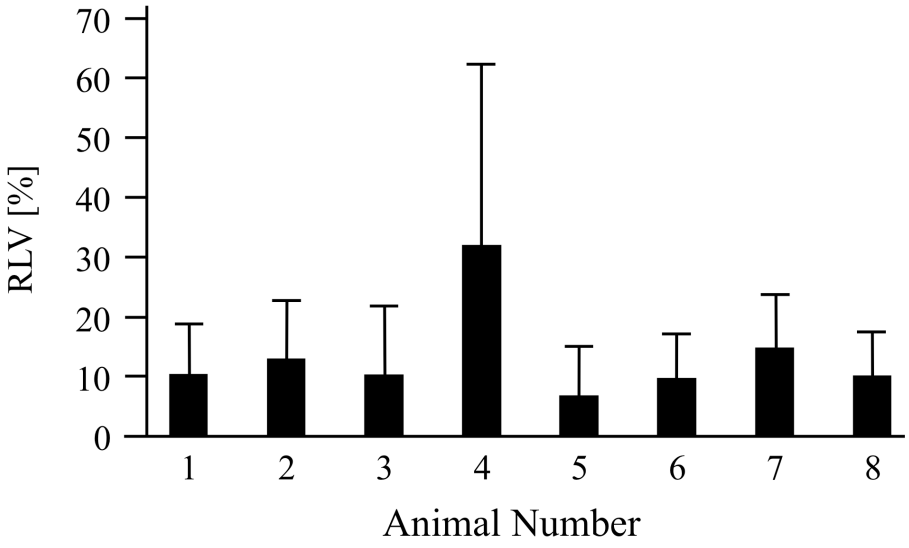

Figure 9.6: Relative Local Variability (RLV), or average slice-to-slice variation, expressed as a percentage of the volumetric mean MCA targeting. Error bars are standard deviations of the adjacent slice relative differences.

9.3.4 Multi-slice IHC Analysis

CD31 staining was performed on three different FSAs to corroborate the conclusion drawn from the USMI data that tumor tissue is heterogeneous. The number of CD31 stained blood vessels per unit area for each segment was compared to the US data (Table 9.1). All histological data was normalized to the segment that contained the largest mean blood vessel density. All US molecular imaging data was normalized to the mean pixel intensity of the acquisition with the most MCA targeting. The data shows that there is large variation in neovasculature in intra- and inter-tumor analyses.

IHC data demonstrates that there is a large variation in quantity of neovasculature and that it roughly correlates to the amount of microbubble targeting in the USMI

Table 9.1: Blood vessel density (mean and standard deviation) for each tumor segment for each tumor as compared with the corresponding targeted intensity obtained with USMI. All values were normalized to the maximum blood vessel density for each tumor.

		Histology	**Ultrasound**
Animal #	Approx. Dist. From Tumor Center [mm]	Norm. Mean Blood Vessel Density [Count/Unit Area]	Norm. Mean Targeting Intensity [Intensity/Unit Area]
1	-3.8	0.52 ± 0.12	0.13
	-1	0.51 ± 0.28	0.28
	1.4	0.27 ± 0.38	0.26
	4.1	0.44 ± 0.38	0.21
	5.3	0.29 ± 0.27	0.11
	Total Mean	**0.40**	**0.20**
2	-2.1	0.52 ± 0.24	0.74
	1.9	1.0 ± 0.56	1.00
	5.9	0.58 ± 0.34	0.28
	Total Mean	**0.70**	**0.67**
3	-1.8	0.59 ± 0.44	0.65
	3.6	0.70 ± 0.27	0.58
	4	0.97 ± 0.34	1.00
	Total Mean	**0.75**	**0.75**

data (Figure 9.7). Data shows that the normalized mean pixel intensity of the US acquisitions has a similar trend as the histological analysis. Furthermore, targeted MCA overlays on b-mode images illustrate the variability in microbubble targeting to $\alpha_v\beta_3$ along with representative images of the stained histology. Exact alignment and orientation between the tumor segments and the USMI data was unattainable due to the difficulty of perfectly registering histology and image data, and thus a more rigorous and quantitative correlation between US and histology was not attempted and considered to be outside of the scope of this project.

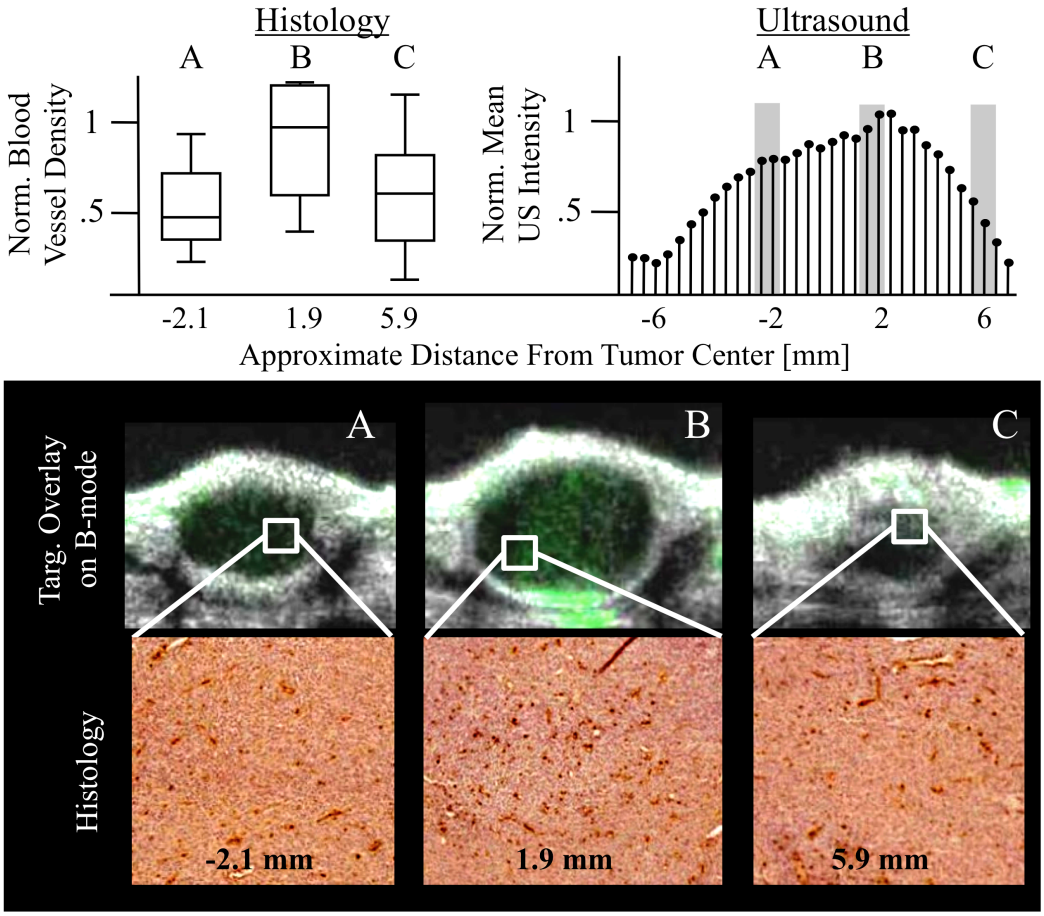

Figure 9.7: Upper Left Panel: Distributions of new blood vessel density at each tumor segment in boxplot format. The data was normalized to the slice B mean so that the scales were similar to the corresponding USMI analysis. The approximate elevational distance from the tumor center is indicated below the distribution. Upper Right Panel: Normalized mean pixel intensity per 2-D slice acquisition for USMI analysis. Data was normalized to the 2-D acquisition with the most targeting. Bottom Panel: The top images are targeted overlays on b-mode images illustrating microbubble targeting to $\alpha_v\beta_3$.The bottom images are representative of the stained histology samples at the approximate locations specified. Dark red color indicates neovasculature stained with CD31 antibodies.

9.4 Discussion and Conclusion

Until recently, traditional b-mode has been predominantly 2-D. This has not been a limiting factor for applications in which the user is imaging anatomical structures,

because adjusting the transducer manually can vary the image plane. Since molecular imaging with US typically uses a more precise subtraction method for quantifying molecular marker expression, image acquisitions are obtained by placing the transducer in a fixed clamp on an anesthetized animal [43; 44; 60; 61; 108; 114]. For over a decade, this 2-D molecular imaging method has provided valuable insight into the detection of biomolecular markers for numerous applications previously mentioned. In this chapter, we illustrate the advantages of molecular imaging in 3-D.

Data illustrated that 3-D USMI presents a more robust assessment of molecular marker expression throughout the tumors than standard 2-D US. In the case of non-homogeneous tumors (which is common [129]), it is easy to incorrectly assess the tumor characteristics based on only a single cross sectional US slice. An example 3-D tumor rendering (Figure 9.5) illustrated this point through visualization of four different targeted imaging planes with unique spatial distributions of $\alpha_{\mathrm{v}}\beta_3$ expression. In a traditional 2-D analysis, it is possible that any one of these acquisitions would be used to assess the angiogenesis throughout the entire tumor. However, it is evident that the mean MCA targeting in that single plane is not the same in all areas of the tumor, which was confirmed by the relatively large variations in targeting across the tumors of each of the 8 different animals. The importance of a 3-D targeted imaging approach was further corroborated by the analysis of the percent difference between targeting at the center of the tumor relative to the overall mean targeting throughout the tumor. This analysis, which approximates the error between the mean targeting of a 2-D and a 3-D molecular imaging study, indicates that quantification of angiogenesis can be significantly underestimated or overestimated by 2-D imaging. Therefore, implementing a 3-D system for molecular imaging with US provides comprehensive details that would otherwise be missed with a traditional 2-D analysis.

In this chapter we also compared traditional 2-D USMI and its effectiveness by

analyzing the variation in angiogenic biomarker expression in individual tumors. We showed that some tumors had similar mean targeting values over the volume of the tumor while the range and variance of targeting for the tumor was significantly dissimilar. Consequently, a single-slice 2-D targeting analysis could lead to conclusions based on incomplete data when comparing two different tumors due to the large targeting variations between them, and therefore incur additional error.

To further examine the error potentially caused by undersampling in 2-D molecular imaging with US, we analyzed the RLV in MCA targeting between all adjacent imaging planes. In 2-D serial studies, slice position and orientation is essential in maintaining a consistent sequential study. Therefore, using the RLV metric, we quantified the potential error associated with applications in which the transducer is removed from a fixed clamp and repositioned. In this study, the RLV was approximately 13%. While this approximated error may seem low, a 3-D analysis would inherently include all microbubble targeting, thus eliminating the possibility for this type of error.

In this study, we performed a multi-slice immunohistological analysis on three different tumors. This data corroborated our conclusion that the angiogenesis within our tumors was heterogeneous, necessitating a more comprehensive volumetric analysis for adequate characterization. Similar to USMI, variation in mean blood vessel density was considerable in some locations and modest in others, thus reaffirming our conclusion. It is important to note that, although we see a general trend between molecular imaging and histology, it was too difficult to correlate directly. This is due to several factors. First, although CD31 and $\alpha_v\beta_3$ expression are biomarkers for neovasculature, they are not equivalent. Substitution for CD31 instead of $\alpha_v\beta_3$ immunohistology was chosen due to the challenge of obtaining specific antibodies directed against rat $\alpha_v\beta_3$ [130]. Second, it was not possible to exactly match the imaging plane of the histological sample to the US dataset due to the complex orientation and alignment issues, and tissue

deformations associated with extraction. Regardless, the histology results lead us to the same conclusion as the USMI analyses: a single-slice 2-D analysis of neovasculature could easily misrepresent the true value exhibited by the entire volume of the tumor.

In this chapter, we demonstrated the potential of 3-D USMI of angiogenesis *in vivo*. While other clinically relevant applications were not explored, the extension of molecular imaging with US to 3-D provides an opportunity to improve the quality of data collected as well as the accuracy of conclusions drawn from these studies. Based on these demonstrated advantages, we hypothesize that 3-D molecular imaging will become more commonplace as high-resolution 3-D transducers with non-linear contrast imaging capability become more widely available on commercial US systems.

CHAPTER 10

ARF - Enhanced Ultrasonic Molecular Imaging

10.1 Introduction

10.1.1 Background

Over the past decade, *in vivo* USMI research has relied on passive targeting as the basis for this technique. Passive targeting is microbubble adherence that does not require any additional forces for binding. Unfortunately, passive targeting in USMI experiments has resulted in poor binding efficiency, which limits its advancement in many applications that require greater numbers of targeted microbubbles.

ARF can produce a force on particles suspended in liquids such as microbubbles [46]. A transducer directing non-destructive energy perpendicular to the blood flow can displace moving MCAs to the wall of the vessel opposite the sound source increasing the probability of microbubble-endothelium interactions as illustrated in Figure 10.1 [46]. Forcibly displacing MCAs to the wall of the vessel would make it possible to increase the concentration of targeted MCAs during USMI experiments, which has been hypothesized but not demonstrated *in vivo* with a clinical US system [46; 47; 48].

 Portions reprinted, from RC Gessner*, JE Streeter*, R Kothadia, S Feingold, and PA Dayton. "An *In Vivo* Validation of the Application of Acoustic Radiation Force to Enhance the Diagnostic Utility of Molecular Imaging Using 3-D Ultrasound" Ultrasound Med Biol, 2012; 38(4): 651-660. *Equal Contributers

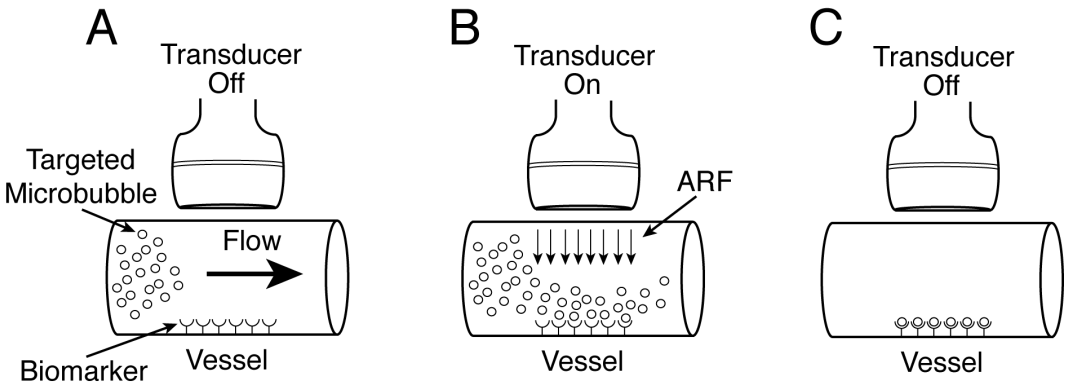

Figure 10.1: Example of Acoustic Radiation Force-Enhanced Targeting. A: Illustration of targeted microbubbles flowing through a vessel that expresses a particular biomarker. B: When the transducer directs non-destructive energy perpendicular to the blood flow, the energy can displace moving MCAs to the wall of the vessel opposite the sound source. C: There is a higher probability of microbubble-biomarker interactions, thus an increase in targeting.

10.1.2 ARF and Molecular Imaging

Since early observations of ARF on MCAs *in vivo*, researchers have speculated about the utility of this force to push populations of microbubbles in a direction normal to their flow in a patient's vasculature, thereby guiding them out of circulation and against the wall of a vessel [46]. It has been hypothesized that increasing ligand-receptor proximity and reducing the velocity of flowing microbubbles would greatly increase the amount of targeted microbubble adhesion in molecular imaging studies [131; 48; 47; 110; 51]. *In vitro* studies of ARF on microbubbles have demonstrated the ability to increase the quantity of microbubble adhesion over 100 fold compared to molecular targeting without ARF [47]. *In vivo* observations performed by intravital microscopy have also demonstrated between four and twenty-fold increases (depending on the vascular environment) in the amount of targeted microbubbles retained in microvasculature after ARF pulses [48]. Similarly, with the development of acoustically-active drug delivery vehicles, it has been hypothesized that ARF could be a mechanism to increase vehicle

and drug concentration at the desired target site via US. Researchers have shown the utility of ARF to mediate the concentration of several types of potential therapeutic delivery vehicles [132; 133; 134].

It has also been proposed that ARF might play a role in pulse sequences designed to enhance the detection of targeted contrast agents in molecular imaging. Many current molecular imaging studies involve the use of a waiting period, typically 5 to 20 minutes, for free (unbound) microbubbles to clear the circulation before imaging of adherent targeted agents can be performed [135]. This limitation makes USMI a slow process and likely results in loss of detected signal as bound microbubbles can detach or degrade over the waiting period. It has been shown that rapid increase in adhesion of targeted microbubbles using ARF can be utilized to help delineate signal from free and bound contrast agents [136; 112].

To date, literature demonstrating the application of ARF *in vivo* to improve microbubble targeting has been scarce. This is likely due to a disparity between the types of acoustic pulses used for imaging by clinical and pre-clinical imaging systems, and the acoustic regime over which ARF-induced microbubble displacement is most efficient. Microbubble translation is maximized near the bubble's resonant frequency. For most efficient translation, a large duty cycle is required, and the MI must be low enough to avoid microbubble destruction [131]. A long duty cycle and low MI are typically not parameters beneficial for US imaging, and thus it is likely that the paucity of *in vivo* ARF-enhanced molecular imaging data is due to the fact that these pulse sequences are not intuitively available on commercial US equipment.

In this chapter, we describe the implementation of a widely-used clinical US system, the imaging parameters of which we have adjusted in order to produce ARF of a magnitude substantial enough to cause non-destructive bubble translation. Following the ARF pulses used to enhance contrast targeting, we utilize contrast-specific imaging

pulse sequences for molecular imaging. This study uses a FSA tumor model to illustrate the effect of ARF-enhanced molecular imaging compared to conventional passive molecular imaging. Additionally, we investigate the effect on non-specific adhesion caused by the intentional push of microbubbles away from the center of the lumen toward the distal walls within tumor vasculature. Results from preliminary *in vitro* studies are also presented which suggest that the pressure of the ARF pulse sequence is a significant factor in promoting lasting bond kinetics between molecularly targeted microbubbles and their target integrins, and that one must balance detrimental over-pushing with ineffective under-pushing to achieve the optimal ARF-enhanced molecular imaging protocol.

10.2 Materials & Methods

10.2.1 Microbubble Contrast Agents

All microbubbles used in our studies were formulated as previously described in 4.3.3, 4.3.4, and 4.3.6. Briefly, targeted agents were fitted with a cRGD peptide known to bind to $\alpha_{\mathrm{v}}\beta_3$, an integrin over-expressed on angiogenic endothelium [22; 38]. Likewise, non-targeted microbubbles were produced with a similar lipid formulation, but without the targeting ligand as described in 4.3.2, 4.3.4, and 4.3.6. Both targeted and non-targeted bubbles were of a diameter size distribution centered at 1.6 μm.

10.2.2 Imaging System

The 3-D US imaging system along with the parameters used to acquire all images in this chapter are as described in 5.2.1, 5.2.2 and 5.2.3. Within all imaging data sets, the CPS gain (-10 dB) and transmit power (MI: 0.18) were kept constant. The elevational step-size used in this study was 400 μm.

For volumetric radiation force administration and imaging, the transducer was swept

in the elevational direction by a computer-controlled motion stage interfaced through LabView to a desktop computer as previously described in 5.2.4. The amplitude of the ARF pulses was modulated by using the power output dial of the US system. The output dial to pressure amplitude relationship used in this study was as follows: -7 dB = 4 kPa, -3 dB = 13 kPa, 0 dB = 21 kPa.

10.2.3 Calibration

Acoustic pressure measurements were determined by a calibrated needle hydrophone (model: HNA-0400, Onda - Sunnyvale, CA) in a water tank. The acoustic pressures produced by the linear array transducer in PW Doppler mode at the previously mentioned parameters were measured at 100 μm increments in a 2.2 cm x 0.4 cm area in front of, and parallel to, the aperture using the needle hydrophone. This region of the acoustic pressure field was mapped at 0.5, 1, 1.5, and 2 cm distances from the aperture, for seven different power output settings. The peak negative pressure was measured at each spatial location and power output setting. These pressures were between 8 and 28 kPa for the system output setting studied, and the pressure field deviated by less than 10% at the locations between 0.5 and 2 cm from the aperture face (in the water tank).

10.2.4 *In Vitro* Studies: Effect of ARF Pressure

In order to assess the relationship between output pressure and microbubble translation efficiency, an optical-acoustical system was constructed to enable visualization of microbubble translation during pulsing. A Photron high-speed camera (Model APX-RS San Diego, CA) was fitted with a 60x water immersion objective lens (LUMPlanFI/w, Olympus - Melville, NY) through a single-tube microscope (Edmund Optics, Barrington, NJ). The objective was inserted through a latex seal into the water tank and aligned confocally with and at 90 degrees to the linear array transducer (Figure 10.2A).

A 200 μm acoustically and optically transparent cellulose tube (Spectrum Labs, Rancho Dominguez, CA) was placed at the mutual focus, and a fiber optic illuminator was used as a light source for the camera. A dilute concentration of contrast agents was pumped through the tube and ARF pulses were applied perpendicularly to both the flow direction and microbubble buoyancy. Videos were acquired of the contrast agents as they were pushed by the ARF pulses across the diameter of the tube. Data were analyzed offline and the spatial locations of the contrast agents were mapped throughout their translation using a custom-designed program in Matlab. Bubble motion was tracked at each of the pressure outputs, yielding a relationship between ARF-induced translational bubble velocity and acoustic pressure amplitude.

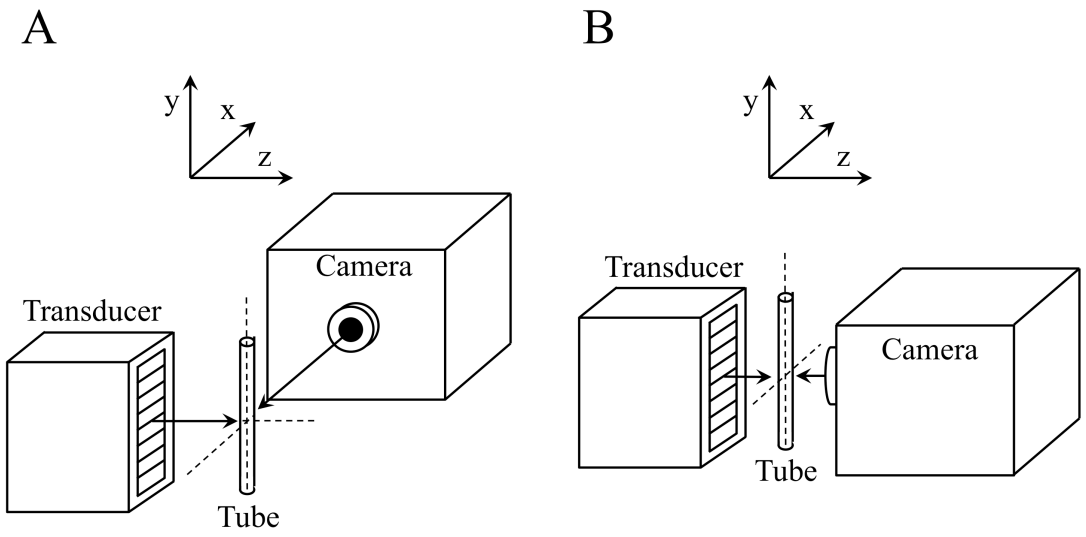

Figure 10.2: Experimental diagrams for the *in vitro* characterizations of the effects of radiation force on microbubbles. A: System used to determine the relationship between microbubble translational velocity and output pressure from the transducer. B: System used to examine the effects of secondary radiation force on contrast agents after making contact with the tube wall. In panel A, the optical axis is along the x direction, the acoustic axis is along the z direction and the microbubble flow axis is along the y direction. Similarly, in panel B, the optical axis and the acoustic axis are along the z direction and the microbubble flow axis is along the y direction.

A second study was performed in which the axial dimension of the transducer was

aligned with the optical axis, and ARF pulses were used to push contrast agents toward the wall of the tube closest to the lens (Figure 10.2B). The purpose of this study was to visualize the behavior of microbubbles at the tube wall after initial ARF pulses had successfully pushed them to the boundary, and thereby quantify conditions where "over-pushing" occurred. We define over-pushing as any ARF setting that caused microbubble destruction, or aggressive lateral motion along the wall (i.e. motion that would likely cause adherent microbubbles *in vivo* to be knocked free and thus be detrimental to molecular imaging studies). Since our bubbles were not targeted to the tube wall, it was possible to observe their motion as an indication of both the lateral component of primary and secondary radiation forces acting on them at the liquid-tube interface. Videos of the bubbles were acquired for several seconds as they were pushed into the wall by ARF pulses, and analyzed later offline. Data were processed with a pixel-wise standard deviation projection through the time axis, thereby quantifying the lateral movement of the bubbles after hitting the wall.

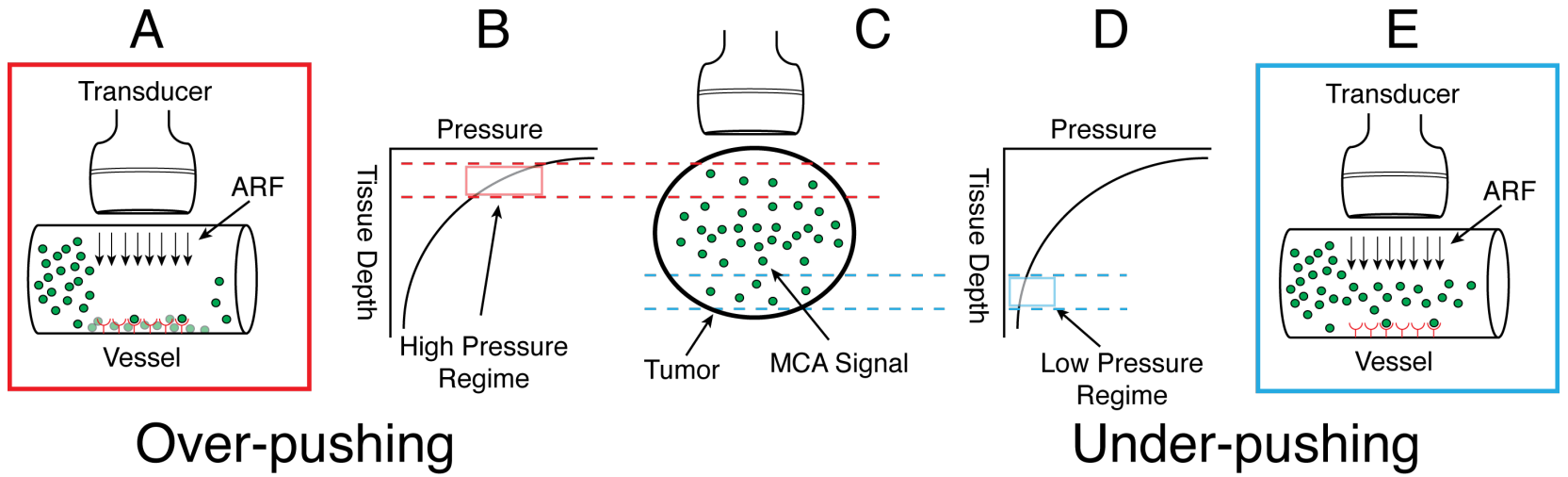

Figure 10.3: Example of Over-Pushing and Under-Pushing in Acoustic Radiation Force-Enhanced USMI. A: Illustration of over-pushing microbubbles in a vessel. B: Example curve of pressure versus the depth into tissue due to acoustic attenuation. Over-pushing regime, outlined in red, is where the ARF pressure is higher than the required force to move MCAs to the vessel wall. C: Illustration of a transducer interrogating a tumor with targeted MCAs. The region closest to the transducer has fewer targeted MCAs due to over-pushing. Likewise, the region farthest from the transducer also has fewer targeted MCAs due to under-pushing. D: Example curve of pressure versus the depth in tissue due to acoustic attenuation. Under-pushing regime, outlined in blue, is where the ARF pressure is lower than the required force to move MCAs to the vessel wall. E: Illustration of under-pushing microbubbles in a vessel.

10.2.5 *In Vitro* Studies: Estimating Optimal *In Vivo* Study Parameters

It is known that the amount of ARF experienced by a defined population of microbubbles is a function of the acoustic pressure and the exposure time in the acoustic field. Prior to *in vivo* studies, we estimated optimal experimental parameters for administering ARF to a volume of tissue in which targeted contrast agents were circulating. We chose to utilize a fixed translational speed of 1 $\frac{\text{mm}}{\text{s}}$ for the mechanically scanned transducer, as well as a fixed duty cycle for all ARF administration. The optimal pressure, P_o, was necessarily a balance between efficient bubble translation and non-detrimental bubble-wall interactions. Our goal was to design an experimental protocol in which ARF was applied uniformly across a volume of tissue. Due to the effects of tissue attenuation, P_o was not constant through the entire depth of tissue. This necessitated a compromise between over-pushing in shallower regions of tissue, and under-pushing at deeper regions of tissue (Figure 10.3).

The optimal setting was estimated by computing a cumulative error-function (CEF) defined as

$$CEF = \int^{D} \mid P_o - P(z) \mid dz \tag{10.1}$$

where $P(z)$ was the pressure of the radiation force beam derated for attenuation at depth z into the tumor with an axial diameter D. Compensating for tissue attenuation is achieved via the formula

$$P(z) = P_i e^{-\alpha z} \tag{10.2}$$

where α is the attenuation coefficient for the tissue [137]. A constant tissue attenuation of 0.6 $\frac{\text{Np}}{\text{cm}}$ was assumed for the tumors used in the *in vivo* portion of the study, as this falls within the range of attenuation values previously measured [138; 139]. The

units of equation 10.1 are in kPa, though the true values returned by the equation are less important than the relative values between different power output settings. We computed the CEF for each of the output settings on the US system as a method for estimating the optimal ARF pressure amplitude for a given tumor diameter. Similarly, we could estimate the axial distance travelled by microbubbles, D_a, within a volume of tissue as a result of the ARF pulses by computing

$$D_a(z) = (velocity) \cdot (time) = (m \cdot P(z)) \cdot (\frac{w_b}{v_T}) \tag{10.3}$$

where m is the slope of the curve for velocity of microbubbles as a function of pressure (determined by the *in vitro* experiments with the schematic seen in Figure 10.2A, with units $\frac{\text{m}}{\text{s}\cdot\text{kPa}}$, $P(z)$ is the pressure of the ARF beam at depth z, w_b is the elevational width of the ARF beam, and v_T is the elevational sweep velocity of the transducer during the application of ARF. Thus, the first term in parenthesis will yield the average velocity of the microbubbles exposed to ARF, and the second term will yield the amount of time they are traveling. This calculation assumes an infinite potential path length (i.e. no tube wall to prevent the bubble from being steadily translated).

10.2.6 *In Vivo* Experiments

A total of 8 Fischer 344 rats were used for studies of ARF-enhanced and conventional molecular imaging (hereafter called "passive targeting" studies, i.e. those not implementing ARF). Tumors were implanted and animals were prepared for imaging as described in 5.3. The appropriate volume of stock solution was added to the catheter via a micropipette tip and flushed with 100 μL of sterile saline such that a contrast dose of 2 x 10^8 bubbles was administered consistently. Because of the dose limitations with the injected volume of saline and contrast into the animals, two different types of studies were performed over several days to examine (a) the effect of ARF pulse

amplitude on microbubble targeting efficiency relative to passive targeting, and (b) the effect of ARF at promoting non-specific adhesion in control bubbles relative to targeted bubbles also exposed to ARF.

For study type (a), each animal underwent four distinct injection and ARF protocols in the following order: (1) passive targeting (no application of ARF) using targeted microbubbles (2) application of ARF with a pressure of 4 kPa using targeted microbubbles (3) application of ARF using a pressure of 13 kPa with targeted microbubbles (4) application of ARF with a pressure of 21 kPa using targeted microbubbles. After each of these four imaging protocols, there was a minimum wait time of 10 minutes to ensure that there were no circulating microbubbles remaining. Similarly for study type (b), each animal underwent distinct injection and ARF protocols in the following order: (1) passive targeting with control microbubbles (2) application of ARF with a pressure of 13 kPa with control microbubbles (3) passive targeting with targeted microbubbles (4) application of ARF with a pressure of 13 kPa with targeted microbubbles. Between each type (b) experiment, there was a minimum wait time of 10 minutes to ensure that there were no circulating microbubbles remaining in the tumor vasculature. In order to compare type (a) and type (b) experiments, data were normalized to the mean image intensity within the volumetric passive targeting image data (using targeted microbubbles without application of ARF) in each animal because this imaging protocol occurred in both type (a) and type (b) studies.

Before the bolus injection, the system was set to the ARF parameters described in 5.2.4. Then, the transducer was swept at a constant speed of 1 $\frac{\text{mm}}{\text{s}}$ across the tumor volume after contrast agents were administered to the animal, for a total of 10 passes after the injection. After waiting approximately 10 minutes for freely-circulating bubbles to clear from the animal's system, the procedure for molecular imaging experiments and its subsequent analysis was performed as described in 6.2. The number of animals

imaged at each setting were as follows: 4 kPa: N = 5, 13 kPa: N = 7, 21 kPa: N = 5). During passive targeting studies, ARF pulses were not administered (N = 4). The statistical significance of our comparisons between the mean microbubble targeting measured by the different imaging study settings was assessed by using Matlab to implement a two-sided Student's t-test assuming equal variances. Significance between two different distributions were considered at a value of $p < 0.05$.

10.3 Results

10.3.1 *In Vitro* Studies: Effect of ARF Pressure

The positions of multiple bubbles ($4 \leq N \leq 10$) were tracked through space and time and a linear relationship ($R^2 = 0.953$) between velocity and radiation force amplitude was observed with a slope of $\sim$5.0 $\frac{\mu m}{s \cdot kPa}$ (Figure 10.4A). For this linear curve fit, the y-intercept was set to 0 (corresponding with a velocity of zero for microbubbles not exposed to ARF).

At each acoustic pressure setting tested between 8 and 28 kPa, the ARF pulses were able to force the microbubbles out of the center of the cellulose tube and against the wall. As the pressure was increased, the aggressiveness of the lateral bubble movement and aggregation due to secondary radiation force increased (Figure 10.4B). It was hypothesized that the secondary radiation force at pressures greater than 10 kPa would not facilitate lasting ligand-integrin bond kinetics. Thus, P_o was estimated to be 10 kPa, as this setting would provide the best compromise between efficient bubble translation ($\sim$50 $\frac{\mu m}{s}$) and minimization of lateral movement after contact with the vessel wall.

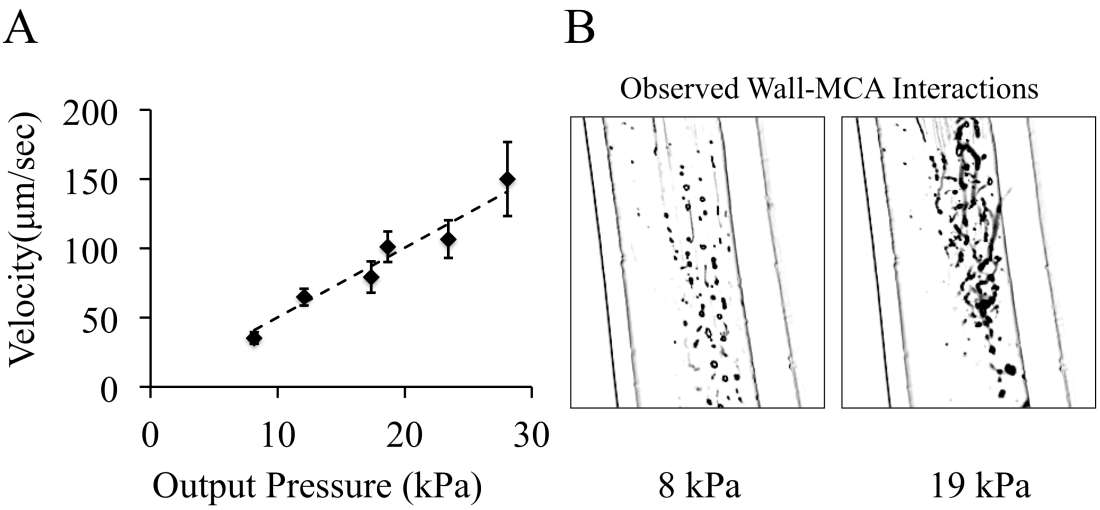

Figure 10.4: Results from optical observations of *in vitro* radiation force on microbubbles. A: The translational velocity of contrast agents as a function of radiation force pressure amplitude. B: Images of standard deviation projections of microbubble lateral translation along the tube wall during radiation force pulsing at high (19 kPa) and low (8 kPa) pressures. As the pressure is increased, lateral motion along the wall caused by secondary radiation force can be clearly visualized as non-spherical trails. Note: the displayed images are negatives of the actual projections - large values appear dark in these images.

10.3.2 *In Vitro* Studies: Estimating Optimal *In Vivo* Study Parameters

The CEF computations demonstrated that there was no single pressure appropriate for all tumor sizes. A 2-D surface plot of the CEF values illustrates how error can be minimized by modulating initial ARF pressure (Figure 10.5A). The optimal initial ARF pressure to maximize targeting efficiency through the tumor volume was determined by taking the minimum value of the CEF for any given tumor size. The CEF predicted that the 13 kPa pressure setting would be the most effective *in vivo* protocol for a 1 cm tumor. A 4 kPa and a 21 kPa setting were also tested *in vivo* to compare the relative targeting efficiencies to the 13 kPa setting predicted by the CEF model.

The calculations of D_a, the expected distance microbubbles would translate *in vivo* along the ARF beam's propagation axis, revealed that both the initial push pressure

and the depth into tissue determined whether a contrast agent would be sufficiently pushed out of circulation to the luminal wall (Figure 10.5B). In a previous histological analysis of vessels within xenografted tumors, 100 μm was the upper bound on the range of vessel diameters [140]. It was predicted that the three pressure settings tested *in vivo* would provide sufficient microbubble translation ($D_a \leq 50$ μm) at tissue depths less than 3.12 cm, 2.4 cm, and 0.51 cm for the 21 kPa, 13 kPa and 4 kPa ARF amplitudes respectively.

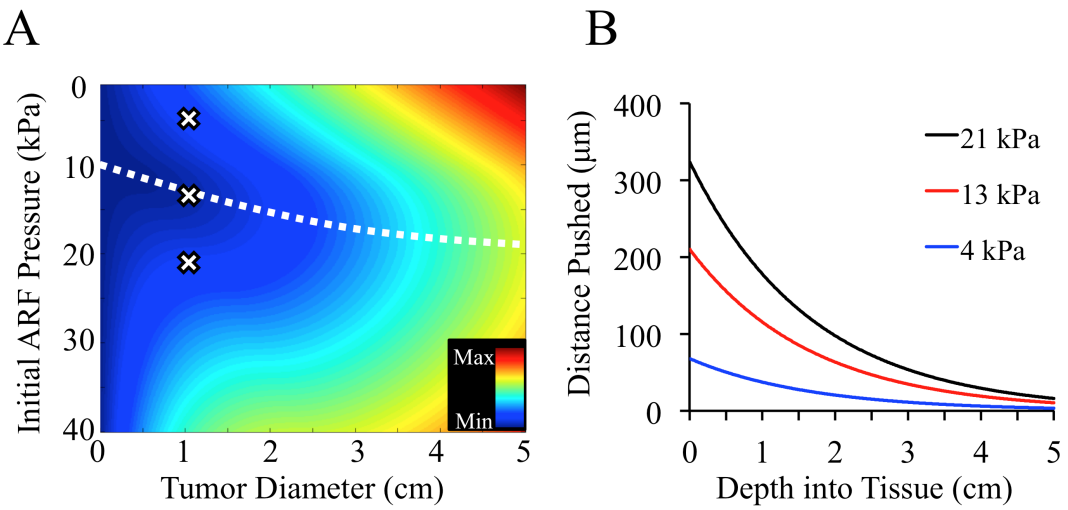

Figure 10.5: The CEF plotted as a function of initial ARF push pressure and tumor diameter. Minimizing the CEF at a given tumor diameter provides the basis for estimating the optimal push protocol for an *in vivo* study (white dashed line). The X's illustrate the three output settings that were tested and compared in the *in vivo* validation studies. B: Simulations predicting the distance a microbubble would be pushed by ARF pulses for the three different initial pressure amplitudes as a function of depth into tissue.

10.3.3 *In Vivo* Results

Microbubbles targeted to angiogenic vasculature were used to compare ARF-enhanced targeting to conventional passive targeting (Figure 10.6). Of the tested ARF pulsing schemes, the maximum increase in microbubble targeting, as measured by mean pixel

Table 10.1: A summary of the percentage of animals (top) and percentage of 2-D image slices (bottom) that exhibited a greater degree of microbubble targeting in the ARF-enhanced targeting studies relative to the passive targeting studies.

	RF-4/cRGD$^+$	RF-13/cRGD$^+$	RF-21/cRGD$^+$
% of Animals Exposed to ARF with Volumetric Targeting > Volumetric Passive Targeting	80%	100%	60%
% of Slices Exposed to ARF with Mean Targeting > Passive Targeting	65%	91%	51%

intensities, was achieved using ARF pulses with a 13 kPa amplitude and a cRGD targeted bubble (nomenclature: "RF-13/cRGD$^+$"). In all of the animals that were tested, the volumetric targeted intensity was greater using RF-13/cRGD$^+$ than with passive targeting (nomenclature: "RF-0/cRGD$^+$"). Notably, there was improved microbubble retention in 91% of all 2-D image slices of RF-13/cRGD$^+$ data collected when compared to the RF-0/cRGD$^+$ studies (Table 10.1). In the remaining 9% of 2-D image slices (in which the passive targeting images were brighter than the RF-13/cRGD$^+$ images), there was less than 1 dB difference between the mean pixel intensity of RF-13/cRGD$^+$ data as compared to the RF-0/cRGD$^+$ case. Also of note, of the 9% of 2-D image slices in which RF-13/cRGD$^+$ was not as bright as the passive targeting run, 80% of these were within the same animal.

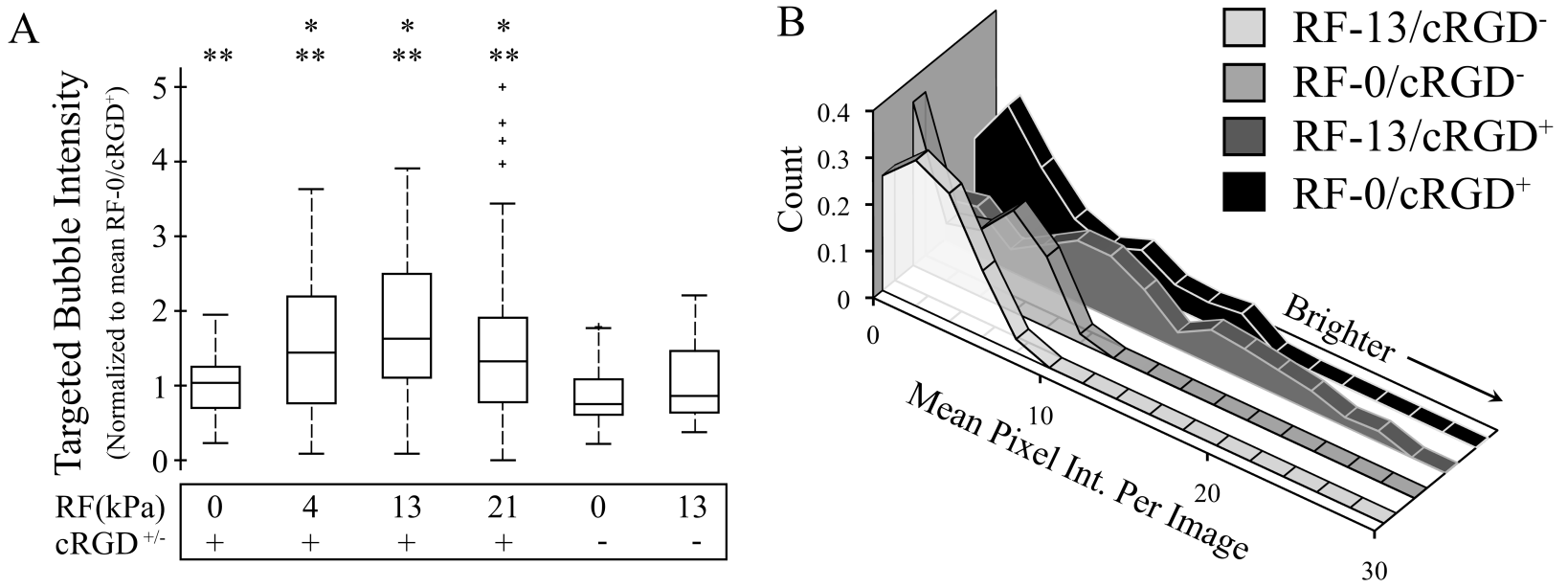

Figure 10.6: A: A box and whiskers plot displaying the distribution of all mean intensities within baseline-subtracted targeted bubble images collected in this study. Data is normalized to the mean pixel intensity within the 0 kPa /cRGD$^+$ dataset collected in each study. Asterisks indicate a statistically significant increase in targeting ($p < 0.05$) over: * - the RF-0/cRGD$^+$ data, ** - the RF-0/cRGD$^-$ data. B: A comparison of the histograms of pixel intensities for all image slices used in studies using control and targeted microbubbles with and without radiation force at 13 kPa. These histograms are area-normalized (not intensity normalized), and show a larger proportion of bright pixel values when targeted bubbles are used, and even more when radiation force is used with targeted bubbles.

The increase in average retained contrast intensity across all animals was 77.8% higher with the RF-13/cRGD$^+$ over the RF-0/cRGD$^+$ case: 11.40 ± 6.97, compared to 6.41 ± 4.81 respectively. The values represent baseline-subtracted pixel intensities, and thus the units are dB. The error in these values is the standard deviation of the baseline-subtracted pixel intensities. Similarly, both the RF-4 (8.80 ± 7.88) and RF-20 (8.78 ± 6.96) settings produced a statistically significant increase in targeting of cRGD$^+$ bubbles relative to the RF-0/cRGD$^+$ case. Of note, the RF-13/cRGD$^-$ case suggested a slight increase in non-specific microbubble adhesion relative to the RF-0/cRGD$^-$ case; however, differences were not significant ($p = 0.15$). The histograms created from the amalgamation of all unnormalized data show that, in general, the adherent bubble concentration was higher for both ARF-enhanced and passive targeting studies (Figure 10.6B) compared to non-targeted controls. Furthermore, these histograms show that the RF-13/cRGD$^+$ studies produced the greatest number of enhanced pixels. Figure 10.7 illustrates an example of ARF-enhanced targeted imaging and conventional passive targeting. In this image, the tumor volume is presented with a conically-stratified hinged cutaway, wherein elliptical regions of interest were drawn such that they did not follow the tumor border but instead cut into the interior of the tumor. This allows for microbubble targeting from within the tumor margins to be visualized on the rendered 3-D surface, which we found was useful in visualizing 3-D molecular imaging data.

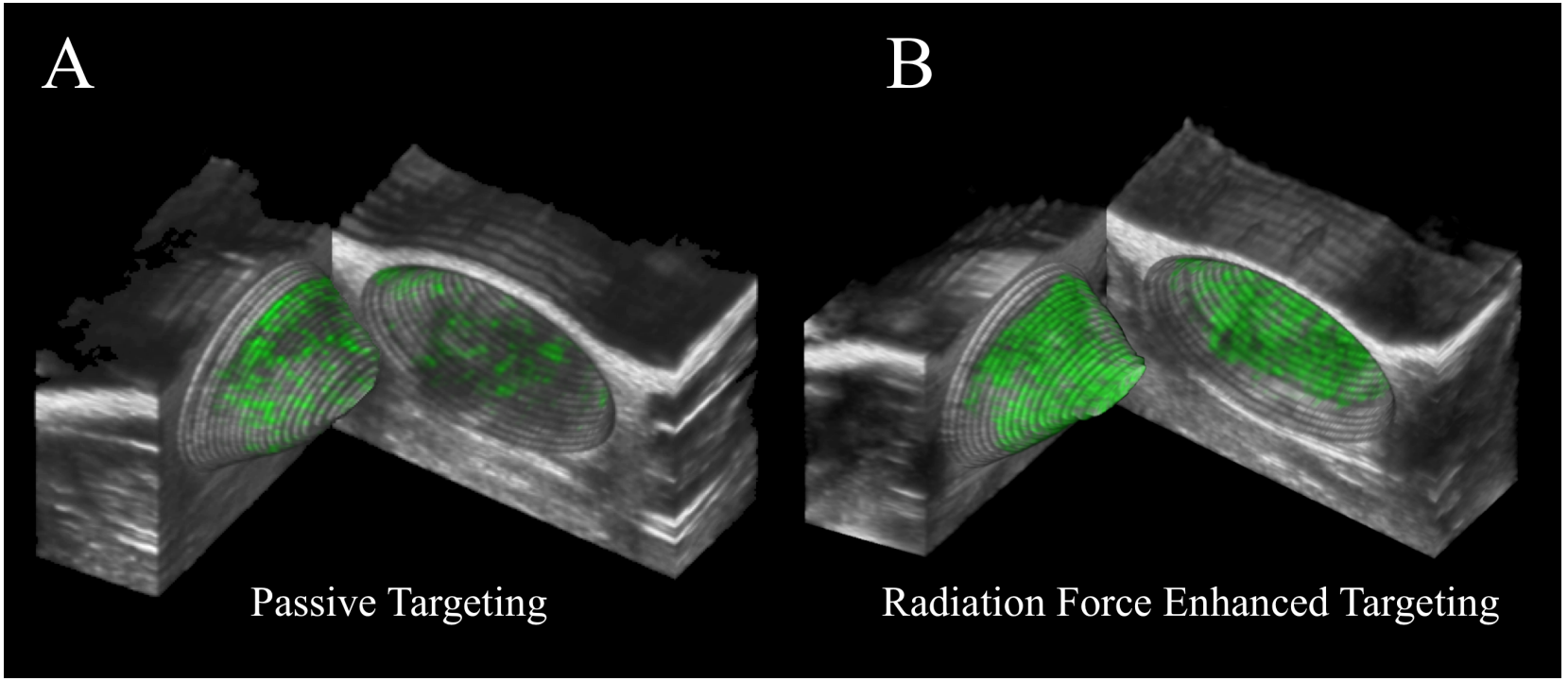

Figure 10.7: A side-by-side comparison of two 3-D conically-stratified hinged cutaway images. B-mode images (grayscale) are registered to the corresponding CPS images acquired 10 minutes after contrast injection (green). In both of these images, the same dose of targeted microbubbles was administered to the same animal. Radiation force was not applied in image A, and was applied at 13 kPa in image B. The imaging field of view was 1.2 cm x 1.1 cm x 0.08 cm.

10.4 Discussion and Conclusion

10.4.1 Optimizing Radiation Force: *In Vitro* Predictions and *In Vivo* Results

Using ARF to facilitate molecular targeting of microbubbles to integrins expressed on diseased endothelium is an intuitive approach to improving the sensitivity of this diagnostic imaging methodology, but its application is non-trivial. Our *in vitro* studies allowed us to observe the behavior of microbubbles exposed to ARF pulses both during their translation and after making contact with the wall of a vessel-mimicking phantom. These analyses allowed us to tune parameters to predict the optimal settings for *in vivo* studies.

The calculation of the CEF demonstrated that because of the effects of tissue attenuation, there is no single setting for ARF amplitude that is universally appropriate to increase molecular imaging sensitivity at all tissue depths. Our CEF model predicted that ARF pulses with 13 kPa pressure amplitude to be the most effective of the three amplitudes tested in our *in vivo* study. The model suggestions were supported by the *in vivo* study, as the 13 kPa pulses had the highest microbubble targeting efficiency. The CEF predictions for the two other pressure amplitudes tested (4 and 20 kPa) were similar, which was also reflected in the *in vivo* data, as these pressures resulted in similar increases in microbubble targeting, and were both less effective than the 13 kPa ARF pulses. This CEF model assumed a constant attenuation of 0.6 $\frac{\mathrm{Np}}{\mathrm{cm}}$ throughout the depth of the tumor, which did not take into account the attenuation provided by the scatter of microbubbles in the tissue. Moreover, our method of tuning ARF pressure via the CEF assumes that a uniform density of integrin expression exists throughout the entire tumor volume. While this is likely not true in the highly heterogeneous microenvironment of tumors, unless the heterogeneity is known, the best strategy for improving molecular targeting is one which maximizes the probability of microbubble

bond formation at all locations within the tumor.

Our *in vivo* studies demonstrated an average increase in microbubble targeting of nearly 80% relative to traditional passive targeting studies. It is important to emphasize that 91% of all the 2-D image slices within the ARF-enhanced datasets exhibited greater microbubble targeting than the corresponding image frames taken from the passive targeting data. Of the remaining slices that exhibited greater microbubble adhesion in the passive targeting case, most were outliers found in a single animal that showed poor microbubble targeting in all experiments. This, along with the rest of the data summarized in Table 10.1, makes a compelling argument that ARF can improve the diagnostic utility of USMI studies.

In control microbubble experiments, non-specific targeting was observed. In some animals, the targeting with control microbubbles was similar to the targeting with targeted microbubbles, which is a detriment to the technique. The ultimate goal of molecular imaging is to determine the degree to which biomarkers are expressed by the target tissue. Therefore, it is essential that targeted microbubbles adhere in quantities that produce backscattered intensities in greater magnitude than the signal intensities from non-specific targeting of control microbubbles. Given this requirement, and the significant increases in microbubble adhesion with ARF, the application of ARF to improve targeting *in vivo* is of great value for applications in which there is substantial non-specific targeting.

10.4.2 Comparing This *In Vivo* Study To Previous Work

A persistent question surrounding the usefulness and applicability of ARF to *in vivo* molecular imaging studies is whether pushing populations of bubbles away from the proximal walls of vessels could actually be detrimental to maximizing the number of microbubble-integrin bonds. While microbubble targeting on proximal vessel walls

is likely negligible during the application of ARF pulses, after the pulses stop, these binding sites are free to be populated by the passive targeting of bubbles circulating through the vasculature. Regardless, based on our *in vitro* observations, the amount of increased bubble adhesion due to ARF substantially outweighs any loss of targeting on the proximal vessel walls. Another concern is whether acoustically forcing bubbles into vessel walls will cause an increase in non-specific adhesion and thereby increase the rate of false-positive diagnoses. This was not observed in our study, as there was no significant difference in targeting efficiency between the control bubble with ARF application compared to the control bubble with no ARF (Figure 10.6). However, we suggest that this would need to be re-evaluated for different adhesion ligands and tumor types.

Previous *in vitro* work studying the increase in targeting efficiency of ARF-enhanced studies relative to passive targeted bubbles adhesion has demonstrated a large dependence on microbubble concentration. There was approximately 3 times more adhesion in passive targeting experiments without an appreciable difference in ARF efficiency when the bubble concentration was increased from 2.5 x 10^6 to 25 x 10^6 $\frac{\#}{\text{mL}}$ [47]. This suggests that a larger difference in microbubble targeting effectiveness will be apparent if a lower concentration of microbubbles is used, though these studies have yet to be performed *in vivo*. Additionally, since the magnitude of radiation force is highest at the resonant frequency of a microbubble [131], the frequency of our radiation force pulses could have been a source of reduction in expected targeting effectiveness. We were pulsing at 7 MHz, which was slightly higher than the resonance frequency of our bubbles ($\sim$6 MHz, as calculated using the method described in [36]). Finally, secondary radiation force is known to create aggregates of multiple microbubbles after contacting vessel walls [46; 47; 141] (Figure 10.4B). If these aggregates form lasting bonds with integrin targets, they will contribute to the image signal intensity differently than a

single bubble would. This could have contributed to the variability observed in our *in vivo* studies.

In prior *in vivo* molecular imaging studies implementing ARF, Rychak *et al.* (2007) optically observed a > 20 fold increase in microbubble adhesion *in vivo* using intravital microscopy in both the femoral artery and vein of a mouse model for inflammation; although, this study relied on optically counting microbubbles through invasive intravital microscopy to quantify retention rather than using US imaging. Thus, a direct correlation between Rychak's data and the data presented herein is not possible. Gessner *et al.* (2009) previously demonstrated the administration of ARF and acoustic detection of the targeted bubbles using a prototype high-resolution probe and custom pulse sequences, with an average microbubble targeting improvement of 13 dB across all image slices when ARF was used compared to passive targeting. There were many differences between that study and this one, including the ARF parameters, and the imaging techniques' contrast sensitivities, which could account for the differences between the reported increase in sensitivity facilitated by radiation force in that paper relative to this one.

10.4.3 Limitations and Future Directions

It was beyond the scope of the *in vitro* study of observations of contrast agents interacting with the tube wall to quantify the motion and trajectories of the bubbles after contacting the tube wall. This was because the aggregates of multiple contrast agents continually formed clusters of bubbles in an erratic fashion due to secondary radiation forces, and thus made tracking individual contrast agents very difficult. The lack of this analysis notwithstanding, the standard deviation projections seen in Figure 10.4B demonstrate this effect and suggest that higher pressures would reduce the likelihood of lasting ligand-integrin bond formations. A more thorough analysis of this lateral

motion would help define P_o more accurately than our coarse ability to adjust the amplitude of the ARF pulses permitted.

As mentioned previously, the best strategy for improving targeting is one that maximizes the probability of microbubble adhesion throughout the tumor. Due to attenuation effects, it was not possible in our *in vivo* studies to apply ARF uniformly at all axial depths. One potential strategy to apply a more homogeneous ARF profile to multiple depths within tissue (not examined in these studies) would be to sweep through multiple pressures at each spatial location. If at first a high pressure is used, it facilitates microbubble targeting deeper into tissue (due to attenuation) while simultaneously over-pushing at shallow depths. If the pressure is steadily reduced, microbubbles at shallower depths will be pushed at a more appropriate pressure without negatively affecting the targeted bubbles deeper in the tissue, since the pressure at these depths will have been reduced and thus the secondary radiation force effects minimized. Of note, over-pushing targeted contrast agents only would be detrimental to molecular imaging studies in which the lasting integrity of the microbubble's bond is critical, whereas this is less important for therapeutic delivery studies in which the ultimate goal is rapid and efficient localization and release of a microbubble's payload.

The time window over which radiation force is applied may also affect the increase in microbubble adhesion; if radiation force is administered continuously over several minutes as microbubbles circulate through the animal, more bubbles will be pushed against the endothelium, though this increased microbubble traffic at the vessel wall could be counterproductive if it causes previously adherent agents to become dislodged.

The experiments performed in this manuscript were done on a widely used clinical scanner without any additional customization of the software or pulse sequences; although, we suggest that improved results would be obtained if dedicated optimized pulse sequencing and beam focusing/defocusing were available. Our approach did rely

on mechanical scanning of the transducer to uniformly apply ARF pulses from the 1-D linear array across the volume of tumor tissue; however, this would be unnecessary if a 2-D matrix array probe were available for high-resolution contrast imaging.

The studies presented herein provide validation of ARF applied with a clinical US system as a mechanism to enhance molecular imaging. In all *in vivo* studies, the average targeted microbubble signal throughout the 3-D tumor volume was greater when using ARF (at 13 kPa) when compared with passive targeting studies. Our 3-D imaging results demonstrate an improvement in sensitivity of 77.8% over conventional passive molecular imaging without a corresponding loss in specificity. Furthermore, experiments suggest that for volumetric administration of radiation force, there exists an optimal pressure for ARM-enhanced targeting, which is a compromise between efficient bubble translation and adhesion-disruptive secondary radiation force and lateral translation effects.

CHAPTER 11

USMI with Buried-Ligand Microbubbles

11.1 Introduction

The current microbubble architecture, with exposed surface targeting ligands, presents the hazard of non-specific interactions with plasma components that may lead to non-specific adhesion. One additional concern for clinical application of exposed-ligand microbubbles is complement activation, which may affect the targeting specificity of the ligand, stimulate an undesired immune response, change the underlying physiology and, in more severe cases, result in complement activation-related pseudo-allergy (CARPA) [142]. Thus, it is necessary to avoid complement fixation and activation by the targeting ligand on the microbubble surface.

To address the problems of immunogenicity and specificity in USMI, we engineered microbubbles with a BLA in which a hydrated PEG brush on the microbubble surface consists of two tiers: the ligand is attached to a short PEG tether surrounded by longer PEG chains that forms an overbrush (Figure 11.1) [51; 75]. The brush self-assembles as the underlying lipids adsorbs and condenses into a monomolecular encapsulation during microbubble fabrication. Shielding of the ligand by the methoxy-terminated

PEG overbrush was shown to inhibit complement activation and increase circulation persistence in non-tumor bearing rodents [51; 52; 50; 143].

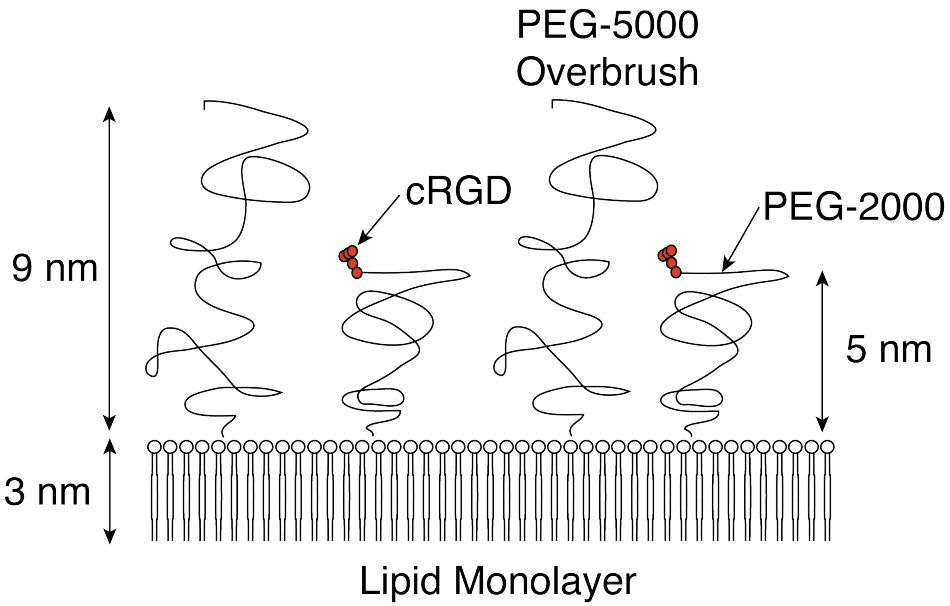

Figure 11.1: The MCA is approximately 4.0 μm in diameter filled with decafluorobutane gas and coated with a lipid monolayer shell. A side view of the lipid shell shows the buried-ligand architecture, which comprises a shorter (2000 Da) PEG tethered to cRGD peptide surrounded by a longer (5000 Da) PEG overbrush [51; 75; 52; 50; 143].

The buried-ligand architecture is designed to be activated by ARF, a phenomenon in which momentum is transmitted from the acoustic wave to the microbubble and which is amplified near microbubble resonance [51; 52]. The combination of a normal force pressing the microbubble against the endothelium and lateral surface dilatation and contraction via oscillation, allows the ligand and receptor molecules to penetrate the longer PEG overbrush for binding. In previous *in vitro* studies, we found that microbubbles with the BLA can be targeted to cells with the application of ARF [52]. However, prior studies have not demonstrated *in vivo* USMI with buried-ligand microbubbles.

To test the functionality of the BLA, we elected to target the vasculature with the cRGD peptide, which has been shown to target tumor vasculature through binding to

$\alpha_v\beta_3$ integrin that is over-expressed in tumor vasculature [22]. While cRGD may also bind to other integrins of the β_3 family, such as platelet integrin $\alpha_{IIb}\beta_3$, the specific activation of the buried-ligand microbubbles through ARF of tumor tissues is expected to limit non-specific background. Comparison of *in vivo* results from exposed-ligand and buried-ligand microbubbles allowed an assessment of this approach for molecular imaging.

11.2 Materials and Methods

11.2.1 Microbubble Contrast Agents

All exposed-ligand microbubbles used in our studies were formulated in a 2 $\frac{mg}{mL}$ lipid solution as previously described in 4.3.3, 4.3.4, and 4.3.6. Briefly, targeted agents were fitted with a cRGD peptide known to bind to $\alpha_v\beta_3$, an integrin over-expressed on angiogenic endothelium [22; 38]. Likewise, non-targeted exposed-ligand microbubbles were produced with a similar lipid formulation, but with a cRAD peptide (control) as described in 4.3.2, 4.3.4, and 4.3.6. Both targeted and non-targeted microbubbles had a mean diameter around 4.0 μm.

All buried-ligand microbubbles used in our studies were formulated similar to the exposed-ligand protocol described in 4.3.3, 4.3.4, and 4.3.6 with the exception that the untethered - DSPE - PEG2000 lipid was replaced with a longer DSPE - PEG5000 overbrush.

11.2.2 Animals and Tumor Models

A total of 8 Fischer 344 rats of similar sizes ($\sim$125 g) were used for all *in vivo* studies. Tumors were implanted and animals were prepared for imaging as described in 5.3. For each injection, the appropriate volume of stock solution was added to the catheter via a micropipette tip and flushed with 100 μL of sterile saline such that a contrast agent

dose of 5 x 10^6 microbubbles was administered consistently with each injection.

11.2.3 Clinical Imaging System

11.2.4 Imaging System

The 3-D US imaging system along with the parameters used to acquire all images in this chapter are as described in 5.2.1, 5.2.2 and 5.2.3. Within all imaging data sets, the CPS gain (−12 dB) and transmit power (MI: 0.18) were kept constant and the transducer was stepped elevationally at 400 μm increments across the tumor.

For volumetric radiation force administration and imaging, the transducer was swept in the elevational direction by a computer controlled motion stage interfaced through LabView to a desktop computer as previously described in 5.2.4. The amplitude of the ARF pulses was set to be 13 kPa, which provided the best ARF enhancement in a previous study [102].

11.2.5 Contrast Agent Persistence Protocol

Microbubble clearance from the circulatory system was measured *in vivo* by observing the length of time that each type of microbubble persisted in the tumor vasculature. Thus, prior to obtaining molecular imaging data, microbubble persistence times in the tumor vasculature were obtained at the cross-sectional center of the tumor using only one 2-D image plane. Data were collected and analyzed using the procedure outlined in 6.1.1. We used Matlab's two-sided Student's t-test to assess the statistical significance of our comparison between microbubbles with an exposed ligand to microbubbles with a buried ligand. Significance between two different distributions were considered at a value of $p < 0.05$.

11.2.6 Molecular Imaging Protocol

Before the bolus injection, the system was set to the ARF parameters described in 5.2.4. Then, the transducer was swept at a constant speed of 1 $\frac{\text{mm}}{\text{s}}$ across the tumor volume after contrast agents were administered to the animal, for a total of 10 passes after the injection. Then, molecular imaging data was obtained and analyzed after freely circulating microbubbles had visibly cleared the animal's system as described in 6.2. Again, we used Matlab's two-sided Student's t-test to assess the statistical significance of our distributions. Significance between two different distributions were considered at a value of $p < 0.05$.

11.3 Results

11.3.1 Contrast Agent Persistence *In Vivo*

After intravenous administration of MCAs, the mononuclear phagocyte system rapidly works to remove these foreign particles from the bloodstream [144]. It is hypothesized that microbubbles with targeting ligands may trigger complement activation in this system, thus decreasing the persistence time relative to microbubbles without a targeting ligand [50]. The goal of our first experiment was to analyze the persistence times of microbubbles with and without targeting ligands to validate our hypothesis.

We first investigated whether burying cRGD by the PEG overbrush can increase the circulation persistence of the microbubbles in tumor-bearing rats with an intact complement system. The persistence of US contrast enhancement was measured as a function of time in the tumor midsection for buried-ligand cRGD microbubbles, and the results were compared to those for microbubbles carrying exposed cRGD (i.e., not buried by PEG) microbubbles. Representative time-intensity curves and their *in vivo* images are provided for reference (Figure 11.2).

We observed that the US contrast half-life in the tumor was over threefold higher

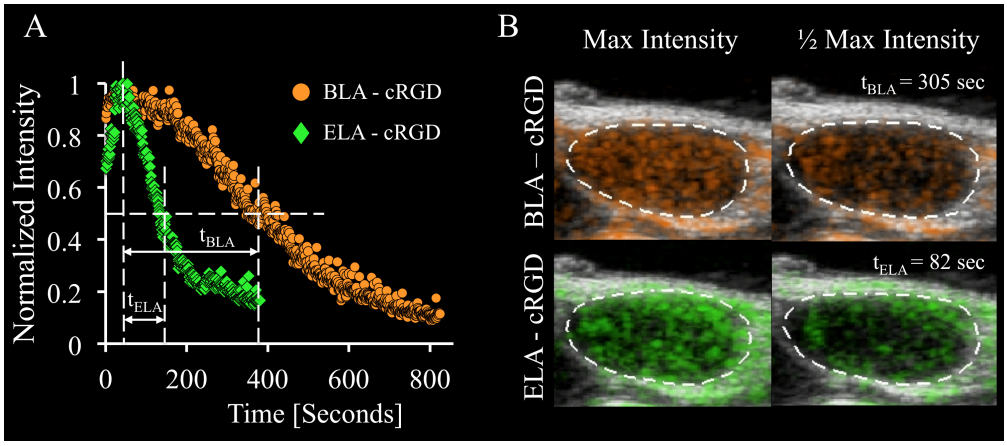

Figure 11.2: A: Representative normalized time-intensity curves showing maximum and half-amplitudes. B: Representative US images showing a 2-D image plane with color contrast from microbubble signals overlay onto grayscale b-mode images.

(96 ± 27 s vs. 298 ± 76 s, $p < 0.001$) for the pooled buried-ligand microbubbles when compared to the pooled exposed ligand microbubble persistence times. Moreover, the individual persistence times from each of the buried-ligand microbubble groups (cRGD and cRAD) were significantly different from each of the exposed-ligand microbubble types (BLA-cRAD: 273 ± 83, BLA-cRGD: 336 ± 48 vs. ELA-cRAD: 87 ± 21, ELA-cRGD: 105 ± 31, $p < 0.001$) (Figure 11.3). The microbubbles were of similar size and concentration, and therefore the increase in circulation persistence indicated a functional decrease in non-specific interactions between the ligand and mononuclear phagocyte system.

11.3.2 Molecular Imaging *In Vivo*

The overall goal of our study was to reduce the level of complement activation in molecular imaging experiments by shielding the targeting ligand from the immune system using a PEG overbrush. Consequently, it was essential that our buried-ligand architecture, not only reduces complement activation, but also behaves in a manner that is suitable for molecular imaging experiments. Thus, buried-ligand microbubbles targeted

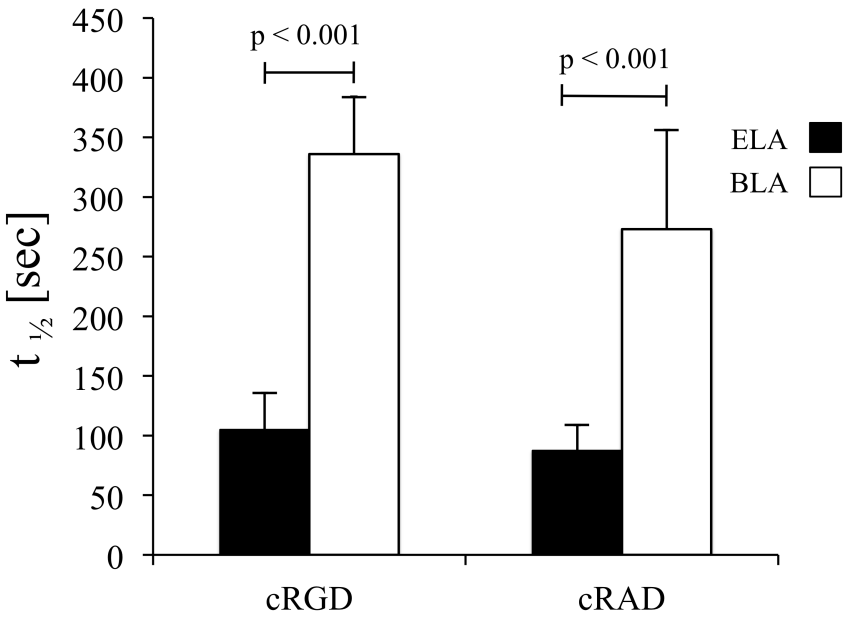

Figure 11.3: Analysis of total US contrast persistence in the tumor volume without ARF showed that buried-ligand (BLA) microbubbles circulated approximately three-fold longer than exposed-ligand (ELA) microbubbles (cRGD, $p < 0.001$, $N \geq 5$, cRAD, $p < 0.001$, $N \geq 5$) indicating avoidance of the mononuclear phagocyte system by the buried-ligand architecture.

to $\alpha_v\beta_3$ (cRGD) were evaluated *in vivo* relative to non-targeted (cRAD) buried-ligand microbubbles with and without radiation force. The contrast signal from targeted microbubbles was registered to the tumor anatomy by overlaying the bound-microbubble signal in green to the background grayscale b-mode image (Figure 11.4). This method produced a noticeable increase in targeting for cRGD-microbubbles exposed to ARF in comparison to controls. To our knowledge, this is the first time that US has been used to activate targeting specificity for *in vivo* molecular imaging. All imaging procedures were performed using a commercially available clinical US system.

In addition, the effect of the application of ARF enhancement was evaluated. This parameter was determined by taking the ratio of the contrast-to-tissue ratios for tumors with and without exposure to ARF for a given microbubble architecture, and therefore

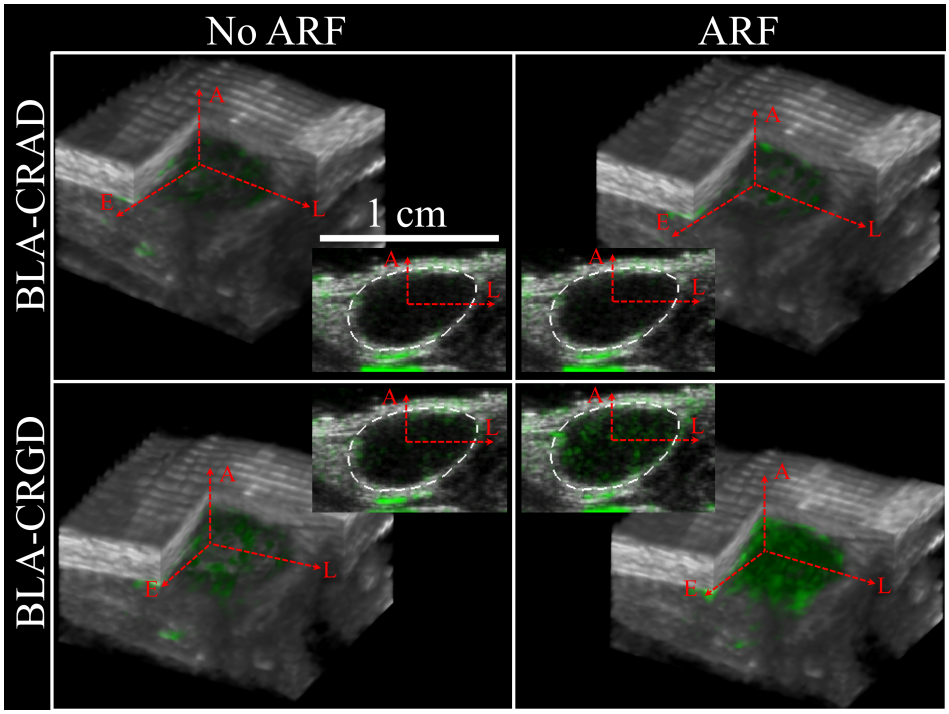

Figure 11.4: Images show the extent of buried-ligand microbubble binding (green contrast) within the tumor and surrounding tissue.

are normalized by circulation persistence to give an accurate value for stimulus responsiveness. Exposure to ARF more than doubled the volumetric targeted intensity for cRGD-microbubbles (BLA-cRGD-ARF: 3.7 ± 1.5 vs. BLA-cRGD-No ARF: 1.6 ± 0.6, $p < 0.01$) (Figure 11.5). No such increase was observed for control cRAD-microbubbles in the same animals (BLA-cRAD-ARF: 1.3 ± 0.8 vs. BLA-cRAD-No ARF: 1.5 ± 1.0, $p > 0.05$). A comparison of the ARF enhancement between brush architectures showed a twofold increase for the buried ligand compared to the exposed ligand (BLA-cRGD: 2.3 ± 0.7 vs. ELA-cRGD: 1.2 ± 0.3 , $p < 0.01$) (Figure 11.6).

11.4 Discussion and Conclusion

Application of ARF with buried-ligand microbubbles was used for USMI of tumor neovasculature *in vivo*. Our data show that the PEG overbrush had the necessary

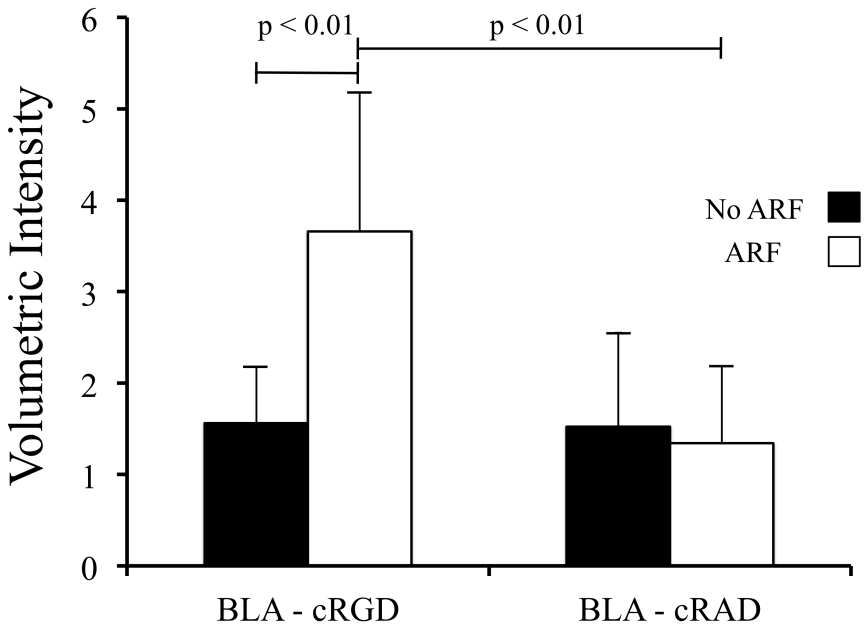

Figure 11.5: Analysis of the volumetric average contrast intensity indicated a significant increase in cRGD-microbubble adhesion to neovasculature when exposed to ARF, showing that US was effective in triggering ligand-receptor mediated adhesion ($N \geq 7$). Control cRAD-microbubbles experienced significantly less adhesion than cRGD-microbubbles when stimulated with ARF, showing specificity ($N \geq 5$).

barrier properties to avoid competitive interactions between the ligand and plasma components en route to the tumor. Our data also show that the buried-ligand surface architecture is sufficiently dynamic to achieve firm adhesion to the tumor endothelium, even with no applied radiation force.

This molecular imaging method was able to detect angiogenic tumor regions with high sensitivity. The methodology allowed on-demand spatiotemporal control over microbubble adhesion, providing enhanced specificity to the targeted tumor tissue. Molecular specificity for $\alpha_v\beta_3$ integrin was shown by comparing the targeted contrast signal from microbubbles expressing the adhesion ligand versus the non-targeted control, in the same tumors. Finally, the utility of the technique was shown through the use of a widely available clinical scanner.

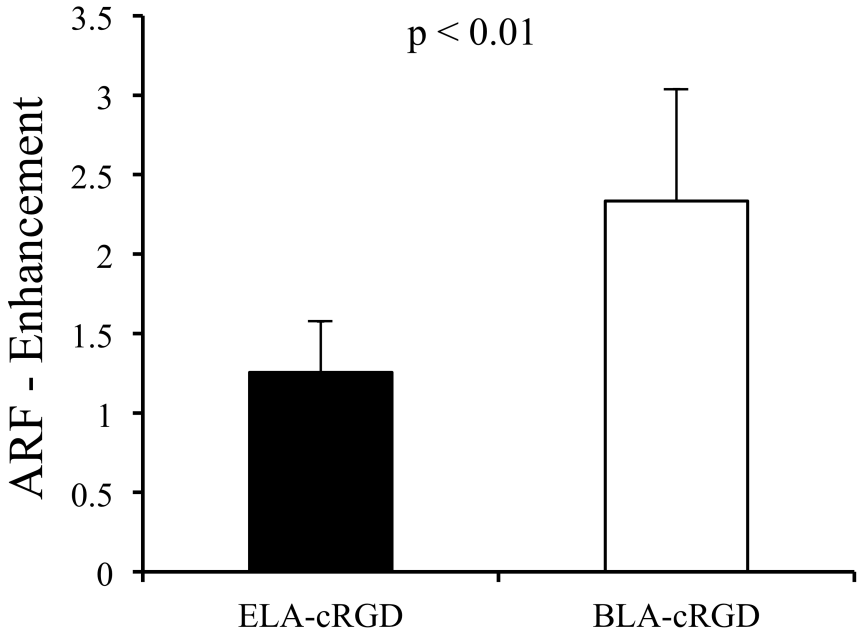

Figure 11.6: Analysis of ARF enhancement for ELA vs. BLA (N $\geq$ 7). Enhancement was significantly greater for the buried-ligand architecture, showing that these microbubbles provide enhanced specificity to spatiotemporal targeting through application of radiation force.

This work paves the way for a new generation of US imaging systems that provide greater target sensitivity and adaptive user control for increased safety and accuracy. While these studies are encouraging, we note that the FSA tumor model tested here is known to exhibit active angiogenesis over the tumor volume. This allowed quantification through volumetric averaging of the contrast signal to produce a sensitive and specific readout of tumor neovasculature. Clinical translation, however, would require further testing of the methodology in tumors ranging in size, shape and tissue depth and exhibiting variable degrees of angiogenesis. Additionally, clinical translation will require additional studies to assess diagnosis of tumor physiology in large-animal models exhibiting genetically derived and spontaneous tumors. The *in vivo* demonstration of the technique using a clinical scanner provides strong rationale to pursue such studies.

CHAPTER 12

Evaluating Techniques for Response to Therapy

12.1 Introduction

12.1.1 Aurora-A Kinase Inhibition

Aurora kinase, a type of serine/threonine kinase, is part of a family of enzymes related to cell proliferation [145]. In the mid 1990's, it was discovered that aurora kinase defects led to mitotic abnormalities [146]. Disruption of the functional process involving aurora kinase can result in mitotic spindle apparatus deficiencies, chromosome segregation abnormalities and eventually apoptosis [147]. The discovery that aurora kinases are highly expressed in many tumor cell lines, including pancreatic adenocarcinoma [148], has led to the development of a variety of aurora kinase inhibitors, such as MLN8237, for tumor research [149; 150; 151]. MLN8237, an orally administered aurora-A kinase inhibitor is currently in clinical trials for patients with advanced solid tumors; emerging data suggests that it may be active in some adult solid tumors [152; 153].

 Portions reprinted, with permission, from JE Streeter, SG Herrera-Loeza, NF Neel, JJ Yeh and PA Dayton. "A Comparative Evaluation of Ultrasound Molecular Imaging, Perfusion Imaging, and Volume Measurements in Evaluating Response to Therapy in Patient-Derived Xenografts" TCRT, Jan 25, 2013. Epub ahead of print.

12.1.2 Response to therapy

Anatomic measures of solid tumors have been the "gold standard" by which therapy effectiveness is evaluated [7]. The disadvantage to using size measurements to analyze response is that although the tumor volume may not have changed significantly, there may be considerable changes in tumor activity and necrosis [154; 155]. In many instances, there may be a significant delay or lag time between the time of treatment and any change in tumor size [7]. Thus, new early imaging response techniques are sought after to non-invasively predict treatment response both clinically and pre-clinically. USMI and DCE-PI are two attractive alternatives.

12.1.3 Ultrasonic Molecular Imaging

MCAs are inherently blood pool agents, thus USMI is restricted to analysis of biological events located within the vascular system. This particular characteristic makes this imaging modality an attractive non-invasive technique for the detection of molecular processes on vascular endothelial cells, and more specifically, tumor angiogenesis. Tumor angiogenesis is the formation of capillaries and new blood vessels from surrounding host tissue to provide sufficient oxygen supply and nutrients to the tumor [129]. As cancer cells proliferate, more oxygen and nutrients are needed for cell survival. Thus, at the onset of hypoxia after cell proliferation, tumors will assemble vasculature by releasing chemotactic signals to recruit endothelial precursor cells [129]. Presumably, any impairment of tumor growth and apoptosis has a downstream effect on angiogenesis and therefore angiogenic integrins (VEGFR-2, $\alpha_{\mathrm{v}}\beta_3$, etc.) expressed on endothelial cells in proximity to the tumor [156; 157].

In recent years, targeted agents have been successfully used for non-invasive 2-D *in vivo* imaging of tumor angiogenesis [45; 44; 158; 43; 78], and more recently USMI has been demonstrated in 3-D [81; 38]. This breakthrough has allowed USMI to be

used for quantifying the efficacy of anti-angiogenic drugs such as bevacizumab (VEGF inhibitor) in murine models [43; 159; 54].

12.1.4 Dynamic Contrast-Enhanced Perfusion Imaging

As previously mentioned (6.1.2), ultrasound DCE-PI is a method that is used to non-invasively monitor the blood flow in both large vessels and in the capillary microcirculation using non-targeted MCAs. This technique uses a short high-intensity pulse of US that causes rapid destruction of MCAs in the interrogated region. This clearance pulse is immediately followed by a low-intensity contrast specific signal that does not fracture the microbubbles, but instead, allows for the pixel-by-pixel observation of blood flow rates as the MCAs enter back into the tissue [71; 96]. Accordingly, changes in contrast enhancement over time can provide information about tissue perfusion. This method has previously been utilized to assess perfusion in the myocardium, kidney, and other tissues [71; 96; 97]. Furthermore, it is hypothesized that tissue perfusion correlates to tumor micro vessel density (MVD) [160; 161], a known prognostic factor in many cancer types [162; 163], which has been the motivation for the development of this technique in cancer assessment. Thus, it is proposed that *in vivo* measures using DCE-PI may also predict therapeutic response to agents that target and disrupt the tumor microvasculature.

It is unknown as to what method provides the best opportunity for successful pre-clinical evaluations, though our hypothesis predicts that USMI will provide information earlier in the treatment schedule than both DCE-PI and volume measurements. A recent study by Sirsi *et al.*, which aimed to evaluate both molecular imaging and perfusion imaging in a response to therapy study (VEGF Inhibition in SK-NEP-1 tumor line), supports our hypothesis [72]. Although this study was performed only with 2-D US, it

was highly significant in suggesting the potential of DCE-PI and USMI in the evaluation of a tumor's response to therapy. As recent studies have illustrated that 3-D US DCE-PI and 3-D USMI provide more accurate data regarding tissue blood flow and biomarker distribution than 2-D US, it is crucial to validate these technologies with volumetric imaging [81; 92; 73]. Thus, the aim of this study is to further validate the potential of USMI and DCE-PI in characterizing a tumor's response to therapy using 3-D US.

To test our hypothesis, we use USMI of angiogenesis and DCE-PI, both implemented in 3-D, to evaluate the effect of MLN8237 in patient-derived xenografts (PDX) of pancreatic cancer. PDX models of solid tumors have recently emerged as an innovative platform for the study of novel therapeutics for pancreatic cancer [164]. This model, where actual human tumors are grafted into mice, has been shown to be a better predictor of response to therapies in patients compared to traditional cell line xenografts [165]. We use a Siemens Sequoia US system (Mountain View, CA) in CPS mode for both perfusion and molecular imaging studies. In addition, with the use of a custom computer-controlled motion stage interfaced to the US system, we perform volumetric imaging by scanning the transducer elevationally at controlled intervals for a more robust evaluation of therapy effectiveness [81; 92]. Finally, we compare and elucidate the strength of each technique as a tool to identify responders and non-responders and to characterize how a tumor will respond to therapy over time in our PDX models.

12.2 Materials and Methods

12.2.1 Microbubble Contrast Agents

All microbubbles used in our studies were formulated as previously described in 4.3.3, 4.3.4, and 4.3.6. Briefly, targeted agents were fitted with a cRGD peptide known to bind

to $\alpha_v\beta_3$, an integrin over-expressed on angiogenic endothelium [22; 38]. Likewise, non-targeted microbubbles were produced with a similar lipid formulation, but without the targeting ligand as described in 4.3.2, 4.3.4, and 4.3.6. Both targeted and non-targeted bubbles were of a diameter size distribution centered at 3.9 μm. Unsorted non-targeted MCAs for perfusion imaging were created with a similar lipid formulation, but without the targeting ligand as described in 4.3.1, 4.3.4 and 4.3.5.

12.2.2 Animal Preparation and Contrast Administration

Two PDXs were chosen for this study, one with known response to MLN8237 (PDX-R) and one with no response (PDX-NR) to MLN8237 based on tumor size measurements and long term growth curves in previous studies. Each PDX (PDX-R and PDX-NR) was expanded into 14 nude mice (PDX-R and PDX-NR: Mean Volume $\sim 0.2 \pm 0.1$ cm^3). Seven mice were then assigned to drug treatment or vehicle groups for both USMI and DCE-PI experiments. During US imaging studies, animals were anesthetized with $\sim$2% inhaled isoflurane anesthesia with oxygen and their body temperature was maintained at 37°C through the use of a temperature-controlled heating pad. The area to be imaged was coupled to the US transducer using a water-based acoustic coupling gel devoid of any air bubbles. A 27-gauge catheter was inserted into the tail vein of the animal for the administration of MCAs. In all USMI experiments, bolus MCA injections of 50 μL (Concentration: 1 x 10^8 $\frac{\text{MCAs}}{\text{mL}}$ were delivered followed by an immediate flush of at least 50 μL sterile saline to clear any remaining MCAs from the catheter. For all DCE-PI experiments, non-targeted MCAs were continuously infused at a rate of 15 $\frac{\mu\text{L}}{\text{min}}$ using a PHD-2000 syringe pump (Harvard Apparatus - Holliston, MA).

12.2.3 Therapy

A total of 28 nude mice with (N=14 PDX-R and N=14 PDX-NR's) were used for USMI and DCE-PI experiments. Animals were either treated with 30 $\frac{\text{mg}}{\text{kg}}$ of MLN8237 or a

vehicle control daily by oral gavage each day over a 14-day period (treated group) while the remaining seven animals were provided a control vehicle (untreated group). For all experiments, USMI and DCE-PI data were taken on day 0, day 2, day 7, and day 14 during the treatment period in the same animals.

12.2.4 3-D Imaging Apparatus

The 3-D US imaging system along with the parameters used to acquire all images in this chapter are as described in 5.2.1, 5.2.2 and 5.2.3. Within all imaging data sets for molecular imaging and perfusion imaging studies, the CPS gain (-15 dB) and transmit power (MI: 0.18) were kept constant. For molecular imaging studies, the transducer was stepped elevationally every 400 μm for each image acquisition. However, for perfusion imaging studies, the transducer was stepped elevationally every 800 μm for each image acquisition due to the continuous infusion of microbubbles and the restriction on total volume injected into an animal.

12.2.5 Ultrasonic Molecular Imaging

The procedure for performing molecular imaging experiments and its subsequent analysis is described in 6.2. In this study, 15 minutes was determined to be an adequate length of time for this volume of freely circulating contrast agents to be cleared from an animal's system. The axial focus was positioned in the center of the tumor for each animal's readpoint. In addition, at each readpoint, the amount of microbubble targeting was normalized to the value obtained at baseline (day 0). Finally, we used Matlab's two-sided Student's t-test to assess the statistical significance of each group. Significance between two different distributions were considered at a value of $p < 0.05$.

12.2.6 Dynamic Contrast-Enhanced Perfusion Imaging

The DCE-PI imaging procedures and analysis for this set of studies are as previously described in 6.1.2. Perfusion imaging studies required approximately 10 minutes per animal. In addition, at each readpoint, the volumetric perfusion time was normalized to the value obtained at baseline (day 0). Significance between treated and untreated distributions was analyzed in Excel using a two-sided Student's t-test with unequal variance. Significance between distributions were considered at a value of $p < 0.05$.

12.2.7 Volume Measurements

Volume measurements for each tumor were obtained using the b-mode images acquired during USMI experiments in conjunction with the elevational step size. The measured volume at each readpoint was normalized to the value obtained at day 0 for comparison with other groups. Significance between treated and untreated distributions was analyzed in Excel using a two-sided Student's t-test with unequal variance. Significance between distributions were considered at a value of $p < 0.05$.

12.3 Results

12.3.1 Ultrasonic Molecular Imaging

PDX-R

Day 2 was the earliest readpoint at which there was a statistical difference between the untreated and treated populations when using USMI. On day 2, the mean volumetric targeted microbubble intensity in treated animals decreased by 51% from the baseline measurement at day 0 compared to an 20% increase in targeting for untreated animals (Untreated: 1.20 ± 0.53 vs. Treated: 0.49 ± 0.40; $p < 0.05$) (Figure 12.1A). On Day 7, the same trend was observed (Untreated: 0.70 ± 0.31 vs. Treated: 0.08 ± 0.09; $p < 0.05$), however, by day 14, there were no discernible differences between treated and

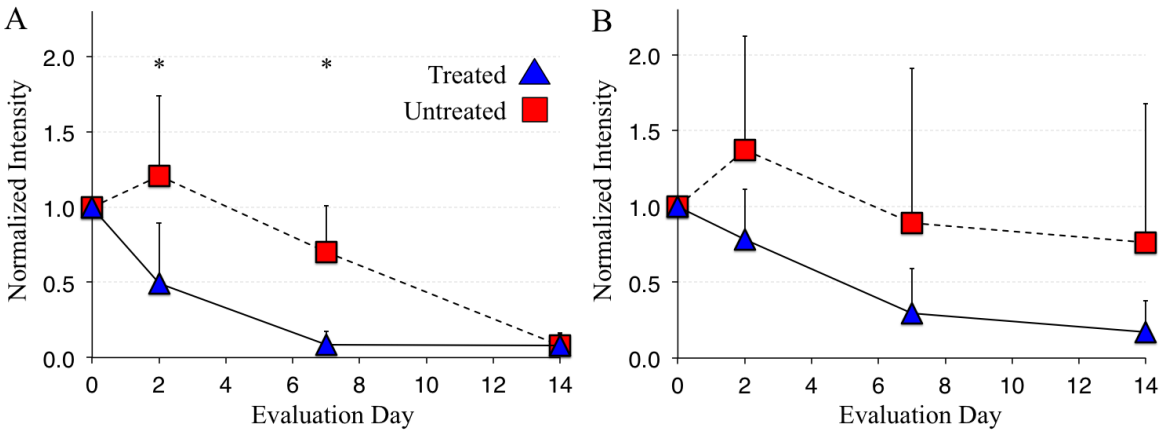

Figure 12.1: A) The percent change in volumetric targeted microbubble intensity for treated and untreated animals before and after therapy in a tumor type that responds to MLN8237 (N=7). B) The percent change in volumetric targeted microbubble intensity for treated and untreated animals before and after therapy in a tumor that does not respond to MLN8237 (N=7). *p < 0.05 for treated group relative to untreated group.

untreated populations.

Volumetric US images of a representative treated and a representative untreated PDX-R at baseline and 48 hours after treatment are illustrated in Figure 12.2. Axial and lateral axes are displayed on each 3-D image to orient the reader to the plane of the US transducer. In addition, 2-D cross sections, as registered by these section axes, illustrate the level of targeting at each day for the treated and untreated animal. The green color overlay illustrates the microbubble adherence to $\alpha_v\beta_3$ where the brightness is assumed to be correlated with the degree of molecular marker expression.

PDX-NR

In the PDX-NR cohort, there were no significant differences between treated and untreated populations at any readpoint in the 14-day study (Figure 12.1B). For clarity, Table 12.1 provides the volumetric USMI data for both the PDX-R and PDX-NR cohorts at all readpoints.

Table 12.1: Summary of the normalized volumetric USMI data for both treated and untreated animals in the PDX-R and PDX-NR cohorts. This data is supplementary to the plots in Figure 12.1.

		USMI			
		Day 0	Day 2	Day 7	Day 14
PDX-R	Treated	1.00 ± 0.0	0.49 ± 0.4	0.08 ± 0.1	0.08 ± 0.1
	Untreated	1.00 ± 0.0	1.20 ± 0.5	0.70 ± 0.3	0.08 ± 0.1
	p		0.03	0.01	1.00
PDX-NR	Treated	1.00 ± 0.0	0.77 ± 0.3	0.30 ± 0.3	0.17 ± 0.2
	Untreated	1.00 ± 0.0	1.37 ± 0.8	0.89 ± 1.0	0.76 ± 0.9
	p		0.08	0.16	0.15

12.3.2 Dynamic Contrast-Enhanced Perfusion Imaging

PDX-R

Day 14 was the earliest readpoint at which there was a statistical difference between the untreated and treated populations when using DCE-PI (Figure 12.3A). Of note, by day 2 there was an increase in mean volumetric TT20 values relative to day 0. While there was not a significant difference between treated and untreated populations at this readpoint, there was an increasing difference between treated and untreated population until day 14. As will be shown in the following subsection, this trend was not observed in the PDX-NR cohort. On day 14, the mean volumetric TT20 value increased by 31% from baseline in treated animals compared to a 6% decrease in the TT20 for untreated animals (Untreated: 0.94 ± 0.23 vs. Treated: 1.31 ± 0.22; $p < 0.05$).

PDX-NR

There were no significant differences between treated and untreated populations at any readpoint with the PDX-NR cohort (Figure 12.3B). Table 12.2 provides the raw volumetric DCE-PI values for each group at each readpoint.

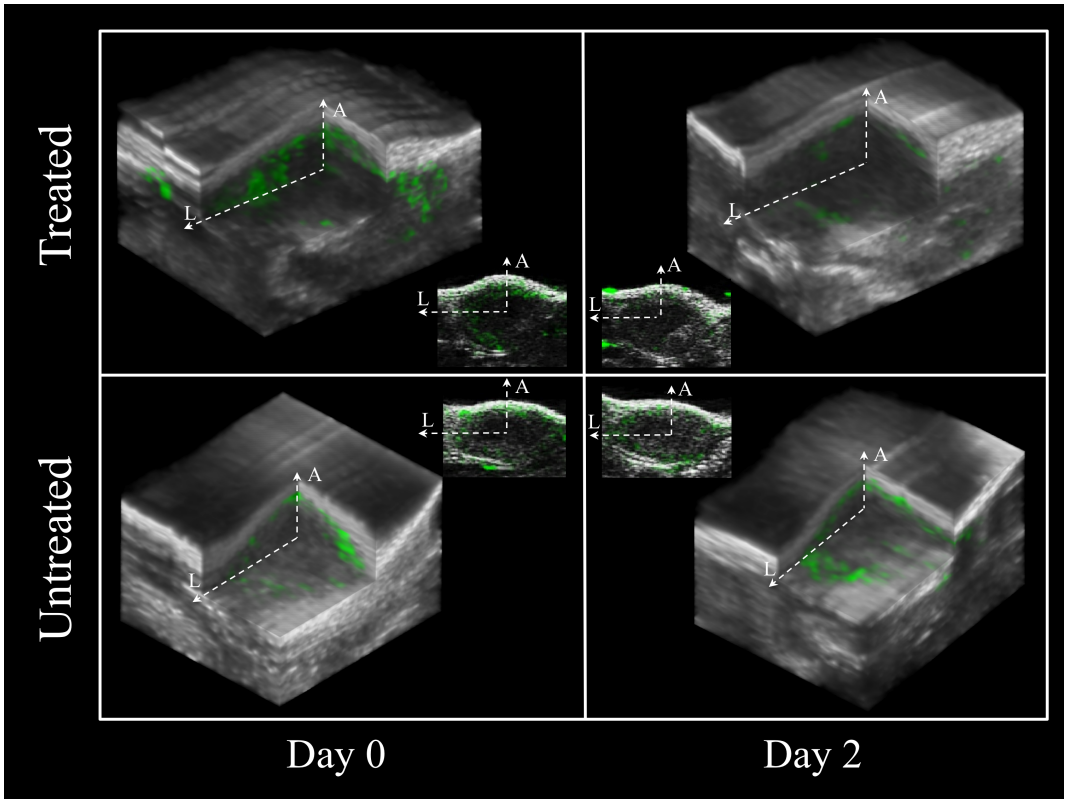

Figure 12.2: 3-D US images of a representative treated and a representative untreated tumor (PDX-R). A (axial) and L (lateral) axes are displayed to orient the reader to the traditional US b-mode image plane. 2-D cross sections as registered by these section axes are displayed in the central region of each panel. The green color overlay illustrates the microbubble adherence to $\alpha_v\beta_3$, an angiogenic biomarker. The brightness of the green image overlay is assumed to be correlated with the degree of molecular marker expression.

12.3.3 Volume Measurements

PDX-R

In the PDX-R cohort of animals, there was no statistical difference between treated and untreated populations when measuring the volume of the tumor at any readpoint (Figure 12.4). However, the difference in tumor volume between treated and untreated animals began to increase starting at day 7, as would be expected in this PDX-R, since it is characterized by known response to MLN8237 treatment. This trend was not

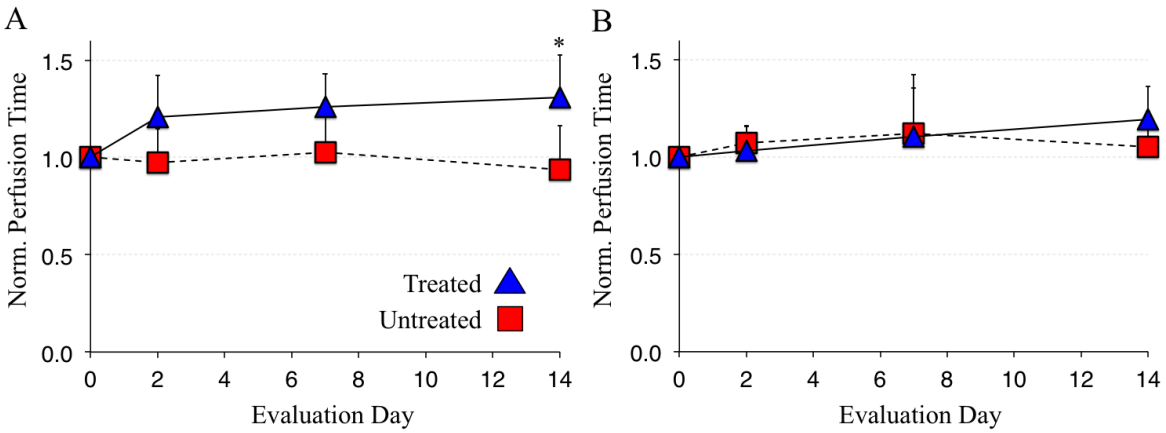

Figure 12.3: A) The average volumetric perfusion times before and after therapy for treated and untreated animals in a tumor type that responds to MLN8237 (N=7). B) The average volumetric perfusion times before and after therapy for treated and untreated animals in a tumor type that does not respond to MLN8237 (N=7). *p $<$ 0.05 for treated group as compared to untreated group.

observed in the PDX-NR cohort.

PDX-NR

As with the PDX-R group, there was no observed statistical difference between treated and untreated populations when measuring the volume of the tumor at any readpoint. Table 12.3 summarizes the volume data collected for the responder and non-responder groups.

12.4 Discussion and Conclusion

In this study, USMI of angiogenesis showed a statistical difference between treated and untreated PDX-R populations after 48 hours of treatment. In contrast, there was no significant difference between treated and untreated groups at the same readpoints in the PDX-NR cohort. Thus, our USMI study clearly illustrates the viability of the technique for monitoring the response to therapy and identifying and characterizing tumors as responders and non-responders in pre-clinical evaluations where comparison

Table 12.2: Summary of the normalized volumetric DCE-PI data for both treated and untreated animals in the PDX-R and PDX-NR cohorts. This data corresponds to the plots in Figure 12.3.

		DCE-PI			
		Day 0	Day 2	Day 7	Day 14
PDX-R	Treated	1.00 ± 0.0	1.21 ± 0.2	1.26 ± 0.2	1.31 ± 0.2
	Untreated	1.00 ± 0.0	0.98 ± 0.2	1.02 ± 0.3	0.94 ± 0.2
	p		0.07	0.19	0.04
PDX-NR	Treated	1.00 ± 0.0	1.03 ± 0.1	1.11 ± 0.3	1.19 ± 0.2
	Untreated	1.00 ± 0.0	1.07 ± 0.1	1.12 ± 0.2	1.05 ± 0.2
	p		0.52	0.93	0.22

with a baseline untreated control is available. In addition, this imaging method used for monitoring biomarker expression was the earliest of the three tested techniques in detecting a change, as reflected by the time at which change was detected (48 hours) and the statistical significance between groups ($p = 0.03$) in the PDX-R cohort.

Data illustrate that the degree of $\alpha_v\beta_3$ expression decreased at a faster rate for treated animals as compared to untreated animals in the PDX-R group, which was the observed trend over a 7-day window (-12% vs. -5%). Likewise, the PDX-NR group also experienced this trend, though the treated group was not significantly different from the untreated group (-4% vs. -2%, $p = 0.08$). This data may suggest that the PDX-NR group partially responded to the therapy, which would explain why we were unable to differentiate between the treated responder group and the treated non-responder group.

DCE-PI, which is a measurement of vascular perfusion and thus MVD, showed statistical significance on day 14 between treated and untreated populations in the PDX-R cohort. Thus, USMI provided information about therapy response prior to DCE-PI for the PDX-R group. This result was not unexpected, as changes in the microvasculature are likely preceded by a corresponding change in biomarker expression. Furthermore, it was predicted that healthy vasculature would have faster perfusion

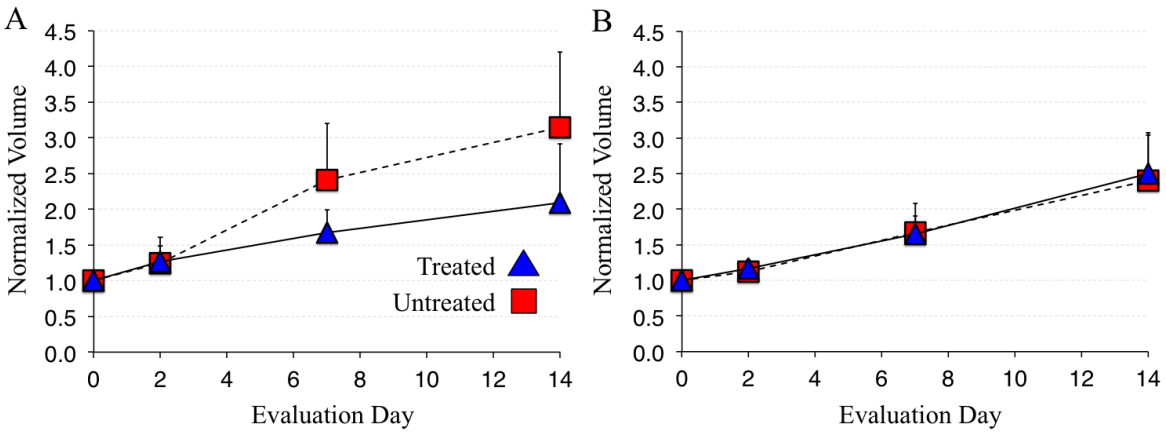

Figure 12.4: A) The tumor volume as measured by regions of interest from US b-mode for treated and untreated animals in a tumor known to respond to MLN8237 (N=7). B) The tumor volume as measured by regions of interest from US b-mode for treated and untreated animals in a tumor known not to respond to MLN8237 (N=7).

times relative to unhealthy microvasculature, which was the observed outcome in the DCE-PI study [166; 167]. Data illustrated that the perfusion times increased at a faster rate during treatment compared to untreated tumors, which was observed in our study (2% vs. 0%). Based on our results, DCE-PI appears to be a viable alternative to volume measurements in terms of identification and characterization of responder and non-responder cohorts for pre-clinical evaluations.

Using volume measurements for therapeutic pre-clinical mouse model studies is rapid, non-invasive and inexpensive; however, it is also high in variability, which is an impediment as a means for monitoring the response to therapy [168; 169]. In this study, volume measurements obtained with US did not show any significant differences between treated and untreated groups on any day for either the PDX-R or PDX-NR cohorts. In contrast, USMI and DCE-PI both demonstrated their ability to detect changes between treated and untreated populations in the responder group at earlier time points than with volume measurements. As with the DCE-PI technique, the volume curves for the treated and untreated treatment populations of the PDX-NR

Table 12.3: Summary of the normalized volumetric data for both treated and untreated animals in the PDX-R and PDX-NR cohorts. This data corresponds to the plots in Figure 12.4.

		Volume			
		Day 0	Day 2	Day 7	Day 14
PDX-R	Treated	1.00 ± 0.0	1.27 ± 0.2	1.68 ± 0.3	2.09 ± 0.8
	Untreated	1.00 ± 0.0	1.24 ± 0.4	2.41 ± 0.8	3.14 ± 1.1
	p		0.88	0.09	0.12
PDX-NR	Treated	1.00 ± 0.0	1.17 ± 0.1	1.66 ± 0.3	2.50 ± 0.6
	Untreated	1.00 ± 0.0	1.12 ± 0.1	1.68 ± 0.4	2.40 ± 0.7
	p		0.39	0.91	0.80

cohort during the time period of the imaging study provided no evidence to support that there was a partial response to therapy.

There are a number of factors that could have impacted how the evaluated techniques performed in this study. For instance, the strength of the evaluated therapeutic may favor one method over the other in terms of the measured effect. The stronger the therapeutic, the more likely the method may detect a change at earlier time points. An increase in dose was not evaluated in this study. Secondly, the readpoint sampling may have contributed to the observed performance of the DCE-PI study. If imaging was performed more frequently between day 2 and day 14, then more observed days with a significant difference between populations might have been observed prior to day 14. The tumor type may also have contributed to the performance of each technique. In the pancreatic adenocarcinoma tumor model that was used in this study, necrosis was observed to increase throughout the length of the study. As a tumor becomes more necrotic, it also becomes less vascular, which ultimately makes the untreated groups look similar to the treated groups. For instance, the untreated populations (PDX-R group) in our USMI study showed a gradual decrease in $\alpha_{\mathrm{v}}\beta_3$ expression. This decrease over time can mean one of two things. Either the vessels are not expressing the

angiogenic biomarker or there is not a vessel there to express the biomarker, which is more likely given that areas of necrosis were also observed in the DCE-PI study. Thus, as the untreated tumor becomes more naturally necrotic over time, it confounds the ability of the technique to distinguish between the treated and untreated groups. In future studies, for both USMI and DCE-PI, each of these factors must be explored. Finally, significance of this study was limited due to its short-term observation period. Future work will need to include larger subject numbers and longer time scales to more thoroughly validate our preliminary observations.

In order to evaluate the sensitivity of each technique's ability to identify a responder over a non-responder in a clinical situation, we evaluated the significance between treated groups at each readpoint. None of the evaluated techniques showed a statistically significant difference between treated groups (PDX-R treated vs. PDX-NR treated) at any readpoint. For this type of evaluation, normalization relative to the untreated groups is necessary. However, since normalization would not be relevant in a clinical situation, the methods as described here would not be clinically translatable without further improvement. Nevertheless, USMI and DCE-PI have illustrated substantial potential in pre-clinical response to therapy studies. Furthermore, it is very possible that these techniques still may be clinically significant without normalization in different tumor models or with therapeutic approaches, or after further improvements in imaging and contrast agent technology.

In conclusion, we showed that we could successfully identify a tumor as a responder or a non-responder with both USMI (day 2 and day 7) and DCE-PI (day 14) and at earlier time points than with volume measurements ($\sim$4 weeks). Second, we were able to characterize how the PDX-R and PDX-NR groups would respond over a 14-day period, which is an essential component in understanding the pathophysiologic

mechanisms of a particular type of cancer and it is an evolutionary step for a clinical-type application. Based on our results, we feel that characterization of a tumor in pre-clinical evaluations using USMI may allow for more effective drug development and an improvement in pharmacodynamic monitoring through reduced cycle times. Finally, since a volumetric approach has been shown to provide more accurate data than an equivalent 2-D analysis, we have succeeded in illustrating the strengths of 3-D USMI and 3-D DCE-PI for characterizing a tumor's response to therapy in pre-clinical studies.

CHAPTER 13

Discussion and Conclusion

13.1 Introduction

For molecular imaging to be effective in cancer treatment, underlying molecular, cellular, and physiologic processes that govern therapeutic receptiveness must be identified and quantified. USMI has emerged as a modality that may achieve this qualification by providing cellular and molecular information prior to any phenotypic changes precisely for applications such as response to therapy, disease identification and target delivery of therapeutics. USMI has made significant advances over the past decade, but has lacked advancement in many areas that are explored in this dissertation. To assess the validity of our hypotheses, we explored improvements to USMI techniques and utilized these techniques in the context of a response to cancer therapy application.

First, in Chapter 7, we explored what effect multiple targeted microbubble injections would have on the remaining number of biomarker receptors available for future targeting. The outcome showed that serial multiple injections in a USMI study do not bias or compromise the retention of targeted microbubbles due to competitive inhibition from previously bound MCAs. This conclusion was essential in confirming the validity of the data collected in subsequent chapters, which relied on multiple serial injections.

In Chapter 8, we evaluated what effect, if any, that the size of the microbubble had on both the persistence time and the sensitivity in an USMI study. We discovered that,

by increasing the mean diameter of the MCA population, a several-fold improvement in contrast sensitivity could be achieved. Next, in Chapter 9, we described how we could improve our ability to quantify biomarker expression by obtaining volumetric readings. We illustrated the necessity of volumetric molecular imaging by quantifying the variability in angiogenesis across a tumor. Data illustrated that 3-D USMI presents a more robust assessment of molecular marker expression throughout the tumors than standard 2-D US.

In Chapter 10, we demonstrated in an *in vivo* proof of concept, that we could enhance the quantity of adherent microbubbles in an USMI study. In all *in vivo* experiments, the volumetric targeted signal was greater when using ARF than with a traditional passive targeting approach without any loss in specificity. Chapter 11 logically followed and illustrated how we could selectively activate targeted microbubbles using ARF. Our data showed that, by incorporating a PEG overbrush in the microbubble shell architecture, we could create a pseudo-barrier in order to avoid competitive interactions between the ligand and plasma components. Ultimately, with this bubble architecture, we maintained specificity and prevented unwanted immunogenic reactions in an *in vivo* proof of concept.

Finally, we evaluated how well pancreatic adenocarcinoma responded to a novel aurora-A kinase inhibitor using improved USMI techniques, perfusion imaging and volume measurements. We showed that we could successfully identify a tumor as a responder or a non-responder with USMI and at earlier time points than with traditional volume measurements. While monitoring volumetric changes in response to therapy is the "gold standard" for pre-clinical studies, our data suggests that USMI may be used to earlier identify and robustly characterize tumor response.

13.2 Discussion - Improved USMI Techniques

In this section we discuss our hypotheses in greater context. We will explore the advantages of each technique described in this dissertation, the shortcomings, and future directions. Finally, we will assess the possibilities for clinical translation of USMI in the context of response to therapy.

13.2.1 Repeated Injections in an USMI Study

In this study, we explored how multiple serial injections of targeted MCAs affect future targeting. Our preliminary data suggests that multiple serial injections do not bias or compromise the MCA adherence in an USMI study. While the scope of this project was constrained to one tumor type and one dose, the outcome is encouraging. There are many instances where multiple targeted microbubble injections are required for comparison such as the assessment of acoustic radiation force to enhance targeting and the evaluation of the buried-ligand architecture. Since these studies used the same tumor model and similar MCA doses, our analysis of repeated serial injections helps solidify our conclusions and paves the way for future USMI studies.

While the results of this study are promising, the scope was limited and based mainly on parameters utilized throughout this dissertation. First, the study only utilized one tumor type. Future studies on this topic should incorporate various cancer types, preferably known to have various degrees of $\alpha_v\beta_3$ expression. This would allow a more thorough analysis of whether or not, multiple MCA injections block a quantity of target sites that would be detrimental to the analysis. Second, the dose and size distribution of microbubbles were limited. It would be advantageous to know if concentration and the size of the microbubble played any role in competitive inhibition.

Another question that arises is whether or not using a mechanical index of 1.9

damages the adjacent vessel walls when clearing the targeted microbubbles after repeated injections. Any vessel damage would confound our ability to accurately assess biomarker expression. A previous study has shown that clearing bubbles with a higher MI at higher frequencies, such as the 7 MHz utilized in our studies, does not seem to cause detectable vessel damage [90]. However, since insonation frequency and MCA resonance are intricately coupled, in future studies it would be of great interest to vary the frequency and pressure along with microbubble size to determine if there are any increased bioeffects that may affect our ability to utilize multiple serial injections in USMI.

Finally, it is clear that the quantity of over-expressed $\alpha_v\beta_3$ integrin is greater than the number of injected microbubbles. For example, in a typical human umbilical vein endothelial cell (HUVEC), there are up to 5 x 10^5 $\alpha_v\beta_3$ receptors per cell [170; 171]. The average HUVEC cell size is approximately 17 μm, which makes the surface area $\sim$900 μm^2 assuming a spherical cell. This equates to $\sim$550 receptors per square micron. The average size the MCAs used in this experiment were approximately 4 μm, thus we would clearly not expect all of the receptors in this area to be populated. Upon cursory examination, there are many more receptors than microbubbles, which supports our findings. Based on this examination, if MCAs are not populating all of the target receptors, can this technique be used to accurately determine the quantity of biomarker expression? Ultimately, in any USMI application, our technique is only as sensitive as our ability to detect the target biomarker expression. Thus, in the greater context of using USMI to quantify disease progression, this must be explored.

13.2.2 Size-Selection for Sensitivity Improvement

Preferential selection of the microbubble size improved our ability to sensitively detect targeted microbubbles in USMI. We demonstrated a several-fold improvement in

contrast enhancement by tailoring MCA size distributions using centrifugation. This is significant in instances where the microbubble targeting is low and maximum sensitivity is required. For instance in a response to therapy study, as animals are treated over time and biomarker expression is diminished, it is imperative to have low-level sensitivity to targeted MCAs. In addition, we discovered that we could achieve greater contrast sensitivities with fewer injected microbubbles. Of course, this is advantageous for minimizing the exposure to foreign particles. Finally, size-selection has assisted in our ability to generate images by illustrating spatial distribution of targeting well above the noise floor.

While microbubble size-selection has proved to be invaluable in pre-clinical studies, there are still limitations and obstacles that must be overcome for clinical advancement. First, it must be noted that centrifugation offers a substantial improvement in production yields and MCA stability over techniques such as microfluidics. Unfortunately, only a few size distributions may be extracted by using the centrifugation technique. Thus, in applications where matching the resonant frequency to the microbubble diameter is important, there is limited flexibility. Though, in my experience, the scattering cross-section may be more significant than matching the resonant frequency to the microbubble diameter, which should be explored in future characterization studies. Another detriment to the centrifugation method for sorting is that the process is time-consuming and the yield (resultant number of microbubbles) is relatively low, though better than other methods. Finally, mass-production for clinical implementation may be difficult due to handling issues and maintaining a sterile environment.

Ideally, a monodisperse population of microbubbles is desired for a number of reasons. This includes an improvement in our ability to quantify biomarkers, better predictability for *in vivo* MCA persistence, and exactly matching the resonant frequency of the system to the size of the MCA. Unfortunately, the resultant size distribution

with centrifugation is not monodisperse. Thus, any future desire to correlate intensity to the number of microbubbles (or biomarkers) will be challenging. However, since backscatter is related to the insonation frequency, it may be possible to determine size related information by scanning the targeted microbubbles at various frequencies and implementing a compounding technique. Finally, since maximum translation of microbubbles using ARF is at the resonant frequency, a wide range of microbubble sizes makes ARF-enhanced molecular imaging less efficient and less predictable.

As mentioned previously, large microbubbles may be more susceptible to detachment than smaller microbubbles, due to greater *in vivo* shear forces. Thus, larger microbubbles may attach and subsequently detach within the time that we wait for free-flowing MCAs to clear the circulation. Currently, our USMI procedure does not account for this situation. However, real-time approaches to USMI are being evaluated to determine receptor expression over time for a more accurate evaluation.

13.2.3 3-D for Improved Quantification

In Chapter 9, we used volumetric USMI to illustrate the heterogeneity of $\alpha_v\beta_3$ in a tumor, thus emphasizing the necessity of a 3-D approach. Furthermore, we showed that a traditional 2-D USMI study may misrepresent the angiogenic expression by as much as 28%. Moreover, 2-D USMI studies that evaluate biomarker expression over time are susceptible to error. Maintaining the exact 2-D slice position and orientation are essential for these types of studies. Thus, error increases substantially when the transducer is removed from a fixed clamp and repositioned. A volumetric USMI approach, however, eliminates the possibility for this type of error.

Volumetric USMI is clearly the more effective way to quantify biomarker expression as compared to an equivalent 2-D study. The setup that was used in our study was a 1-D linear array that was positioned in a fixed clamp and scanned elevationally

to produce a stacked volume of images. This implementation was a requirement for pre-clinical studies due to the way in which we quantify the targeted MCAs at each discretized step. Unfortunately, the implementation of this type of setup in a clinical environment would be very difficult, if not impossible. Thus, due to the lack of clinical 3-D ultrasound probes with contrast detectability, clinical translation of volumetric USMI may not be feasible, which limits its integration to pre-clinical studies. As 3-D contrast-enhanced clinical probes become more prevalent, this will no longer be an impediment.

As 3-D clinical probes become available with contrast-enhanced detection schemes, it will be important to evaluate the sensitivity of 3-D USMI relative to a 2-D approach. For instance, due to the increased number of transducing elements in the elevational direction, 3-D probes have the ability to focus and steer in both the lateral and elevational directions. While the resolution of the transducer in the elevational direction is greatly improved, the sensitivity in detecting larger number of microbubbles may be compromised due to the smaller beam that interrogates the contrast agents. However, due to the improvement in sensitivity by size-selecting microbubbles, this may be a non-issue. Regardless, there may be a trade-off between resolution and sensitivity to large populations of microbubbles moving from a 2-D to 3-D USMI approach, which must be explored as 3-D probes become available for USMI.

13.2.4 ARF-Enhanced USMI for Improved Adherence

In this study, we presented the first non-invasive *in vivo* validation of ARF-enhanced USMI with an unmodified clinical system. By utilizing ARF, we were able to demonstrate an $\sim$80% increase in targeted microbubble intensity relative to a traditional passive targeting approach. Furthermore, ARF did not significantly increase image contrast when applied to non-targeted MCAs, suggesting that ARF did not increase

non-specific adhesion.

This particular technique yielded an appreciable increase in microbubble adherence over passive targeting. While ARF-enhanced targeting is significant in merit, and could yield tremendous benefits, there are drawbacks with its current implementation. First, the volumetric application of ARF is not trivial. The current implementation uses an imprecise mechanism for controlling the time in which ARF is administered, which may inadvertently increase secondary radiation force effects or over-pushing. Thus, it is difficult to maintain accuracy and consistency for longitudinal studies. In future studies, consistency of the method in a particular animal and tumor should be evaluated. Second, due to attenuation effects, and therefore axial administration deficiencies, application of ARF may be different for various-sized tumors. This is a deleterious consequence for any response to therapy study that evaluates biomarker expression as the tumor volume changes over time. Moreover, the inconsistent axial administration of ARF would be exacerbated in a clinical environment where human subjects exhibit increased attenuation in much deeper tissues. Also, to further expound on clinical translation of this technique, each patient may have a different size tumor. Therefore, standardization of the technique may be difficult, which is burdensome for radiologists and physicians who rely on robust techniques for diagnosis. These deficiencies were the primary reason for not utilizing this technique in our pre-clinical response to therapy evaluation.

In order to advance ARF-enhanced targeting technique to a more clinically-suited method, a system must be created to overcome the previously described deficiencies. A clinical system that allows precise control over power (applied pressure amplitude), depth of administration, pulse length and timed-delivery is ideal for ARF-enhanced targeting. Implementation of this type of system would allow for strategies in which

a more homogeneous administration of ARF is achieved. For instance, a higher pressure may be used first to facilitate microbubble targeting deeper into tissue (due to attenuation) while simultaneously over-pushing at shallow depths. Steadily reducing the pressure would allow microbubbles at shallower depths to be pushed at a more appropriate pressure without negatively affecting the targeted bubbles deeper in the tissue. A system with this type of flexibility and dedicated support is essential for the advancement of the technique beyond pre-clinical experiments.

For future pre-clinical evaluations, it will be important to evaluate the importance of matching the MCA size to the system frequency. Since maximum MCA translation is achieved at the resonant frequency of the microbubble, optimal retention may not yet be realized. Furthermore, the time of ARF administration needs to be examined along with an evaluation of using a bolus injection over a continuous infusion of MCAs throughout the administration time-window. Finally, for traditional passive targeting, increasing the dose of microbubbles directly correlates with an increase in MCA targeting. However, with ARF-enhancement, sufficient targeting may be achieved with a reduction in MCA dose. Thus, in the context of ARF-enhanced targeting, evaluating the quantity of injected MCAs to achieve maximum targeting should be evaluated.

13.2.5 BLA for Reduced Immunogenic Response

In this *in vivo* proof of concept, we successfully created a microbubble that was designed to shield a targeting ligand from plasma components that may lead to non-specific adhesion and potentially stimulate an undesired immunogenic response. Not only did we maintain our targeted specificity for $\alpha_{\mathrm{v}}\beta_3$ integrin, we provided evidence that the PEG overbrush had the necessary barrier properties to avoid competitive interactions between the ligand and plasma components in circulation. In addition, this technique allowed us to administer targeted agents at the tumor site providing enhanced specificity

while reducing the possibility of targeting elsewhere, thus minimizing undesired side-effects. This body of work is the most relevant to the discussion of clinical translation as avoiding stimulating immunogenic reactions is imperative for user safety. Finally, this work paves the way for the advancement of clinical US systems that incorporate user-controlled ARF functionality.

To our knowledge, this was the first time that US has been used to activate targeting specificity for *in vivo* molecular imaging. While this is a breakthrough, due to its dependence on ARF, this technique has the same drawbacks that were considered in section 13.2.4. Additionally, most pre-clinical studies utilize microbubbles that incorporate a (biotin-streptavidin)-based structure tethered to a biotinylated antibody for targeting various biomarkers. While this MCA architecture is well-suited for flexibility, streptavidin is immunogenic, and therefore, these types of microbubbles cannot be used in humans. Thus, the assorted targeted MCAs that are currently available for pre-clinical USMI could not be used clinically. This is due to the physical length of the PEG structure and its inability to shield the longer biotin-streptavidin-biotin-antibody complex from the plasma components. Antibodies and other targeting mechanisms must be small enough to be shielded by the PEG barrier for functional efficacy, which is not always the case. Novel targeted MCAs (not including $\alpha_v\beta_3$ integrin) with a more advanced chemistry need to be developed for clinical advancement such as BR55, the VEGF-targeted microbubble recently developed by ©Bracco [159].

13.3 Discussion - Response to Therapy

Predicting response to cancer therapy has been a central motivation for the development and advancement of USMI. In general, with a response to therapy study, there are two interesting questions that arise. First, "does a particular tumor respond to a given therapy?" More specifically, can we identify a tumor as a responder or a non-responder,

and additionally, at what point in time may we determine this information? This may be resolved, as we did in our response to therapy study, by evaluating one type of tumor with and without treatment over time. By analyzing when the response curves significantly diverge, we can determine how well and when, a particular tumor type responds to therapy relative to the non-treated control. This type of assessment is ideal for pre-clinical research and drug evaluations. For example, if a novel drug is evaluated for its efficacy in a particular type of cancer, then early information will lead to fast decision-making in the framework of drug development cycle times and responder/non-responder identification. Naturally, this would yield a benefit with respect to managing resources and saving costs. Unfortunately, this type of evaluation is ill-suited for clinical translation, because there would never be a situation where patients were not treated. If in the course of pre-clinical research, a unique response curve was established that did not require normalization to the untreated populations, then response to therapy with USMI may be clinically viable.

This particular scenario brings us to a more clinically relevant question: "can we determine if a tumor is responding to therapy over time with no additional information?" For instance, if a patient with a particular form of cancer started treatment, can we predict if that patient is responding to treatment by only monitoring the response to therapy over time relative to historical data (not an untreated control)? By historically and statistically evaluating the response (Treated Responder vs. Treated Non-Responder) that many patients have to a particular form of therapy, it is possible to answer the question; however, the response must be statistically well-behaved. Namely, there must be a clear delineation between a tumor that responds to therapy over time or does not respond to therapy. Unfortunately, there may be some tumors that marginally respond to the therapy, which confounds our ability for diagnosis without having a control for a reference.

Table 13.1: Response to Therapy Example Scenario

	Day 0	Day 7	Day 14
Responder-Treated	1.0	1.1	1.2
Responder-Not Treated	1.0	1.5	2.4
Non-Responder-Treated	1.0	1.1	1.2
Non-Responder-Not Treated	1.0	1.2	1.4

The downside to not having an untreated control may be illustrated in the following what-if scenario. Suppose there were two patients with tumors of the same type. One patient's tumor is more aggressive in its growth rate relative to the other patient's tumor (Table 13.1). At Day 14, the two treated groups have the same value. This comparison does not accurately reflect the significance of the data. The significance emanates from the fact that the treated responder had half the value of the tumor that was not treated, and thus clearly affirming the efficacy of treatment. Since the growth rates between the two untreated groups are different, it is not accurate to only compare the treated groups without some form of normalization. For the most effective evaluation, we must have an untreated control group for the purpose of normalization, which is not possible in the clinical application. Thus, for clinical viability, a well-behaved tumor that either responds or does not respond to therapy is essential for successful translation.

In our response to therapy study, we showed that volumetric USMI may be used to earlier identify and robustly characterize tumor response. First, we showed that we could label a tumor as responder or non-responder earlier than with volume measurements. Second, we were able to characterize how the responder and non-responder cohorts would respond over a 14-day period. As previously mentioned, this type of characterization is an essential component in understanding the underlying mechanisms of a particular type of cancer. Furthermore, it is an evolutionary step for a pre-clinical drug development and clinical translation. Finally, we succeeded in illustrating the

strengths of 3-D USMI (versus a 2-D study) for characterizing a tumor's response to therapy in pre-clinical studies.

Our study illustrated that USMI, at least for this tumor type and therapy, allows us to identify and characterize a tumor in a pre-clinical setting where untreated controls are available for comparison. Additionally, we can determine whether or not a tumor will respond to therapy at earlier time points than with traditionally used volume measurements. Unfortunately, none of the evaluated techniques showed a statistically significant difference between treated groups (Treated Responder vs. Treated Non-Responder) at any readpoint. Thus, we do not have a sensitive enough technique to distinguish between a tumor that responds well and a tumor that marginally responds to this form of therapy, which is the ideal case for clinical translation. For a clinically viable USMI technique, a well-behaved tumor that either responds or does not respond to therapy is needed. A responder would follow one unique response to therapy curve while a non-responder would have a much different response curve. As previously discussed, this is because the only comparison to be made is relative to the first imaging readpoint, not an untreated control. Thus, having a historical and statistically significant response curve for many patients is the foundation for successful clinical translation. In conclusion, we were successful in determining a tumor's response to therapy using USMI; however, at this time, this type of evaluation may be best suited for pre-clinical studies.

13.4 Discussion - Clinical Translation

For successful clinical translation of USMI for response to therapy evaluations, it is important to identify suitable niches where the modality adds needed information that cannot be easily obtained by other methods. Thus, in the future, different tumor types need to be evaluated with various therapeutic strategies to statistically identify the

most suitable candidates for clinical translation. Moreover, it would be invaluable to compare this type of USMI study to a metabolic assessment using PET/CT imaging (or other proven modalities) to evaluate the effectiveness relative to a clinically applicable technique. If PET imaging offers physicians a more reliable molecular imaging approach to diagnosis relative to USMI, then clinical translation of USMI may not be appropriate. However, due to its portability, no associated ionizing radiation, and real-time capabilities, there is a clear advantage for USMI if a suitable niche is discovered.

To date, USMI has not been used clinically, which is largely related to the lack of FDA-approved targeted MCAs. It is likely that the main reason for the delay is the concern by pharmaceutical companies regarding user safety and the size of the market for molecularly targeted agents. As mentioned earlier, there is a small niche that must be established in order to be clinically viable. If there is little to no demand for the product (targeted microbubbles), then pharmaceutical companies will be hesitant to invest in that particular business model. In addition to needing an FDA-approved targeted microbubble, there are other considerations for clinical translation of USMI. First, well-done clinical trials of the application must be accomplished with a clear understanding of the procedure and analysis. This includes having a large number of patients for statistical relevance. One critical aspect in the context of clinical trials is test and retest reproducibility. Incorporating test and retest assessments into clinical trials serves as a useful quality control measure especially for USMI, which is quite computational. Also, interpretation of the images is operator-dependent; therefore, future pre-clinical USMI evaluations should include more rigorous analysis-based assessments. Moreover, it is important to train physicians and clinicians regarding new techniques, which can be quite difficult given the complexity of USMI. Last, there must be readily available clinical ultrasound systems that are capable of detecting MCAs and separating them from tissue. There are numerous systems that have this capability,

but unfortunately, they do not all utilize the same MCA detection scheme; therefore, repeatability and standardization across platforms may be difficult. While there remain significant near-term challenges in clinical translation of USMI, the long-term benefits of an ultrasound-based approach are considerable and must be explored.

13.5 Conclusion

Molecular imaging with ultrasound is an exciting new field that offers the potential to detect pathology before phenotypic changes occur using inexpensive and portable ultrasound systems without ionizing radiation. Although, significant advances have been made, the technologies enabling molecular imaging are still in development. Commercial imaging systems are still being optimized for molecular imaging, and targeted contrast agents for clinical and veterinary use are still not widely available. Although molecularly targeted contrast agents have been used in animal studies for nearly two decades, the safety and clinical utility of using ultrasound molecular imaging in humans is in its infancy.

While significant progress has been made in USMI techniques over the past decade, there remain challenges that need to be addressed as this technique proceeds toward clinical relevance. This dissertation provides improved techniques towards the advancement of USMI with respect to sensitivity, specificity, and quantification. Moreover, we utilized these improvements to successfully assess a tumor's response to therapy and compare it to more traditional methods. While the current implementation of USMI is best suited for pre-clinical evaluations, considering the potential advantages of this technique, it is reasonable to expect that ultrasonic molecular imaging may have a place in the clinic in the future.

Bibliography

[1] R. W. Ruddon, *Cancer Biology*. Oxford University Press, 4th ed., Jan 2007.

[2] S. Pelengaris and M. Khan, eds., *The Molecular Biology of Cancer*. Blackwell Publishing, Jan 2006.

[3] J. Gabriel, *The Biology of Cancer*. John Wiley and Sons, Ltd., 2nd ed., Nov 2007.

[4] A. C. Society, "Cancer facts & figures 2013," *American Cancer Society*, pp. 1–60, 2013.

[5] H. H. Pien, A. J. Fischman, J. H. Thrall, and A. G. Sorensen, "Using imaging biomarkers to accelerate drug development and clinical trials," *Drug Discov Today*, vol. 10, pp. 259–66, Feb 2005.

[6] S. Apisarnthanarax and K. S. C. Chao, "Current imaging paradigms in radiation oncology," *Radiat Res*, vol. 163, pp. 1–25, Jan 2005.

[7] M. H. Michalski and X. Chen, "Molecular imaging in cancer treatment," *Eur J Nucl Med Mol Imaging*, vol. 38, pp. 358–77, Feb 2011.

[8] M. Allison, "Is personalized medicine finally arriving?," *Nat Biotechnol*, vol. 26, pp. 509–17, May 2008.

[9] G. Kramer-Marek and J. Capala, "The role of nuclear medicine in modern therapy of cancer," *Tumour Biol*, vol. 33, pp. 629–40, Jun 2012.

[10] J. Leyton, J. R. Latigo, M. Perumal, H. Dhaliwal, Q. He, and E. O. Aboagye, "Early detection of tumor response to chemotherapy by 3'-deoxy-3'-[18F]fluorothymidine positron emission tomography: the effect of cisplatin on a fibrosarcoma tumor model in vivo," *Cancer Res*, vol. 65, pp. 4202–10, May 2005.

[11] W. S. Richter, "Imaging biomarkers as surrogate endpoints for drug development," *Eur J Nucl Med Mol Imaging*, vol. 33 Suppl 1, pp. 6–10, Jul 2006.

[12] M. J. Ratain and S. G. Eckhardt, "Phase II studies of modern drugs directed against new targets: if you are fazed, too, then resist RECIST," *J Clin Oncol*, vol. 22, pp. 4442–5, Nov 2004.

[13] J. Goffin, S. Baral, D. Tu, D. Nomikos, and L. Seymour, "Objective responses in patients with malignant melanoma or renal cell cancer in early clinical studies do not predict regulatory approval," *Clin Cancer Res*, vol. 11, pp. 5928–34, Aug 2005.

[14] F. A. Shepherd, J. R. Pereira, T. Ciuleanu, E. H. Tan, V. Hirsh, S. Thongprasert, D. Campos, S. Maoleekoonpiroj, M. Smylie, R. Martins, M. van Kooten, M. Dediu, B. Findlay, D. Tu, D. Johnston, A. Bezjak, G. Clark, P. Santabárbara, L. Seymour, and N. C. I. of Canada Clinical Trials Group, "Erlotinib in previously treated non-small-cell lung cancer," *N Engl J Med*, vol. 353, pp. 123–32, Jul 2005.

[15] R. Ford, L. Schwartz, J. Dancey, L. E. Dodd, E. A. Eisenhauer, S. Gwyther, L. Rubinstein, D. Sargent, L. Shankar, P. Therasse, and J. Verweij, "Lessons learned from independent central review," *Eur J Cancer*, vol. 45, pp. 268–74, Jan 2009.

[16] R. Weissleder and M. J. Pittet, "Imaging in the era of molecular oncology," *Nature*, vol. 452, pp. 580–9, Apr 2008.

[17] G. J. Kelloff, K. A. Krohn, S. M. Larson, R. Weissleder, D. A. Mankoff, J. M. Hoffman, J. M. Link, K. Z. Guyton, W. C. Eckelman, H. I. Scher, J. O'Shaughnessy, B. D. Cheson, C. C. Sigman, J. L. Tatum, G. Q. Mills, D. C. Sullivan, and J. Woodcock, "The progress and promise of molecular imaging probes in oncologic drug development," *Clin Cancer Res*, vol. 11, pp. 7967–85, Nov 2005.

[18] M. A. Pysz, S. S. Gambhir, and J. K. Willmann, "Molecular imaging: current status and emerging strategies," *Clin Radiol*, vol. 65, pp. 500–16, Jul 2010.

[19] J. E. Streeter and P. A. Dayton, "Ultrasonic molecular imaging," *Advance for Imaging & Radiation Oncology*, pp. 1–6, Apr 2011.

[20] L. de Geus-Oei, D. Vriens, H. van Laarhoven, W. van der Graaf, and W. Oyen, "Monitoring and predicting response to therapy with 18F-FDG PET in colorectal cancer: a systematic review," *J Nucl Med*, vol. 50, no. Suppl 1, pp. 43S–54S, 2009.

[21] R. Wahl, H. Jacene, Y. Kasamon, and M. Lodge, "From RECIST to PERCIST: Evolving considerations for PET response criteria in solid tumors," *J Nucl Med*, vol. 50, no. Suppl 1, pp. 22S–50S, 2009.

[22] E. Ruoslahti, "Integrins as signaling molecules and targets for tumor therapy," *Kidney Int*, vol. 51, pp. 1413–7, May 1997.

[23] R. Haubner, H. Wester, U. Reuning, R. Senekowitsch-Schmidtke, B. Diefenbach, H. Kessler, G. Stöcklin, and M. Schwaiger, "Radiolabeled alpha(v)beta3 integrin antagonists: a new class of tracers for tumor targeting," *J Nucl Med*, vol. 40, no. 6, pp. 1061–1071, 1999.

[24] A. Beer, R. Haubner, M. Goebel, S. Luderschmidt, M. Spilker, H. Wester, W. Weber, and M. Schwaiger, "Biodistribution and pharmacokinetics of the alphavbeta3-selective tracer 18F-galacto-RGD in cancer patients," *J Nucl Med*, vol. 46, no. 8, pp. 1333–1341, 2005.

[25] A. Beer, R. Haubner, I. Wolf, M. Goebel, S. Luderschmidt, M. Niemeyer, A. Grosu, M. Martinez, H. Wester, W. Weber, and M. Schwaiger, "PET-based human dosimetry of 18F-galacto-RGD, a new radiotracer for imaging alpha v beta3 expression," *J Nucl Med*, vol. 47, no. 5, pp. 763–769, 2006.

[26] A. C. O. Farrell, S. D. Shnyder, G. M. P. L. Coletta, and J. H. Gill, "Non-invasive molecular imaging for preclinical cancer therapeutic development," *Br J Pharmacol*, vol. [Epub ahead of print], 2013.

[27] A. Rahmim and H. Zaidi, "PET versus SPECT: strengths, limitations and challenges," *Nucl Med Commun*, vol. 29, no. 3, pp. 193–207, 2008.

[28] S. Lyons, "Advances in imaging mouse tumour models in vivo," *J Pathol*, vol. 205, no. 2, pp. 194–205, 2005.

[29] M. Ali, B. Janic, A. Babajani-Feremi, N. Varma, A. Iskander, J. Anagli, and A. Arbab, "Changes in vascular permeability and expression of different angiogenic factors following anti-angiogenic treatment in rat glioma," *PLoS One*, vol. 5, no. 1, 2010.

[30] Z. Huang, S. Teh, W. Zheng, J. Mo, K. Lin, X. Shao, K. Ho, M. Teh, and K. Yeoh, "Integrated Raman spectroscopy and trimodal wide-field imaging techniques for real-time in vivo tissue Raman measurements at endoscopy," *Opt Lett*, vol. 34, no. 6, pp. 758–760, 2009.

[31] J. Motz, M. Fitzmaurice, A. Miller, S. Gandhi, A. Haka, L. Galindo, R. Dasari, J. Kramer, and M. Feld, "In vivo Raman spectral pathology of human atherosclerosis and vulnerable plaque," *J Biomed Opt*, vol. 11, no. 2, pp. 1–9, 2006.

[32] E. Fomchenko and E. Holland, "Mouse models of brain tumors and their applications in preclinical trials," *Clin Cancer Res*, vol. 12, no. 18, pp. 5288–5297, 2006.

[33] W. Loo, H. Sasano, and L. Chow, "Effects of capecitabine and vinorelbine on cell proliferation, metabolism and COX2 and p16 expression in breast cancer cell lines and solid tumour tissues," *Biomed Pharmacother*, vol. 61, no. 9, pp. 596–600, 2007.

[34] H. Leong-Poi, "Molecular imaging using contrast-enhanced ultrasound: evaluation of angiogenesis and cell therapy," *Cardiovasc Res*, vol. 84, pp. 190–200, Nov 2009.

[35] J. K. Willmann, N. van Bruggen, L. M. Dinkelborg, and S. S. Gambhir, "Molecular imaging in drug development," *Nat Rev Drug Discov*, vol. 7, pp. 591–607, Jul 2008.

[36] E. Quaia and T. V. Bartolotta, *Contrast Media in Ultrasonography: Basic Principles and Applications*. Springer, Jan 2005.

[37] R. S. C. Cobbold, *Foundations of Biomedical Ultrasound*. Oxford University Press, Jan 2007.

[38] J. E. Streeter, R. C. Gessner, I. Miles, and P. A. Dayton, "Improving sensitivity in ultrasound molecular imaging by tailoring contrast agent size distribution: in vivo studies," *Mol Imaging*, vol. 9, pp. 87–95, Apr 2010.

[39] K. Hettiarachchi, E. Talu, M. L. Longo, P. A. Dayton, and A. P. Lee, "On-chip generation of microbubbles as a practical technology for manufacturing contrast agents for ultrasonic imaging," *Lab Chip*, vol. 7, pp. 463–8, Apr 2007.

[40] U. Farook, E. Stride, M. J. Edirisinghe, and R. Moaleji, "Microbubbling by co-axial electrohydrodynamic atomization," *Med Biol Eng Comput*, vol. 45, pp. 781–9, Aug 2007.

[41] J. A. Feshitan, C. C. Chen, J. J. Kwan, and M. A. Borden, "Microbubble size isolation by differential centrifugation," *J Colloid Interface Sci*, vol. 329, pp. 316–324, Jan 2009.

[42] S. Sirsi, J. A. Feshitan, J. Kwan, S. Homma, and M. A. Borden, "Effect of microbubble size on fundamental mode high frequency ultrasound imaging in mice," *Ultrasound Med Biol*, vol. 36, pp. 935–48, Jun 2010.

[43] J. K. Willmann, R. Paulmurugan, K. Chen, O. Gheysens, M. Rodriguez-Porcel, A. M. Lutz, I. Y. Chen, X. Chen, and S. S. Gambhir, "US imaging of tumor angiogenesis with microbubbles targeted to vascular endothelial growth factor receptor type 2 in mice," *Radiology*, vol. 246, pp. 508–18, Feb 2008.

[44] P. A. Schumann, J. P. Christiansen, R. M. Quigley, T. P. McCreery, R. H. Sweitzer, E. C. Unger, J. R. Lindner, and T. O. Matsunaga, "Targeted-microbubble binding selectively to GPIIb IIIa receptors of platelet thrombi," *Invest Radiol*, vol. 37, pp. 587–93, Nov 2002.

[45] H. Leong-Poi, J. P. Christiansen, A. L. Klibanov, S. Kaul, and J. R. Lindner, "Noninvasive assessment of angiogenesis by ultrasound and microbubbles targeted to alpha(v)-integrins," *Circulation*, vol. 107, pp. 455–60, Jan 2003.

[46] P. A. Dayton, A. L. Klibanov, G. Brandenburger, and K. W. Ferrara, "Acoustic radiation force in vivo: a mechanism to assist targeting of microbubbles," *Ultrasound Med Biol*, vol. 25, pp. 1195–201, Oct 1999.

[47] J. J. Rychak, A. L. Klibanov, and J. A. Hossack, "Acoustic radiation force enhances targeted delivery of ultrasound contrast microbubbles: in vitro verification," *IEEE Trans Ultrason Ferroelectr Freq Control*, vol. 52, pp. 421–33, Mar 2005.

[48] J. J. Rychak, A. L. Klibanov, K. F. Ley, and J. A. Hossack, "Enhanced targeting of ultrasound contrast agents using acoustic radiation force," *Ultrasound Med Biol*, vol. 33, pp. 1132–9, Jul 2007.

[49] R. C. Gessner, M. Lukacs, M. Lee, J. Tsuruta, F. S. Foster, and P. A. Dayton, "Radiation force-enhanced targeted imaging and near real-time molecular imaging using a dual-frequency high-resolution transducer: In-vitro and in-vivo results," *IEEE Ultrasonics Symposium*, p. 4, Jan 2010.

[50] C. C. Chen and M. A. Borden, "The role of poly(ethylene glycol) brush architecture in complement activation on targeted microbubble surfaces," *Biomaterials*, vol. 32, pp. 6579–87, Sep 2011.

[51] M. A. Borden, M. R. Sarantos, S. M. Stieger, S. I. Simon, K. W. Ferrara, and P. A. Dayton, "Ultrasound radiation force modulates ligand availability on targeted contrast agents," *Mol Imaging*, vol. 5, pp. 139–47, Jul 2006.

[52] M. A. Borden, H. Zhang, R. J. Gillies, P. A. Dayton, and K. W. Ferrara, "A stimulus-responsive contrast agent for ultrasound molecular imaging," *Biomaterials*, vol. 29, pp. 597–606, Feb 2008.

[53] M. A. Pysz, K. Foygel, J. Rosenberg, S. S. Gambhir, M. Schneider, and J. K. Willmann, "Antiangiogenic cancer therapy: monitoring with molecular US and a clinically translatable contrast agent (BR55)," *Radiology*, vol. 256, pp. 519–27, Aug 2010.

[54] M. Palmowski, J. Huppert, G. Ladewig, P. Hauff, M. Reinhardt, M. M. Mueller, E. C. Woenne, J. W. Jenne, M. Maurer, G. W. Kauffmann, W. Semmler, and F. Kiessling, "Molecular profiling of angiogenesis with targeted ultrasound imaging: early assessment of antiangiogenic therapy effects," *Mol Cancer Ther*, vol. 7, pp. 101–9, Jan 2008.

[55] G. M. Lanza, K. Wallace, M. Scott, W. Cacheris, D. Abendschein, D. Christy, A. Sharkey, J. Miller, P. Gaffney, and S. Wickline, "A novel site-targeted ultrasonic contrast agent with broad biomedical application," *Circulation*, vol. 94, pp. 3334–3340, Jan 1996.

[56] P. A. Dayton and J. J. Rychak, "Molecular ultrasound imaging using microbubble contrast agents," *Front Biosci*, vol. 12, pp. 5124–42, Jun 2007.

[57] K. W. Ferrara, M. A. Borden, and H. Zhang, "Lipid-shelled vehicles: engineering for ultrasound molecular imaging and drug delivery," *Acc Chem Res*, vol. 42, pp. 881–92, Jul 2009.

[58] R. Suzuki, Y. Oda, N. Utoguchi, E. Namai, Y. Taira, N. Okada, N. Kadowaki, T. Kodama, K. Tachibana, and K. Maruyama, "A novel strategy utilizing ultrasound for antigen delivery in dendritic cell-based cancer immunotherapy," *J Control Release*, vol. 133, pp. 198–205, Oct 2009.

[59] J. R. Lindner, "Molecular imaging of cardiovascular disease with contrast-enhanced ultrasonography," *Nat Rev Cardiol*, vol. 6, pp. 475–481, Jul 2009.

[60] S. M. Stieger, P. A. Dayton, M. A. Borden, C. F. Caskey, S. M. Griffey, E. R. Wisner, and K. W. Ferrara, "Imaging of angiogenesis using cadence contrast pulse sequencing and targeted contrast agents," *Contrast Media Mol Imaging*, vol. 3, pp. 9–18, Jan 2008.

[61] M. A. Kuliszewski, H. Fujii, C. Liao, A. H. Smith, A. Xie, J. R. Lindner, and H. Leong-Poi, "Molecular imaging of endothelial progenitor cell engraftment using contrast-enhanced ultrasound and targeted microbubbles," *Cardiovasc Res*, vol. 83, pp. 653–662, Sep 2009.

[62] C. Marelli, "Preliminary experience with NC100100, a new ultrasound contrast agent for intravenous injection," *Eur Radiol*, vol. 9 Suppl 3, pp. S343–6, Jan 1999.

[63] E. Unger, D. Shen, T. Fritz, B. Kulik, P. Lund, G. L. Wu, D. Yellowhair, R. Ramaswami, and T. Matsunaga, "Gas-filled lipid bilayers as ultrasound contrast agents," *Invest Radiol*, vol. 29 Suppl 2, pp. S134–6, Jun 1994.

[64] R. Basilico, M. J. K. Blomley, D. O. Cosgrove, J. B. Liull, A. Broillet, A. Bauer, and L. Bonomo, "The first phase I study of a novel ultrasound contrast agent (BR14): assessment of safety and efficacy in liver and kidneys," *Acad Radiol*, vol. 9 Suppl 2, pp. S380–1, Aug 2002.

[65] A. L. Klibanov, "Microbubble contrast agents: targeted ultrasound imaging and ultrasound-assisted drug-delivery applications," *Invest Radiol*, vol. 41, pp. 354–62, Mar 2006.

[66] A. L. Klibanov, "Preparation of targeted microbubbles: ultrasound contrast agents for molecular imaging," *Med Biol Eng Comput*, vol. 47, pp. 875–82, Aug 2009.

[67] B. A. Kaufmann, K. Wei, and J. R. Lindner, "Contrast echocardiography," *Curr Prob Cardiology*, vol. 32, pp. 51–96, Feb 2007.

[68] J. P. Reilly, P. A. Tunick, R. J. Timmermans, B. Stein, B. P. Rosenzweig, and I. Kronzon, "Contrast echocardiography clarifies uninterpretable wall motion in intensive care unit patients," *J Am Coll Cardiol*, vol. 35, pp. 485–90, Feb 2000.

[69] L. J. Crouse, J. Cheirif, D. E. Hanly, J. A. Kisslo, A. J. Labovitz, J. S. Raichlen, R. W. Schutz, P. M. Shah, and M. D. Smith, "Opacification and border delineation improvement in patients with suboptimal endocardial border definition in routine echocardiography: results of the phase III Albunex Multicenter Trial," *J Am Coll Cardiol*, vol. 22, pp. 1494–500, Nov 1993.

[70] K. Wei, "Detection and quantification of coronary stenosis severity with myocardial contrast echocardiography," *Prog Cardiovasc Dis*, vol. 44, pp. 81–100, Jan 2001.

[71] K. Wei, A. R. Jayaweera, S. Firoozan, A. Linka, D. M. Skyba, and S. Kaul, "Quantification of myocardial blood flow with ultrasound-induced destruction of microbubbles administered as a constant venous infusion," *Circulation*, vol. 97, pp. 473–83, Feb 1998.

[72] S. R. Sirsi, M. L. Flexman, F. Vlachos, J. Huang, S. L. Hernandez, H. K. Kim, T. B. Johung, J. W. Gander, A. R. Reichstein, B. S. Lampl, A. Wang, A. H. Hielscher, J. J. Kandel, D. J. Yamashiro, and M. A. Borden, "Contrast ultrasound imaging for identification of early responder tumor models to anti-angiogenic therapy," *Ultrasound Med Biol*, vol. 38, pp. 1019–29, Jun 2012.

[73] K. Hoyt, A. Sorace, and R. Saini, "Quantitative mapping of tumor vascularity using volumetric contrast-enhanced ultrasound," *Invest Radiol*, vol. 47, pp. 167–74, Mar 2012.

[74] R. E. Pollard and R. F. Larson, "Dynamic contrast-enhanced computed tomography for the quantification of tumor response to vasoactive agents in a rat tumor model: preliminary results," *Contrast Media Mol Imaging*, vol. 6, pp. 28–34, Jan 2011.

[75] C. C. Chen and M. A. Borden, "Ligand conjugation to bimodal poly(ethylene glycol) brush layers on microbubbles," *Langmuir*, vol. 26, pp. 13183–94, Aug 2010.

[76] G. M. Lanza and S. Wickline, "Targeted ultrasonic contrast agents for molecular imaging and therapy," *Curr Prob Cardiology*, vol. 28, pp. 625–653, Jan 2003.

[77] F. S. Villanueva, E. Lu, S. Bowry, S. Kilic, E. M. Tom, J. Wang, J. Gretton, J. J. Pacella, and W. R. Wagner, "Myocardial ischemic memory imaging with molecular echocardiography," *Circulation*, vol. 115, pp. 345–52, Jan 2007.

[78] G. E. R. Weller, E. Lu, M. M. Csikari, A. L. Klibanov, D. Fischer, W. R. Wagner, and F. S. Villanueva, "Ultrasound imaging of acute cardiac transplant rejection with microbubbles targeted to intercellular adhesion molecule-1," *Circulation*, vol. 108, pp. 218–24, Jul 2003.

[79] P. A. Grayburn, "Product safety compromises patient safety (an unjustified black box warning on ultrasound contrast agents by the food and drug administration)," *Am J Cardiol*, vol. 101, pp. 892–3, Mar 2008.

[80] M. L. Main, J. H. Goldman, and P. A. Grayburn, "Ultrasound contrast agents: balancing safety versus efficacy," *Expert Opin Drug Saf*, vol. 8, pp. 49–56, Jan 2009.

[81] J. E. Streeter, R. C. Gessner, J. Tsuruta, S. Feingold, and P. A. Dayton, "Assessment of molecular imaging of angiogenesis with three-dimensional ultrasonography," *Mol Imaging*, vol. 10, pp. 460–468, Apr 2011.

[82] P. Frinking, A. Bouakaz, J. Kirkhorn, F. J. T. Cate, and N. de Jong, "Ultrasound contrast imaging: current and new potential methods," *Ultrasound Med Biol*, vol. 26, pp. 965–75, Jul 2000.

[83] A. L. Klibanov, P. T. Rasche, M. S. Hughes, J. K. Wojdyla, K. P. Galen, J. H. Wible, and G. H. Brandenburger, "Detection of individual microbubbles of ultrasound contrast agents: imaging of free-floating and targeted bubbles," *Invest Radiol*, vol. 39, pp. 187–95, Mar 2004.

[84] G. Brock-Fisher, M. Poland, and P. G. Rafter, "Means for increasing sensitivity in non-linear ultrasound imaging systems," *US Patent 5577505*, pp. 1–5, Feb 1996.

[85] C. Chapman and J. Lazenby, "Ultrasound imaging system employing phase inversion subtraction to enhance the image," *US Patent 5632277*, pp. 1–5, Feb 1997.

[86] P. Phillips and E. Gardner, "Contrast-agent detection and quantification," *Eur Radiol*, vol. 14 Suppl 8, pp. P4–10, Oct 2004.

[87] J. Chomas, P. Dayton, D. May, and K. Ferrara, "Nondestructive subharmonic imaging," *IEEE Trans Ultrason Ferroelectr Freq Control*, vol. 49, pp. 883–92, Jul 2002.

[88] P. M. Shankar, P. D. Krishna, and V. L. Newhouse, "Subharmonic backscattering from ultrasound contrast agents," *J Acoust Soc Am*, vol. 106, pp. 2104–10, Oct 1999.

[89] F. Forsberg, W. T. Shi, and B. B. Goldberg, "Subharmonic imaging of contrast agents," *Ultrasonics*, vol. 38, pp. 93–8, Mar 2000.

[90] K. Johnson, R. Cianciolo, R. C. Gessner, and P. A. Dayton, "A pilot study to assess markers of renal damage in the rodent kidney after exposure to 7 MHz ultrasound pulse sequences designed to cause microbubble translation and disruption," *Ultrasound Med Biol*, vol. 38, pp. 168–72, Jan 2012.

[91] B. A. Kaufmann, C. L. Carr, T. Belcik, A. Xie, B. Kron, Q. Yue, and J. R. Lindner, "Effect of acoustic power on in vivo molecular imaging with targeted microbubbles: implications for low-mechanical index real-time imaging," *J Am Soc Echocardiogr*, vol. 23, pp. 79–85, Jan 2010.

[92] S. Feingold, R. C. Gessner, I. M. Guracar, and P. A. Dayton, "Quantitative volumetric perfusion mapping of the microvasculature using contrast ultrasound," *Invest Radiol*, vol. 45, pp. 669–74, Oct 2010.

[93] T. Schroeder, H. Yuan, B. L. Viglianti, C. Peltz, S. Asopa, Z. Vujaskovic, and M. W. Dewhirst, "Spatial heterogeneity and oxygen dependence of glucose consumption in R3230Ac and fibrosarcomas of the Fischer 344 rat," *Cancer Res*, vol. 65, pp. 5163–71, Jun 2005.

[94] E. Quaia, "Assessment of tissue perfusion by contrast-enhanced ultrasound," *Eur Radiol*, vol. 21, pp. 604–15, Mar 2011.

[95] D. Cosgrove, R. Eckersley, M. Blomley, and C. Harvey, "Quantification of blood flow," *Eur Radiol*, vol. 11, pp. 1338–44, Jan 2001.

[96] R. E. Pollard, A. R. Sadlowski, S. H. Bloch, L. Murray, E. R. Wisner, S. Griffey, and K. W. Ferrara, "Contrast-assisted destruction-replenishment ultrasound for the assessment of tumor microvasculature in a rat model," *Technol Cancer Res Treat*, vol. 1, pp. 459–70, Dec 2002.

[97] R. E. Pollard, P. A. Dayton, K. D. Watson, X. Hu, I. M. Guracar, and K. W. Ferrara, "Motion corrected cadence CPS ultrasound for quantifying response to vasoactive drugs in a rat kidney model," *Urology*, vol. 74, pp. 675–81, Sep 2009.

[98] J. R. Lindner, P. A. Dayton, M. P. Coggins, K. F. Ley, J. Song, K. W. Ferrara, and S. Kaul, "Noninvasive imaging of inflammation by ultrasound detection of phagocytosed microbubbles," *Circulation*, vol. 102, pp. 531–8, Aug 2000.

[99] P. A. Dayton and K. W. Ferrara, "Targeted imaging using ultrasound," *J Magn Reson Imaging*, vol. 16, pp. 362–77, Oct 2002.

[100] J. R. Lindner, M. P. Coggins, S. Kaul, A. L. Klibanov, G. H. Brandenburger, and K. F. Ley, "Microbubble persistence in the microcirculation during ischemia/reperfusion and inflammation is caused by integrin- and complement-mediated adherence to activated leukocytes," *Circulation*, vol. 101, pp. 668–75, Feb 2000.

[101] F. S. Villanueva, R. J. Jankowski, S. Klibanov, M. L. Pina, S. M. Alber, S. C. Watkins, G. H. Brandenburger, and W. R. Wagner, "Microbubbles targeted to intercellular adhesion molecule-1 bind to activated coronary artery endothelial cells," *Circulation*, vol. 98, pp. 1–5, Jul 1998.

[102] R. C. Gessner, J. E. Streeter, R. Kothadia, S. Feingold, and P. A. Dayton, "An in vivo validation of the application of acoustic radiation force to enhance the diagnostic utility of molecular imaging using 3-D ultrasound," *Ultrasound Med Biol*, Feb 2012.

[103] P. J. A. Frinking, I. Tardy, M. Théraulaz, M. Arditi, J. Powers, S. Pochon, and F. Tranquart, "Effects of acoustic radiation force on the binding efficiency of BR55, a VEGFR2-specific ultrasound contrast agent," *Ultrasound Med Biol*, May 2012.

[104] J. K. Willmann, A. M. Lutz, R. Paulmurugan, M. R. Patel, P. Chu, J. Rosenberg, and S. S. Gambhir, "Dual-targeted contrast agent for US assessment of tumor angiogenesis in vivo," *Radiology*, vol. 248, pp. 936–44, Sep 2008.

[105] M. Kaya, S. Feingold, J. E. Streeter, K. Hettiarachchi, A. P. Lee, and P. A. Dayton, "Acoustic characterization of individual monodisperse contrast agents with an optical-acoustical system," *IEEE Ultrasonics Symposium*, pp. 1–4, Sep 2009.

[106] E. Talu, K. Hettiarachchi, S. Zhao, R. L. Powell, A. P. Lee, M. L. Longo, and P. A. Dayton, "Tailoring the size distribution of ultrasound contrast agents: possible method for improving sensitivity in molecular imaging," *Mol Imaging*, vol. 6, pp. 384–92, Jan 2007.

[107] A. L. Klibanov, J. J. Rychak, W. C. Yang, S. Alikhani, B. Li, S. Acton, J. R. Lindner, K. F. Ley, and S. Kaul, "Targeted ultrasound contrast agent for molecular imaging of inflammation in high-shear flow," *Contrast Media Mol Imaging*, vol. 1, pp. 259–66, Jan 2006.

[108] J. R. Lindner, J. Song, F. Xu, A. L. Klibanov, K. Singbartl, K. F. Ley, and S. Kaul, "Noninvasive ultrasound imaging of inflammation using microbubbles targeted to activated leukocytes," *Circulation*, vol. 102, pp. 2745–50, Nov 2000.

[109] D. B. Ellegala, H. Leong-Poi, J. E. Carpenter, A. L. Klibanov, S. Kaul, M. E. Shaffrey, J. Sklenar, and J. R. Lindner, "Imaging tumor angiogenesis with contrast ultrasound and microbubbles targeted to alpha(v)beta3," *Circulation*, vol. 108, pp. 336–41, Jul 2003.

[110] S. Zhao, M. A. Borden, S. H. Bloch, D. E. Kruse, K. W. Ferrara, and P. A. Dayton, "Radiation-force assisted targeting facilitates ultrasonic molecular imaging," *Mol Imaging*, vol. 3, pp. 135–48, Jul 2004.

[111] S. Zhao, D. E. Kruse, K. W. Ferrara, and P. A. Dayton, "Acoustic response from adherent targeted contrast agents," *J Acoust Soc Am*, vol. 120, pp. EL63–9, Dec 2006.

[112] S. Zhao, D. E. Kruse, K. W. Ferrara, and P. A. Dayton, "Selective imaging of adherent targeted ultrasound contrast agents," *Phys Med Biol*, vol. 52, pp. 2055–72, Apr 2007.

[113] J. J. Rychak, J. R. Lindner, K. F. Ley, and A. L. Klibanov, "Deformable gas-filled microbubbles targeted to p-selectin," *J Control Release*, vol. 114, pp. 288–99, Sep 2006.

[114] G. E. R. Weller, M. K. K. Wong, R. A. Modzelewski, E. Lu, A. L. Klibanov, W. R. Wagner, and F. S. Villanueva, "Ultrasonic imaging of tumor angiogenesis using contrast microbubbles targeted via the tumor-binding peptide arginine-arginine-leucine," *Cancer Res*, vol. 65, pp. 533–9, Jan 2005.

[115] K. P. Pancholi, U. Farook, R. Moaleji, E. Stride, and M. J. Edirisinghe, "Novel methods for preparing phospholipid coated microbubbles," *Eur Biophys J*, vol. 37, pp. 515–20, Apr 2008.

[116] U. Farook, E. Stride, and M. Edirisinghe, "Controlling size and size distribution of electrohydrodynamically prepared microbubbles," *Bubble Sci Eng Technol*, vol. 1, no. 1-2, pp. 53–57, 2009.

[117] E. Stride and M. Edirisinghe, "Novel preparation techniques for controlling microbubble uniformity: a comparison," *Med Biol Eng Comput*, vol. 47, pp. 883–92, Aug 2009.

[118] M. A. Borden and M. L. Longo, "Dissolution behavior of lipid monolayer-coated, air-filled microbubbles: Effect of lipid hydrophobic chain length," *Langmuir*, vol. 18, pp. 9225–9233, 2002.

[119] A. Kabalnov, J. Bradley, S. Flaim, D. Klein, T. Pelura, B. Peters, S. Otto, J. Reynolds, E. Schutt, and J. Weers, "Dissolution of multicomponent microbubbles in the bloodstream: 2. experiment," *Ultrasound Med Biol*, vol. 24, pp. 751–60, Jun 1998.

[120] C. Sonne, F. Xie, J. Lof, J. Oberdorfer, P. Phillips, E. C. Everbach, and T. R. Porter, "Differences in Definity and Optison microbubble destruction rates at a similar mechanical index with different real-time perfusion systems," *J Am Soc Echocardiogr*, vol. 16, pp. 1178–85, Nov 2003.

[121] S. W. Smith, R. F. Wagner, J. Sandrik, and H. Lopez, "Low contrast detectability and contrast/detail analysis in medical ultrasound," *IEEE Trans Ultrason Ferroelectr Freq Control*, vol. 30, pp. 164–173, May 1983.

[122] A. Needles, O. Couture, and F. S. Foster, "A method for differentiating targeted microbubbles in real time using subharmonic micro-ultrasound and interframe filtering," *Ultrasound Med Biol*, vol. 35, pp. 1564–73, Sep 2009.

[123] R. N. Rankin, A. Fenster, D. B. Downey, P. L. Munk, M. F. Levin, and A. D. Vellet, "Three-dimensional sonographic reconstruction: techniques and diagnostic applications," *AJR Am J Roentgenol*, vol. 161, pp. 695–702, Oct 1993.

[124] V. Mor-Avi, L. Sugeng, and R. M. Lang, "Three-dimensional adult echocardiography: where the hidden dimension helps," *Curr Cardiol Rep*, vol. 10, pp. 218–25, May 2008.

[125] L. Coyne, K. Jayaprakasan, and N. Raine-Fenning, "3D ultrasound in gynecology and reproductive medicine," *Women's health (London, England)*, vol. 4, pp. 501–16, Sep 2008.

[126] E. Leen, S. Kumar, S. A. Khan, G. Low, K. O. Ong, P. Tait, and M. Averkiou, "Contrast-enhanced 3D ultrasound in the radiofrequency ablation of liver tumors," *World J Gastroentero*, vol. 15, pp. 289–299, Jan 2009.

[127] W. Luo, K. Numata, M. Morimoto, A. Nozaki, Y. Nagano, K. Sugimori, and K. Tanaka, "Three-dimensional contrast-enhanced sonography of vascular patterns of focal liver tumors: pilot study of visualization methods," *AJR Am J Roentgenol*, vol. 192, pp. 165–73, Jan 2009.

[128] M. Reinhardt, P. Hauff, R. A. Linker, A. Briel, R. Gold, P. Rieckmann, G. Becker, K. V. Toyka, M. Mäurer, and M. Schirner, "Ultrasound derived imaging and quantification of cell adhesion molecules in experimental autoimmune encephalomyelitis (EAE) by sensitive particle acoustic quantification (SPAQ)," *Neuroimage*, vol. 27, pp. 267–78, Aug 2005.

[129] R. Weinberg, *The Biology of Cancer*. Garland Science, Taylor and Francis Group, LLC, Jan 2007.

[130] B. J. Pichler, M. Kneilling, R. Haubner, H. Braumüller, M. Schwaiger, M. Röcken, and W. A. Weber, "Imaging of delayed-type hypersensitivity reaction by PET and 18F-galacto-RGD," *J Nucl Med*, vol. 46, pp. 184–9, Jan 2005.

[131] P. A. Dayton, J. S. Allen, and K. W. Ferrara, "The magnitude of radiation force on ultrasound contrast agents," *J Acoust Soc Am*, vol. 112, pp. 2183–92, Nov 2002.

[132] M. Shortencarier and P. A. Dayton, "A method for radiation-force localized drug delivery using gas-filled lipospheres," *IEEE Trans Ultrason Ferroelectr Freq Control*, vol. 51, no. 7, pp. 822 – 831, 2004.

[133] A. F. H. Lum, M. A. Borden, P. A. Dayton, D. E. Kruse, S. I. Simon, and K. W. Ferrara, "Ultrasound radiation force enables targeted deposition of model drug carriers loaded on microbubbles," *J Control Release*, vol. 111, pp. 128–34, Mar 2006.

[134] A. Kheirolomoom, P. A. Dayton, A. F. H. Lum, E. Little, E. E. Paoli, H. Zheng, and K. W. Ferrara, "Acoustically-active microbubbles conjugated to liposomes: characterization of a proposed drug delivery vehicle," *J Control Release*, vol. 118, pp. 275–84, Apr 2007.

[135] J. R. Lindner, J. Song, J. Christiansen, A. L. Klibanov, F. Xu, and K. F. Ley, "Ultrasound assessment of inflammation and renal tissue injury with microbubbles targeted to p-selectin," *Circulation*, vol. 104, pp. 2107–12, Oct 2001.

[136] A. V. Patil, J. J. Rychak, J. S. Allen, A. L. Klibanov, and J. A. Hossack, "Dual frequency method for simultaneous translation and real-time imaging of ultrasound contrast agents within large blood vessels," *Ultrasound Med Biol*, vol. 35, pp. 2021–30, Dec 2009.

[137] D. Christensen, *Ultrasonic Bioinstrumentation*. John Wiley and Sons, Ltd., Jan 1988.

[138] F. T. D'Astous and F. S. Foster, "Frequency dependence of ultrasound attenuation and backscatter in breast tissue," *Ultrasound Med Biol*, vol. 12, pp. 795–808, Oct 1986.

[139] C. H. Chang, S. W. Huang, H. C. Yang, Y. H. Chou, and P. C. Li, "Reconstruction of ultrasonic sound velocity and attenuation coefficient using linear arrays: clinical assessment," *Ultrasound Med Biol*, vol. 33, pp. 1681–7, Nov 2007.

[140] M. Palmowski, J. Huppert, P. Hauff, M. Reinhardt, K. Schreiner, M. A. Socher, P. Hallscheidt, G. W. Kauffmann, W. Semmler, and F. Kiessling, "Vessel fractions in tumor xenografts depicted by flow- or contrast-sensitive three-dimensional high-frequency doppler ultrasound respond differently to antiangiogenic treatment," *Cancer Res*, vol. 68, pp. 7042–9, Sep 2008.

[141] S. Kotopoulis and M. Postema, "Microfoam formation in a capillary," *Ultrasonics*, vol. 50, pp. 260–8, Feb 2010.

[142] J. Szebeni, "Complement activation-related pseudoallergy: a new class of drug-induced acute immune toxicity," *Toxicology*, vol. 216, pp. 106–21, Dec 2005.

[143] C. C. Chen, S. R. Sirsi, S. Homma, and M. A. Borden, "Effect of surface architecture on in vivo ultrasound contrast persistence of targeted size-selected microbubbles," *Ultrasound Med Biol*, vol. 38, pp. 492–503, Mar 2012.

[144] V. C. Mosqueira, P. Legrand, A. Gulik, O. Bourdon, R. Gref, D. Labarre, and G. Barratt, "Relationship between complement activation, cellular uptake and surface physicochemical aspects of novel PEG-modified nanocapsules," *Biomaterials*, vol. 22, pp. 2967–79, Nov 2001.

[145] J. Fu, M. Bian, Q. Jiang, and C. Zhang, "Roles of aurora kinases in mitosis and tumorigenesis," *Mol Cancer Res*, vol. 5, pp. 1–10, Jan 2007.

[146] D. M. Glover, M. H. Leibowitz, D. A. McLean, and H. Parry, "Mutations in aurora prevent centrosome separation leading to the formation of monopolar spindles," *Cell*, vol. 81, pp. 95–105, Apr 1995.

[147] T. Hirota, N. Kunitoku, T. Sasayama, T. Marumoto, D. Zhang, M. Nitta, K. Hatakeyama, and H. Saya, "Aurora-A and an interacting activator, the LIM protein Ajuba, are required for mitotic commitment in human cells," *Cell*, vol. 114, pp. 585–98, Sep 2003.

[148] D. Li, J. Zhu, P. F. Firozi, J. L. Abbruzzese, D. B. Evans, K. Cleary, H. Friess, and S. Sen, "Overexpression of oncogenic STK15/BTAK/aurora A kinase in human pancreatic cancer," *Clin Cancer Res*, vol. 9, pp. 991–7, Mar 2003.

[149] M. Tatsuka, H. Katayama, T. Ota, T. Tanaka, S. Odashima, F. Suzuki, and Y. Terada, "Multinuclearity and increased ploidy caused by overexpression of the aurora- and Ipl1-like midbody-associated protein mitotic kinase in human cancer cells," *Cancer Res*, vol. 58, pp. 4811–6, Nov 1998.

[150] H. Zhou, J. Kuang, L. Zhong, W. L. Kuo, J. W. Gray, A. Sahin, B. R. Brinkley, and S. Sen, "Tumour amplified kinase STK15/BTAK induces centrosome amplification, aneuploidy and transformation," *Nat Genet*, vol. 20, pp. 189–93, Oct 1998.

[151] H. Katayama, T. Ota, F. Jisaki, Y. Ueda, T. Tanaka, S. Odashima, F. Suzuki, Y. Terada, and M. Tatsuka, "Mitotic kinase expression and colorectal cancer progression," *J Natl Cancer Inst*, vol. 91, pp. 1160–2, Jul 1999.

[152] O. Gautschi, J. Heighway, P. C. Mack, P. R. Purnell, P. N. Lara, and D. R. Gandara, "Aurora kinases as anticancer drug targets," *Clin Cancer Res*, vol. 14, pp. 1639–48, Mar 2008.

[153] H. Kovar, "Aurka inhibitors: right in time," *Pediatr Blood Cancer*, vol. 55, pp. 3–4, Jul 2010.

[154] A. D. V. den Abbeele, C. Gatsonis, D. J. de Vries, Y. Melenevsky, A. Szot-Barnes, J. T. Yap, A. K. Godwin, L. Rink, M. Huang, M. Blevins, J. Sicks, B. Eisenberg, and B. A. Siegel, "ACRIN 6665/RTOG 0132 phase II trial of neoadjuvant imatinib mesylate for operable malignant gastrointestinal stromal

tumor: monitoring with 18F-FDG PET and correlation with genotype and GLUT4 expression," *J Nucl Med*, vol. 53, pp. 567–74, Apr 2012.

[155] J. O. Prior, M. Montemurro, M. V. Orcurto, O. Michielin, F. Luthi, J. Benhattar, L. Guillou, V. Elsig, R. Stupp, A. B. Delaloye, and S. Leyvraz, "Early prediction of response to sunitinib after imatinib failure by 18F-fluorodeoxyglucose positron emission tomography in patients with gastrointestinal stromal tumor," *J Clin Oncol*, vol. 27, pp. 439–45, Jan 2009.

[156] D. Kim and J. Chung, "Akt: versatile mediator of cell survival and beyond," *J Biochem Mol Biol*, vol. 35, pp. 106–15, Jan 2002.

[157] Y. H. Lin, C. C. Lee, W. L. Chan, W. H. Chang, Y. C. Wu, and J. G. Chang, "16-Hydroxycleroda-3,13-dien-15,16-olide deregulates PI3K and aurora B activities that involve in cancer cell apoptosis," *Toxicology*, vol. 285, pp. 72–80, Jul 2011.

[158] J. K. Willmann, R. H. Kimura, N. Deshpande, A. M. Lutz, J. R. Cochran, and S. S. Gambhir, "Targeted contrast-enhanced ultrasound imaging of tumor angiogenesis with contrast microbubbles conjugated to integrin-binding knottin peptides," *J Nucl Med*, vol. 51, pp. 433–40, Mar 2010.

[159] S. Pochon, I. Tardy, P. Bussat, T. Bettinger, J. Brochot, M. von Wronski, L. Passantino, and M. Schneider, "BR55: a lipopeptide-based VEGFR2-targeted ultrasound contrast agent for molecular imaging of angiogenesis," *Invest Radiol*, vol. 45, pp. 89–95, Feb 2010.

[160] S. M. Stieger, S. H. Bloch, O. Foreman, E. R. Wisner, K. W. Ferrara, and P. A. Dayton, "Ultrasound assessment of angiogenesis in a matrigel model in rats," *Ultrasound Med Biol*, vol. 32, pp. 673–81, May 2006.

[161] J. Du, F. H. Li, H. Fang, J. G. Xia, and C. X. Zhu, "Correlation of real-time gray scale contrast-enhanced ultrasonography with microvessel density and vascular endothelial growth factor expression for assessment of angiogenesis in breast lesions," *J Ultrasound Med*, vol. 27, pp. 821–31, Jun 2008.

[162] R. L. Foote, N. Weidner, J. Harris, E. Hammond, J. E. Lewis, T. Vuong, K. K. Ang, and K. K. Fu, "Evaluation of tumor angiogenesis measured with microvessel density (MVD) as a prognostic indicator in nasopharyngeal carcinoma: results of RTOG 9505," *Int J Radiat Oncol Biol Phys*, vol. 61, pp. 745–53, Mar 2005.

[163] O. N. El-Assal, A. Yamanoi, Y. Soda, M. Yamaguchi, M. Igarashi, A. Yamamoto, T. Nabika, and N. Nagasue, "Clinical significance of microvessel density and vascular endothelial growth factor expression in hepatocellular carcinoma and surrounding liver: possible involvement of vascular endothelial growth factor in the angiogenesis of cirrhotic liver," *Hepatology*, vol. 27, pp. 1554–62, Jun 1998.

[164] B. Rubio-Viqueira, A. Jimeno, G. Cusatis, X. Zhang, C. Iacobuzio-Donahue, C. Karikari, C. Shi, K. Danenberg, P. V. Danenberg, H. Kuramochi, K. Tanaka, S. Singh, H. Salimi-Moosavi, N. Bouraoud, M. L. Amador, S. Altiok, P. Kulesza, C. Yeo, W. Messersmith, J. Eshleman, R. H. Hruban, A. Maitra, and M. Hidalgo, "An in vivo platform for translational drug development in pancreatic cancer," *Clin Cancer Res*, vol. 12, pp. 4652–61, Aug 2006.

[165] D. Decaudin, "Primary human tumor xenografted models ('tumorgrafts') for good management of patients with cancer," *Anticancer Drugs*, May 2011.

[166] A. Guibal, L. Taillade, S. Mulé, E. Comperat, Y. Badachi, J. L. Golmard, D. L. Guillou-Buffello, O. Rixe, S. L. Bridal, and O. Lucidarme, "Noninvasive contrast-enhanced US quantitative assessment of tumor microcirculation in a murine model: effect of discontinuing anti-VEGF therapy," *Radiology*, vol. 254, pp. 420–9, Feb 2010.

[167] J. H. Zhou, L. H. Cao, J. B. Liu, W. Zheng, M. Liu, R. Z. Luo, F. Han, and A. H. Li, "Quantitative assessment of tumor blood flow in mice after treatment with different doses of an antiangiogenic agent with contrast-enhanced destruction-replenishment US," *Radiology*, vol. 259, pp. 406–13, May 2011.

[168] G. D. Ayers, E. T. McKinley, P. Zhao, J. M. Fritz, R. E. Metry, B. C. Deal, K. M. Adlerz, R. J. Coffey, and H. C. Manning, "Volume of preclinical xenograft tumors is more accurately assessed by ultrasound imaging than manual caliper measurements," *J Ultrasound Med*, vol. 29, pp. 891–901, Jun 2010.

[169] D. M. Euhus, C. Hudd, M. C. LaRegina, and F. E. Johnson, "Tumor measurement in the nude mouse," *J Surg Oncol*, vol. 31, pp. 229–34, Apr 1986.

[170] P. McQuade and L. C. KnIght, "Radiopharmaceuticals for targeting the angiogenesis marker alpha(v)beta(3)," *Q J Nucl Med*, vol. 47, pp. 209–20, Sep 2003.

[171] T. V. Byzova, R. Rabbani, S. E. D'Souza, and E. F. Plow, "Role of integrin alpha(v)beta3 in vascular biology," *Thromb Haemost*, vol. 80, pp. 726–34, Nov 1998.